

Photovoltaic-(photo)electrochemical devices for water splitting and water treatment

Perez Rodriguez, Paula

10.4233/uuid:339df29d-8658-4ff7-a124-84f1cd6043ad

Publication date

Document Version Final published version

Citation (APA)

Perez Rodriguez, P. (2018). Photovoltaic-(photo)electrochemical devices for water splitting and water treatment. [Dissertation (TÚ Delft), Delft University of Technology]. https://doi.org/10.4233/uuid:339df29d-8658-4ff7-a124-84f1cd6043ad

Important note

To cite this publication, please use the final published version (if applicable). Please check the document version above.

Copyright

Other than for strictly personal use, it is not permitted to download, forward or distribute the text or part of it, without the consent of the author(s) and/or copyright holder(s), unless the work is under an open content license such as Creative Commons.

Please contact us and provide details if you believe this document breaches copyrights. We will remove access to the work immediately and investigate your claim.

Photovoltaic-(photo)electrochemical devices for water splitting and water treatment

Proefschrift

ter verkrijging van de graad van doctor aan de Technische Universiteit Delft, op gezag van de Rector magnificus prof. dr. ir. T.H.J.J. van der Hagen, voorzitter van het College van Promoties, in het openbaar te verdedigen op vrijdag 7 September 2018 om 10:00 uur

> door Paula PEREZ RODRIGUEZ Master of Science in Sustainable Energy Technology Technische Universiteit Delft, Nederland geboren te Madrid, Spain

This dissertation has been approved by the promotors:

Prof. dr. M. Zeman

Prof. dr. A.H.M. Smets

Composition of the doctoral committee:

Rector Magnificus chairperson

Prof. dr. M. Zeman Technische Universiteit Delft, promotor

Prof. dr. A.H.M. Smets Technische Universiteit Delft, co-promotor

Independent members:

Prof. dr. ir. L.C. Rietveld Technische Universiteit Delft

Prof. dr. M.A.M.M. van der Meijden Technische Universiteit Delft

Prof. dr. Rutger Schlatmann Helmholtz Zentrum Berlin, Germany

Dr. ir. W.A. Smith

Technische Universiteit Delft

Dr. A. Bieberle DIFFER Institute, Netherlands

The work described in this is a part of the project "APPEL", founded by the Foundation for Fundamental Research on Matter (FOM), which is part of the Netherlands Organization for Scientific Research (NWO).

ISBN: 978-94-6366-061-7

Printed by *Ipskamp Printing*, the Netherlands.

To AMOR, ZORRO, and most of all, to AMIGO $\,$

Do not believe that science rise to greater heights, when it treats engineering with silent scorn.

Do not believe that science sinks to slavish depths, when it answers questions of engineering born.

Hendrik Casimir

Contents

1	Intr	oducti	ion	1
	1.1	Solar energy		
1.2 Photovoltaic (PV) technology			voltaic (PV) technology	3
		1.2.1	The PV effect	3
		1.2.2	Solar cell external parameters	5
		1.2.3	Areas for optimization for solar cell design	7
		1.2.4	Solar cell materials and architectures	8
			1.2.4.1 Silicon Heterojunction (SHJ) solar cells	9
			1.2.4.2 Thin-film silicon solar cells	10
		1.2.5	Multijunction solar cells	11
	1.3	Photo	electrochemical(PEC) technology	13
		1.3.1	PEC technology for water splitting	14
		1.3.2	PEC technology for water treatment	19
		1.3.3	Areas for optimization for PEC device design	22
	1.4	Resear	rch Questions and Outline of this Thesis	24
Ι.	- Sol	ar Wa	ater Splitting	27
2	Sola	ar wate	er splitting using a-SiC:H photocathodes	29
	2.1	Introd	uciton	30
	2.2	Mater	ials and methods	32
	2.3	Result	s and discussion	35
	2.4	Concl	usions	46

CONTENTS

3	Des	signing a silicon based multijunction for water splitting	49
	3.1	Introduction	50
	3.2	Materials and methods	51
		3.2.1 Synthesis methods	51
		3.2.2 Characterization methods	53
	3.3	Results and discussion	53
	3.4	Conclusions	61
4	Lig	ht management of a hybrid silicon cell for water splitting	63
	4.1	Introduction	64
	4.2	Materials and Methods	65
		4.2.1 Synthesis Method	65
		4.2.2 Characterization Method	66
	4.3	Results and Discussion	67
	4.4	Conclusions	73
II	- Sc	plar Water Treatment	7 5
5	Oxi	dation of organic pollutants by a BiVO ₄ photoanode and a solar cell	77
	5.1	Introduction	78
	5.2	Materials and methods	81
		5.2.1 Fabrication methods	81
		5.2.2 Characterization	83
	5.3	Results and discussion	87
		5.3.1 Photoelectrode Characterization	87
		5.3.2 Counter electrode characterization	100
		5.3.3 Solar cell and device characterization	102
	5.4	Conclusions	106
6	Pho	oto-oxidation of organic pollutants using a photovoltaic device	107
	6.1	Introduction	108
	6.2	Materials and methods	110
	6.3	Results and Discussion	112
	6.4	Conclusions	118

CONTENTS

7	Conclusions and Outlook				
	7.1	Concl	usions		121
		7.1.1	Solar water splitting		122
		7.1.2	Solar water treatment		124
	7.2	Outlo	ok		125
Sτ	ımma	ary			145
Sa	Samenvatting				
Li	st of	public	cations		153
Cı	Curriculum Vitae				

CONTENTS

1

Introduction

The world energy demand is expected to be one of the most important problems faced by humanity in the coming years. Both the total population and the energy consumption per capita are expected to rise in the following years. [1] At present, most of the energy demand is covered using fossil fuels. However, the combustion of fossil fuels produces greenhouse gas emissions, which leads to global warming and climate change. [2] Moreover, fossil fuels are a finite resource, resulting in volatile energy prices and political conflicts over their control. For these reasons, an alternative to cover the world energy demand without using fossil fuels must be developed.

Renewable energy sources seem to be the most probable candidates to replace fossil fuels. In particular, solar energy is the most abundant energy source in the world. [3] There are many ways to utilize solar energy to cover our energy demand by converting it to electrical, thermal or chemical energy. Solar cells are used to convert solar energy into electricity, and are among the most common technologies to use solar energy. However, due to the intermittency of the solar radiation availability, it is not feasible to adapt the solar electricity production to easily match the demand. An approach that can help matching demand and supply is the

use of large-scale energy storage. Although batteries are often used in PV system as energy storage, they are not suitable for large long-term energy storage due to their high costs and high self-discharge rates. Alternatively, solar water splitting is able to convert solar energy into chemical energy in the form of molecules, which can then be stored for long periods of time. This strategy can help to shift the supply of energy and electricity to the times when the demand cannot be covered otherwise.

In addition, the technology used to convert solar energy into chemical energy can also be used to drive pollutant degradation reactions to achieve very low pollutant concentrations. By using solar energy for water treatment, both the challenges of covering the energy demand and providing clean water to society can be addressed.

1.1 Solar energy

The Sun releases an enormous amount of electromagnetic radiation into the solar system in the form of photons, which can be defined as discrete packages of energy. The energy of these photons can be described as

$$E = \frac{hc}{\lambda} \tag{1.1}$$

where E is the energy of the photon, h is Planck's constant, c is the speed of light at vacuum and λ is the wavelength of the propagating light.

The Sun emits light at a range of different wavelengths, forming the solar spectrum shown in Figure 1.1. The general shape of the spectrum corresponds to the black body radiation at the temperature of the Sun's surface, at around 6000 K. The radiation reaching the outer layer of the Earth's atmosphere is called AM0. By integrating the incident light across the solar spectrum, the total normal power density can be calculated as 1353 W/m² for AM0. However, the solar radiation at the Earth's surface is generally more relevant for solar cell applications. To account for the effects of the Earth's atmosphere on the radiation spectrum, the Air Mass (AM) is defined. The AM measures the effect of absorption in the atmosphere on the solar radiation spectrum reaching the Earth's surface, and it is determined as [4]

$$AM = \frac{1}{\cos(\theta)} \tag{1.2}$$

where θ is the angle of incidence of the light on the Earth's surface. The standard AM used in solar energy applications is the AM1.5 spectrum, which corresponds to an angle of incidence of 48.2 ° and a total power density of 1000 W/m².

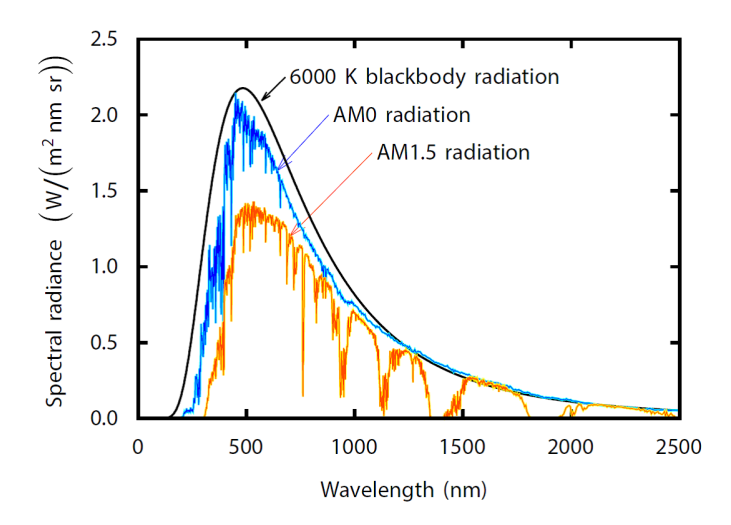


Figure 1.1: Radiation spectrum for a black body at 6000K, the AM0 exatterrestrial solar spectrum and the AM1.5 global solar spectrum. [5]

1.2 Photovoltaic (PV) technology

PV technology converts the solar radiation incident on the Earth's surface into electrical voltage and/or current. It is based on the photovoltaic (PV) effect. This section addresses the main principles behind the conversion of solar energy into electricity, as well as the main architectures normally used in PV devices.

1.2.1 The PV effect

The PV effect refers to the process in which photons excite electrical charges in a semiconductor absorber material These mobile charge carriers are able to generate a voltage and/or current inside a semiconductor device. To create this voltage, the generated charge carriers must be separated and collected using a junction of a material with different doping (homojunction) or a junction of two different materials (heterojunction). Figure 1.2 depicts

the general structure of a solar cell and the corresponding band diagram of a semiconductor junction to better visualize the PV effect.

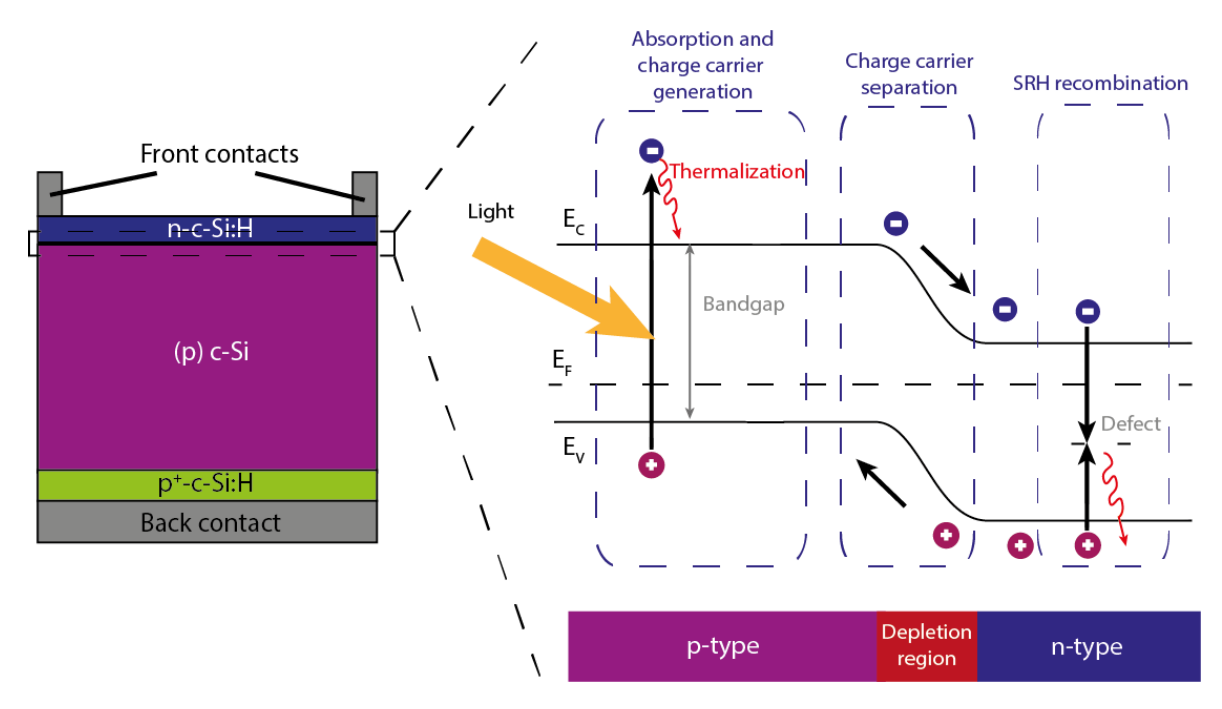


Figure 1.2: Schematic of a typical c-Si solar cell structure, and band diagram of the p-n junction, including the conduction band energy level (E_C) , the valence band energy level (E_V) , and the Fermi energy level (E_F) . The processes shown are the absorption of light and charge carrier generation, the charge carrier separation and the Shockley-Read-Hall (SRH) recombination

The absorption of light and charge carrier generation in the semiconductor absorber material depend on the bandgap of the semiconductor, which is defined as the energy difference between the conduction and valence band edges. Photons with energy higher than the bandgap excite electrons to a higher energy level in the so-called conduction band. The energy difference between the photon energy and the bandgap energy is emitted as heat when the electron and hole relax to the bottom and top of their allowed energy states, respectively. If the photon has an energy lower than the bandgap, the electron does not reach its higher allowed energy state, and no mobile charge carriers are generated. Therefore, the bandgap of the semiconductor determines which photons can be absorbed.

Once the mobile charge carriers are generated, they diffuse to the selective contacts, where they are separated by means of an electric field in the so-called depletion region. Such electric fields are produced by creating junctions of either different materials (heterojuncitons) or the same material with different doping atoms (homojuntions). For simplicity, this principle will be explained taking a homojunction as an example, as depicted in Figure 1.2. These junctions can be created by doping the semiconductor, meaning that some impurities are introduced in the intrinsic material. For example, in silicon this is done by either adding boron atoms or phosphorous atoms to the material. Boron atoms have only three valence electrons compared to the four valence electrons of silicon, and therefore they will be prompted to accept electrons, which generates holes (absence of an electron in the valence band). When holes are the majority charge carriers in the semiconductor, the material is p-type. On the other hand, phosphorous atoms have five valence electrons instead of the four valence electrons of silicon, which facilitates for one of them to detach from the atom, increasing the available free electron concentration. Therefore, electrons are the majority charge carriers in phosphorous doped materials (n-type material). Having a semiconductor junction would create an electric field in the depletion region, as illustrated in the band diagram in Figure 1.2 by the slope of the conduction and valence band edges. This electric field facilitates the separation and collection of charges carriers. However, energy states may exist in the middle of the bandgap due to defects inside the material. By using these defects as recombination centers, electrons and holes can recombine and emit heat in a process called Shockley-Read-Hall (SRH) recombination, as also shown in Figure 1.2.

1.2.2 Solar cell external parameters

Solar cells convert solar energy into electricity based on the PV effect. The main external parameters to characterize the performance of a solar cell under illumination are the maximum power point (MPP), the short-circuit current density, the open circuit voltage and the fill factor. Figure 1.3 presents an example of a current density-voltage (JV) characteristic of a solar cell, where the main solar cell external parameters have been indicated. These external parameters can also be defined as:

• Short-circuit current density, J_{SC} . The electrical current per unit of area that flows through the external circuit when the electrodes of the solar cell are short-circuited. It depends on the irradiance incident on the solar cell and the temperature of the device.

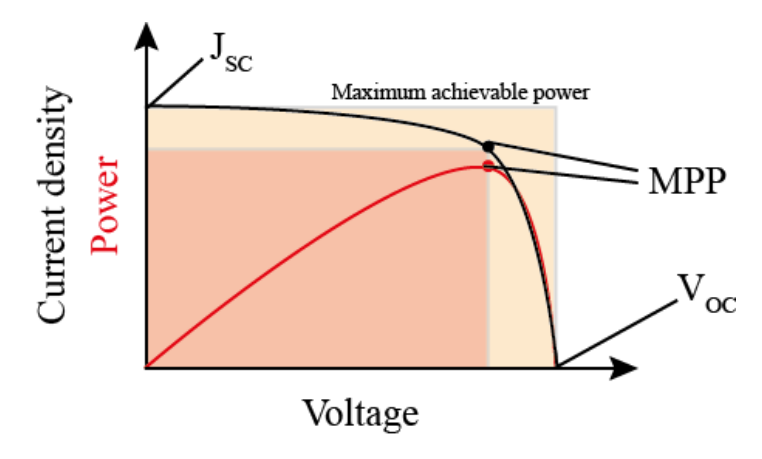


Figure 1.3: Example of a JV characteristic of a solar cell, including the J_{SC} , V_{OC} and MPP. The relation between the areas of MPP and the ideal case represents the FF.

• Open-circuit voltage, V_{OC} . The maximum voltage that a solar cell can deliver. It corresponds to the forward bias voltage at which the saturation current compensates the photo generated current. It can be defined as

$$V_{OC} = \frac{kT}{q} ln \left(\frac{J_{ph}}{J_0} + 1 \right) \tag{1.3}$$

where k is the Boltzmann constant, T is the temperature of the cell, q is the unity charge, J_{ph} is the photogenerated current density and J_0 is the charge saturation current density. Note that the open-circuit voltage also depends on the irradiance and temperature, as well as the material bandgap and device quality.

- Maximum power point (MPP). It is the operational voltage and current of the solar cell at which the power output is maximum for a given illumination.
- Fill factor, FF. It is the ratio between the maximum power generated by a solar cell and the product of V_{OC} and J_{SC}

$$FF = \frac{J_{mpp}V_{mpp}}{J_{SC}V_{OC}} \tag{1.4}$$

where J_{mpp} and V_{mpp} are the current density and voltage at maximum power point. The FF can be represented in Figure 1.3 as the ratio between maximum power that could be obtain from the solar cell and the power produced at MPP. The FF tends to be higher in PV cells with higher open-circuit voltages. [6] • Conversion efficiency, η . It is defined as the ratio between the maximum power generated by the solar cell and the incident solar power on the cell area, assuming the standard irradiance of the AM1.5 spectrum, 1000 W/m² and a temperature of 25°C.

$$\eta = \frac{J_{sc}V_{OC}FF}{P_{in}} \tag{1.5}$$

where P_{in} is the power going into the system, namely the irradiance incident in the solar cell.

1.2.3 Areas for optimization for solar cell design

In order to achieve an efficient PV device, certain areas for optimization must be considered when designing a solar cell, in which improvements are possible. These areas are depicted in Figure 1.4, as charge carrier collection, spectral utilization, light trapping and stability.

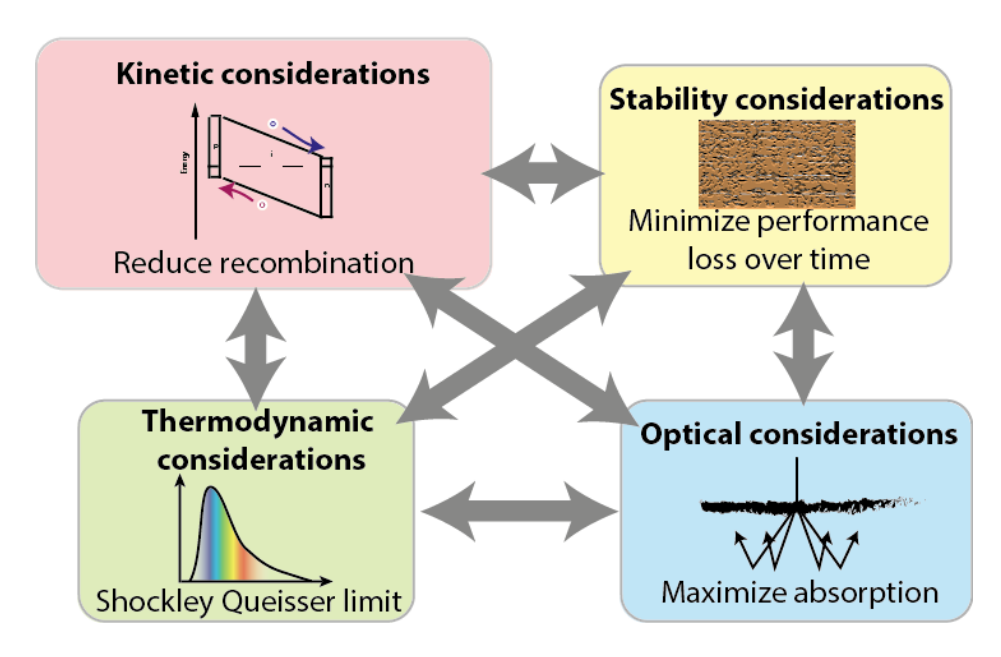


Figure 1.4: Schematic representation of the main areas for optimization involved in a PV solar cell

Kinetic considerations. The first area of interest refers to the challenges posed by recombination in a PV device, which is reflected in the difference between the bandgap energy and the energy difference between the quasi Fermi levels. To achieve high performance of PV devices, recombination of charge carriers both in the bulk of the absorber material and at the interfaces of the device must be avoided. In order to reduce recombination in the bulk

of the absorber material, its quality must be improved by avoiding defects such as impurities or dislocations within the crystal structure. To reduce recombination at the interfaces, good passivation and selective contacts can be applied. Finally, if the absorber material and interface quality are not good enough, electric fields can be introduced to effectively separate and collect the charge carriers. The quality of the charge carrier separation and collection is mainly reflected on the open-circuit voltage and fill factor.

Thermodynamic considerations. The second area to consider is the thermalization and non-absorption losses due to the mismatch between the photon energy and the bandgap energy of the semiconductor. It mainly depends on the bandgap energy of the semiconductor and the light spectrum. Better spectral utilization can be achieved by using multijunction solar cells, as will be further discussed in this section.

Optical considerations. The third area refers to the strategies used to maximize the light reaching the semiconductor and the light path inside a semiconductor, increasing the chance of the light being absorbed. The performance of the PV device is limited by optical losses such as reflection and transmission losses, parasitic absorption and shading losses. Some examples of light management strategies are texturing, back reflectors or anti-reflective coatings.

Stability considerations. The last area to consider is the stability of the device. For practical application of PV devices, they must maintain their performance over time under working conditions. Light and water exposure, heating or recombination within the device might be causes of device degradation, which would reduce its performance over time.

A delicate balance between the four areas of interest is established, in which changing one can drastically affect the others. Therefore, when designing a solar cell, all of these areas must be taken into account.

1.2.4 Solar cell materials and architectures

Some of the most common semiconductor absorber materials used for solar cells include crystalline silicon, copper indium gallium selenide (CIGS), cadmium telluride, III-V technologies and thin film silicon, organic materials or the most recently developed perovskite material.

[7, 8] In this project, only crystalline silicon and thin film silicon based solar cells were considered. These solar cell technologies have the advantages of material availability, low cost, competitive processing techniques, and flexibility of design.

1.2.4.1 Silicon Heterojunction (SHJ) solar cells

Among all single junction silicon PV devices, silicon heterojunction cells (SHJ) have the highest demonstrated efficiency. The world's highest recorded conversion efficiency for a SHJ solar cell is 26.7 %, recently achieved by Kaneka using an interdigitated back contact (IBC) solar cell structure. [9] A schematic of the traditional front/rear heterojunction solar cell, together with its band diagram, is shown in Figure 1.5. The thickness of the wafer typically ranges from 140 to 280 μ m. Thin layers of intrinsic a-Si:H are deposited on the wafer to achieve good surface passivation. Passivation needs to be done by intrinsic a-Si:H layers because doped a-Si:H has higher number of defects, and would reduce the surface passivation quality. To be able to collect the generated minority charge carriers, selective contacts are created by adding p and n supporting layers. Doped p-type a-Si:H and n-type a-Si:H layers are used for this purpose, as illustrated in Figure 1.5. The total thickness of the p/i and n/i a-Si:H layers are in the order of 5 to 20 nm.

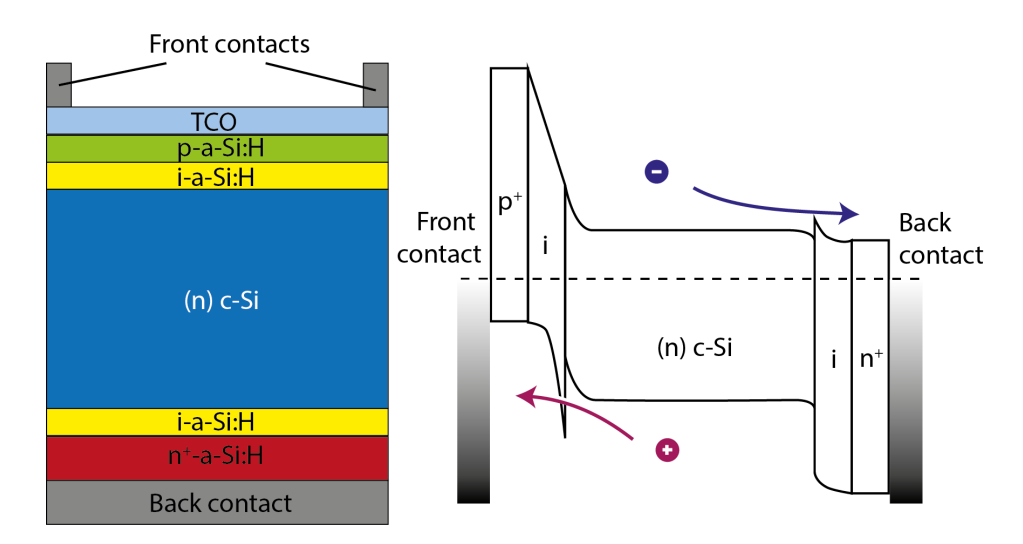


Figure 1.5: Schematic of a SHJ solar cell structure and its corresponding band diagram.

The SHJ structure has many benefits with respect to a traditional silicon homojunction shown in Figure 1.2. It enables good surface passivation of the c-Si wafer while also forming effective selective contacts, resulting in high efficiencies and open-circuit voltages. Moreover, the

a-Si:H layers are deposited at relatively low temperatures (<200 °C), preventing degradation of the quality of the c-Si bulk due to high temperature cycling. Finally, the symmetrical structure of the SHJ solar cell is advantageous to fabricate thinner cells. [10]

SHJ solar cells fabricated on n-doped c-Si wafers have so far been more efficient than on p-doped wafers. This is due to the asymmetry between the conduction and valence band offsets of the p and n supporting layers, which is assumed to reduce the performance of SHJ cells on a p-doped c-Si wafer. In addition, light soaking may detrimentally affect the bulk of p-type c-Si wafer, whereas no such effects are known for n-type wafers. [11]

1.2.4.2 Thin-film silicon solar cells

Most thin-film silicon based materials have a much lower charge carrier diffusion length than crystalline silicon. Therefore, PV devices based on these materials depend on the drift mechanism to efficiently separate charge carriers. Thin film silicon solar cells usually have a p-i-n, or n-i-p structure, (see Figure 1.6) in order to build an electric field across the i-layer and separate the charge carriers. The light is absorbed mainly in the thick intrinsic region. The thin doped layers create the internal electric field that extends across the entire i-layer, as indicated in the band diagram in Figure 1.6 by the slope in the conduction and valence band edges. Finally, the charge carriers are collected at the interface between the doped layers and the metal contacts.

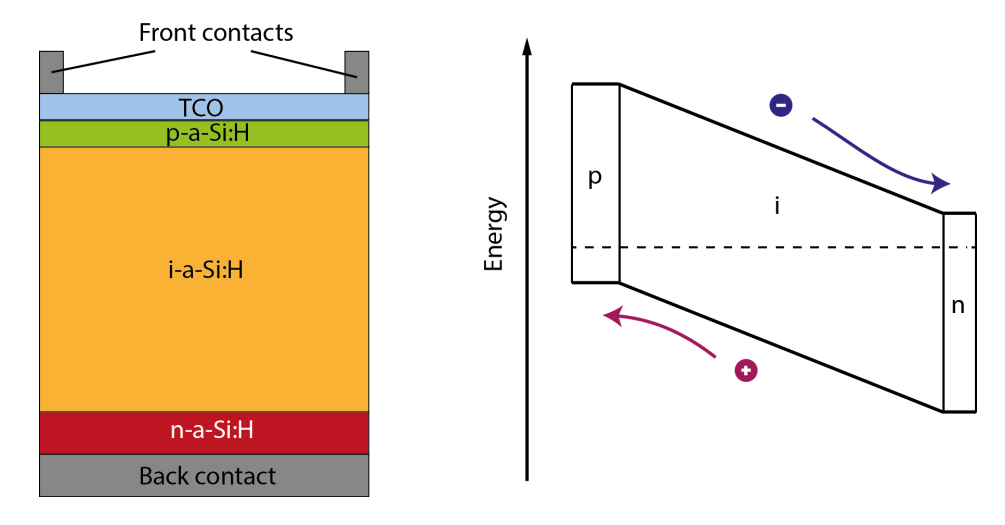


Figure 1.6: Example schematic of a p-i-n a-Si:H solar cell and its corresponding band diagram.

One of the most common active materials for thin film silicon based solar cells is hydrogenated amorphous silicon (a-Si:H). Unlike the crystalline silicon, a-Si:H has a direct bandgap and high absorption coefficient in the wavelength region above its bandgap, lowering the amount of material needed for light absorption. [5] The bandgap for a-Si:H is typically in the range of 1.7 to 1.8 eV, but it varies with deposition conditions such as the hydrogen dilution [12]. The bandgap can also be modified by alloying it with other atoms such as germanium, carbon or oxygen. The highest stabilized efficiency achieved for a single junction a-Si:H solar cell was 10.2 %. [13] One of the factors limiting the efficiency of a-Si:H solar cells is the defect density within the absorber material, which increases SRH recombination. Defects can be caused by impurities, dislocations, voids or dangling bonds, among others. Hydrogen is able to passivate some of these defects, reducing recombination in the material. In addition, a-Si:H suffers from light-soaking effects, which can lower the values of the external parameters of the solar cell. This degradation of amorphous silicon solar cells is known as the Staebler-Wronski effect. [14] Even though the principle behind the degradation process is not fully known, it is commonly believed that the principal cause of the Staebler-Wronski (SW) effect is the increase in metastable defects induced by light soaking. A feature of these light soaking effects is that it can be removed by thermal annealing. [15]

Another popular material to use in thin film silicon solar cells is nanocrystalline silicon (nc-Si:H). This is a heterogeneous material formed by silicon nanocrystals embedded in an amorphous silicon matrix. These grains give the material advantages with respect to a-Si:H, such as higher electron mobility. However, the grain boundaries can also be recombination centers. Therefore, nc-Si:H is hydrogenated for dangling bond passivation, which is especially important around the grain boundaries. The bandgap of the material is approximately 1.1-1.2 eV, roughly the same as crystalline silicon, with an indirect bandgap. This bandgap allows for higher utilizations of low-energy photons with respect to a-Si:H. An efficiency of 11.8 % was achieved for a single junction nc-Si:H solar cell. [16] This material does not suffer from the SW effect.

1.2.5 Multijunction solar cells

A multijunction solar cell is formed by stacking together several solar cells, usually made of absorber materials with different bandgap energies. [17] It utilizes the solar spectrum in a

different way than single junction solar cells. While in a single junction solar cell, all the absorbed light above the bandgap generates charge carriers in a single intrinsic layer; in a multijunction solar cell the light of the solar spectrum is preferentially absorbed in the various absorber layers. The top subcell absorber layer absorbs the highly energetic light in the blue region of the spectrum, while it is transparent to the light in the red region of the spectrum. Therefore, the red light would be able to reach the bottom absorber material, and be absorbed there. The optimum device should have a thin absorber layer with a high bandgap as the top absorber and a much thicker absorber layer with a lower bandgap in the bottom subcell, so that the produced photocurrent in both cells is approximately the same. Although multijunction cells with the same absorber material have been produced, such as a-Si:H/a-Si:H tandem cells, [18] their spectral utilization is lower than tandem cells using different materials.

There are several advantages of multijunction solar cells over single junction cells. First, higher utilization of the solar spectrum can be achieved by using materials with different bandgaps. This reduces the thermalization losses from the photons with energy higher than the bandgap energy. In addition, multijunction solar cells can achieve higher voltages, since more than one single junction solar cell is connected in series. However, fabricating multijunction cells having more than three junctions gives only a small increase in efficiency, which does not justify the increase in fabrication costs and complexity. [19] Therefore, the most studied thin film silicon multijunction cells are either double or triple junction cells. The highest efficiency reported for multijunction thin film silicon solar cells to date is based on a-Si:H/a-SiGe_x:H/nc-Si:H cell, with a 16.3 % initial efficiency. [20] However, when considering stabilized efficiencies, the a-Si:H/nc-Si:H/nc-Si:H configuration achieves the highest efficiency of 14.0 %. [21]

The two main challenges of multijunction solar cells are (i) minimizing the voltage losses at the interface between the subcells; and (ii) light management for an optimum spectral utilization within the different subcells. The first challenge is generally tackled by including a tunneling recombination junction (TRJ), where a layer is added to ensure current continuity at the interface between two subcells. This is usually done either by including a thin defective layer to enhance recombination, or a highly doped layer with low activation energy to enhance both recombination and tunneling. [22] The second challenge of light management can be tackled by bandgap optimization, current matching and substrate texturing. [23]

1.3 Photoelectrochemical(PEC) technology

Although the PV effect is typically used in PV solar cells, this is not its only application. The currents and voltages generated in a semiconductor device can also be used to drive electrochemical (EC) reactions such as electrolysis. A photoelectrochemical (PEC) device consists of a semiconductor in contact with an electrolyte. Figure 1.7 shows the general configuration of a PEC device for water splitting, and the corresponding band diagram at the semiconductor/electrolyte interface. The semiconductor material constitutes the photoelectrode, which could be a photocathode if the electrons are injected from the semiconductor into the electrolyte, or a photoanode if electrons are injected from the electrolyte into the semiconductor. The electrolyte provides the medium for the photoelectrochemical reaction (PEC) to occur, and the counter electrode completes the electrical circuit. When light is absorbed in the semiconductor absorber material, photons generate charge carriers. These charge carriers diffuse to the interface between the semiconductor and the electrolyte, where they are separated by the electric field of the depletion region at the interface, and they would drive the photoelectrochemical (PEC) reaction. This section deals with the challenges of PEC devices, focusing on their use to drive the water splitting and water treatment reactions.

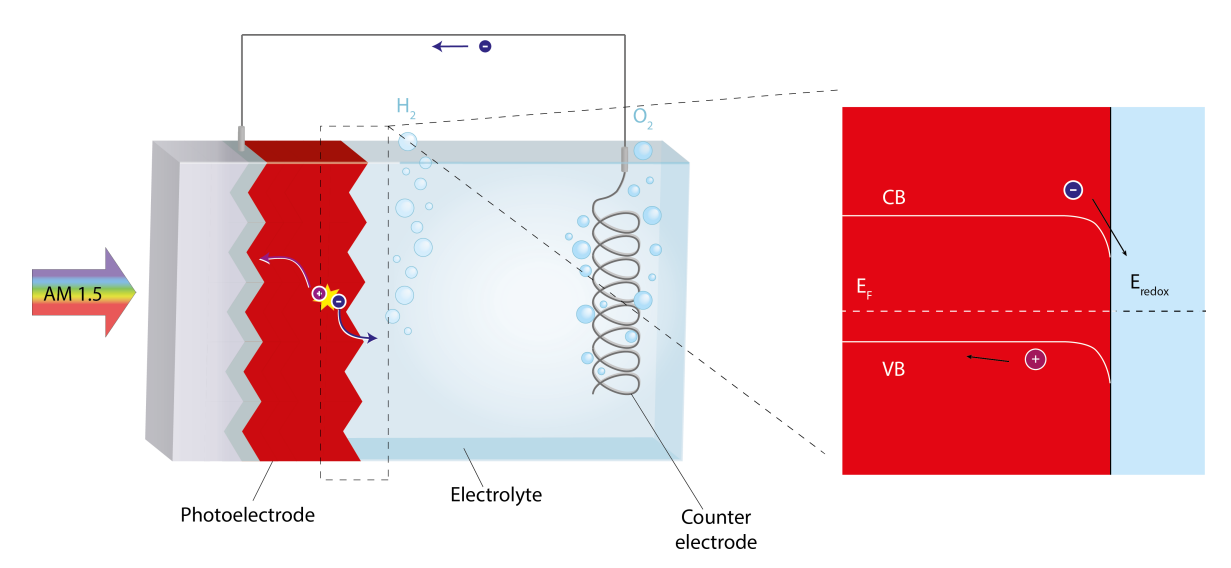


Figure 1.7: Example schematic of a PEC device for water splitting, including the photoelectrode, the electrolyte and the counter electrode; and the corresponding band diagram at the semiconductor/electrolyte interface.

1.3.1 PEC technology for water splitting

Energy storage is an important issue for the current energy market, especially regarding the balance between energy supply and demand. Up to 12 % of the total electrical energy used in 2008 had been stored at some point, and this percentage is expected to grow over 34 % in 2025. [24] Some of the most common large-scale storage technologies are pumped hydro storage (PHS), thermal energy storage (TES), compressed air energy storage (CAES), batteries, chemical storage (fuels), superconducting magnetic energy storage (SMES) and supercapacitors. [25] However, few of these technologies represent a feasible energy storage solution in the long term and at a large scale in terms of cost, power output, energy density and self-discharge rates. One of the most promising technologies is chemical storage, particularly the production of hydrogen using solar energy. Solar water splitting is able to produce highly pure hydrogen, which can be stored as a chemical fuel for long periods of time. [25] Hydrogen has an energy density several times higher than batteries, a fast response for energy release and low self-discharge rates with respect to other storage technologies [26] In addition, molecular hydrogen can react further with CO₂ to form simple hydrocarbons such as methane or methanol, increasing the energy density even further. [27] Therefore, solar fuels are a more suitable option for long-term energy storage compared to other available technologies.

When converting solar energy into a chemical energy carrier such as hydrogen, it must be noticed that water cannot be directly decomposed by light into oxygen and hydrogen because it is transparent to visible light. Therefore, a more efficient way to absorb light and drive the reaction is to use PEC devices. Figure 1.7 already showed the general configuration of a PEC device, and the corresponding band diagram of the semiconductor/electrolyte interface. Charge carriers are generated when the semiconductor absorber is illuminated, and they are separated and collected at the semiconductor/electrolyte interface to drive the PEC reaction. A PEC water splitting device was first demonstrated by Fujishima and Honda in a TiO₂ device. [28, 29] The redox reaction that describes this process can be written as [30]:

Oxidation (anode):
$$H_2O \rightarrow 2H^+ + 1/2O_2 + 2e^ E^0_{ox} = -1.23V$$

Reduction (cathode): $2H^+ + 2e^- \rightarrow H_2$ $E^0_{red} = 0V$
Overall redox reaction: $H_2O \rightarrow 1/2O_2 + H_2$ $E^0_{redox} = 1.23V$

From the above reactions, it can be seen that a minimum voltage of 1.23 V is required. Nevertheless in practice, energy losses in the PEC device translate into a need for additional overpotentials. Some of these energy losses are related to the electrolyte and contact resistance, the SRH recombination inside the semiconductor, the resistance for charge carrier injection at the semiconductor/electrolyte interface, or the catalytic energy losses. The resistive losses in the electrolyte depend on the distance between electrodes and the electrolyte conductivity. The losses due to recombination inside the semiconductor materials mainly depend on the quality of the material, surface passivation and internal electric field. The losses due to recombination at the semiconductor/electrolyte interface depend on the flat band potential of the photoelectrode (Figure 1.8), the catalyst used and the work function of the counter electrode material. [31] Overall, translating these loss mechanisms into voltage losses, a practical voltage of approximately 1.6 to 2 V is needed for the water splitting reaction to occur. [30] Finally, stability and cost considerations must also been taken into account.

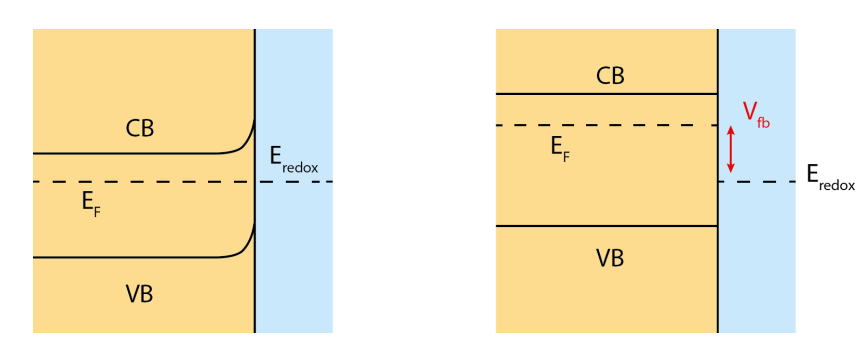


Figure 1.8: Schematic of the bandedge between a semiconductor and an electrolyte, where V_{fb} represents the flat-band potential.

In order to define the performance of a PEC device, the solar-to-hydrogen (STH) conversion efficiency is normally used. This definition assumes that each electron that reaches the solution is used to drive the desired PEC reaction. Moreover, the enthalpy of formation of hydrogen is used as an indication of the energy stored. Mathematically, the STH efficiency can be written as [32]

$$\eta_{STH} = \frac{J_{ph}1.23V}{P_{in}} \tag{1.6}$$

where η_{STH} is the STH efficiency, J_{ph} is the photogenerated current density and P_{in} is the incoming irradiance, which is usually taken as AM1.5 and 1000 W/m². It must be noted that often these measurements are performed at room temperature without any specific temperature control strategy.

There are several ways to achieve the necessary voltage to drive the PEC water splitting reaction using semiconductor materials. Some of the most important concepts are depicted in Figure 1.9, placed in a scale of a completely monolithically integrated PEC device (A) to a completely decoupled one (E). Intermediate devices include a monolithic photovotaic-electrochemical (PV-EC) device (B) in which the PV and EC components are directly in contact, but the semiconductor device does not rely on the semiconductor/electrolyte interface for quasi Fermi level splitting; external multijunction PV-EC devices (C), where the PV and EC components are no longer in direct contact, or external series connected PV-EC devices (D), where several PV devices are connected in series to achieve the required voltage for the solar water splitting reaction.

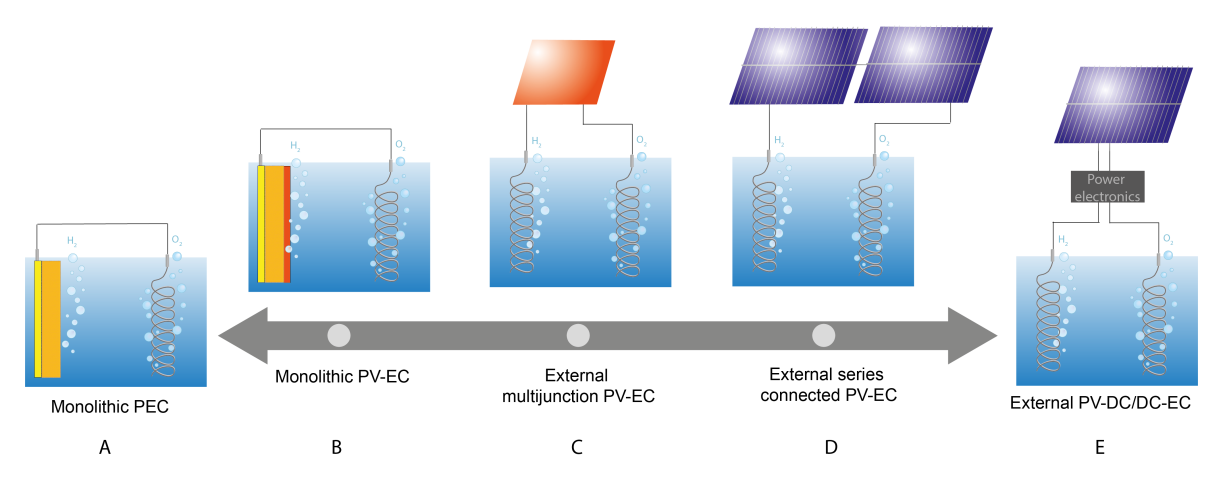


Figure 1.9: Scale of the different possible solar water splitting devices, from the monolithical phototelectrochemical (PEC) devices (A), where the charge carrier generation and the electrochemical reaction are totally coupled; to a PV-DC/DC-EC system (E), where the two elements are completely decoupled by a DC/DC converter. Some examples of intermediate devices include monolithical PV-EC devices (B), which refers to a buried PV junction directly in contact with water; external multijunction PV-EC devices (C), where the PV cell is outside the electrolyte but it still produces enough voltage by itself for the electrolysis reaction to occur; and external series connected PV-EC devices (D), where several cells are connected in series to produce the required voltage, but it does not include any additional electronic components.

In configuration (A), the charge carrier separation and collection happens due to the electric field created by the semiconductor/electrolyte junction. The quasi-Fermi level splitting in the semiconductor reaches up to the semiconductor/electrolyte interface. This interface is often the limiting factor for charge carrier separation and collection, since the conduction

and valence band edges of the semiconductor have to be aligned with the PEC reaction energy levels in the solution for an efficient charge carrier injection from the semiconductor to the electrolyte. If the solution has a very different electrochemical energy level (E_{redox}) compared to the semiconductor band energy levels, there is Fermi level pinning at the semiconductor/electrolyte interface, where the photovoltage is independent of the electrochemical potential. In these cases, the band bending at the semiconductor/electrolyte interface is fixed. The surface states, defined as surface electronic energy levels with energies different from the allowed energy states in the semiconductor, dominate the charge carrier injection process. This causes recombination and limits the conversion efficiency of the PEC device. [33] In addition, monolithic PEC devices use only one semiconductor absorber material. The high voltages needed for the water splitting reaction to occur translate into the need for a high bandgap absorber material, as the ones shown in Figure 1.10. However, absorber materials with high bandgap energies would absorb a smaller portion of the solar spectrum. Therefore, a balance is created regarding the ideal bandgap of the absorber material. Several semiconductor materials have been tested as photoelectrode for the realization of a photoelectrochemical (PEC) device, including TiO_2 [28, 34, 35], α -Fe₂O₃ [36, 37], WO₃, III-V technologies [38] or BiVO₄. [39]

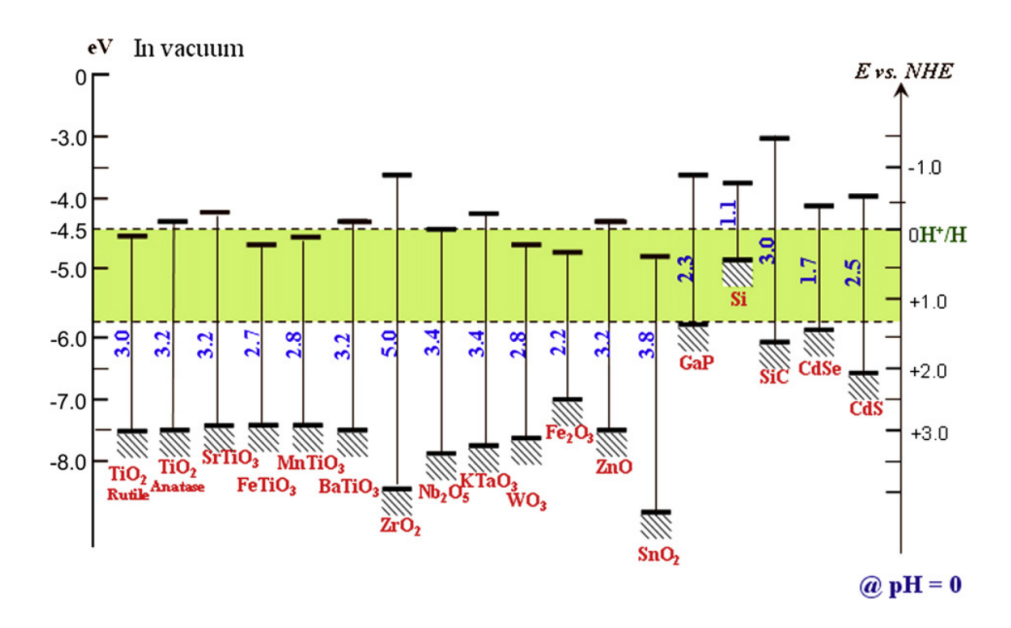


Figure 1.10: The band edge potentials of common semiconductor photoelectrode materials plot against the normal hydrogen electrode (NHE) at pH 0 and vacuum potential. [40]

Another option is to decouple the quasi-Fermi level splitting from the energy level of the reaction in the electrolyte. Previous research suggests the need for a buried junction between two semiconductors to separate and collect the charge carriers and prevent Fermi level pinning at the semiconductor/electrolyte interface. [41] Such a buried junction relaxes the conditions and design limitations of the PEC device. [42, 43] In addition, very few of the proposed semiconductor materials to be used as photoelectrodes have a high enough bandgap to provide the reaction without an external bias voltage [44, 45]. To achieve such a high voltage to drive the PEC reaction, several solar cells connected in series are needed. This can be done by many different configurations, as shown in Figure 1.9. Two of the most promising ones are to externally connect several PV cells in series (D) and to fabricate a monolithic multijunction PV device to produce the necessary voltage and current (B,C). Some of the highest solar-to-hydrogen (STH) efficiencies of stand-alone multijunction devices are depicted in Figure 1.11. The highest STH efficiencies have been obtained with a III-V monolithic based device, achieving 19.3 %. [46]

External series connected PV-EC devices (D) have the advantage of using readily available PV devices to achieve high STH conversion efficiencies, as shown in literature with three heterojunction cells in series combined with an electrolyzer based on earth-abundant materials, resulting in an efficiency of 14.2 %. [48] In addition, external series connected PV-EC can also result in a better current matching than multijunction PV-EC devices, especially at variable spectrum conditions, since all the cells connected in series would be of the same technology and would produce similar currents at different spectrum conditions. However, multijunction PV-EC devices (B,C) have the advantage of an overall better spectral utilization, and possibly lower resistive losses due to less cabling. In addition, since cell interconnections can be avoided, the final device could be more compact and easily produced, potentially lowering the cost.

Finally, a completely decoupled system could be designed (E), where the working conditions of the PV device do not depend on the EC component due to the DC/DC converter installed in between them. Since all these technologies are relatively mature, a 20.6 % STH efficiency was achieved, and a potential of 26.5 % was simulated as a theoretical limit. [49] However, it must be noticed that these approaches (E) have an increasing complexity, and thus achieving a similar efficiency with simpler, more compact devices (B, C) can be more cost effective.

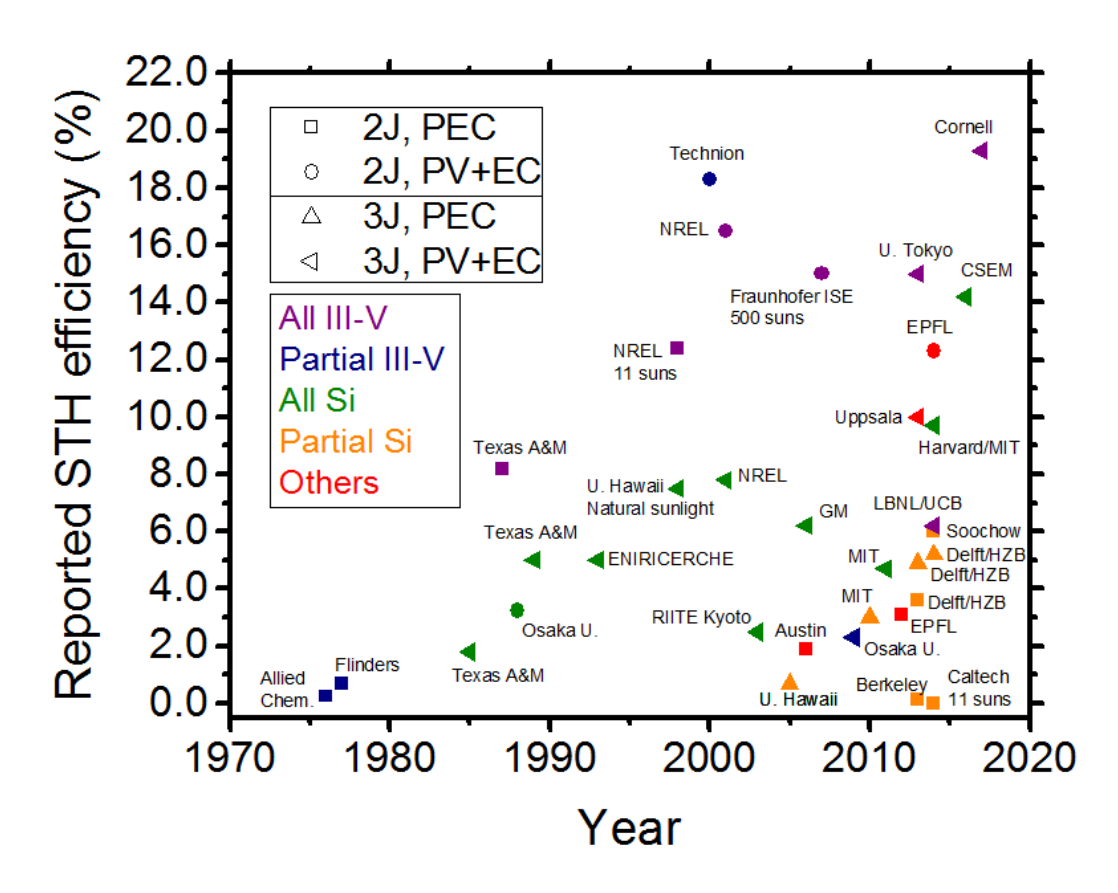


Figure 1.11: Reported solar-to-hydrogen (STH) efficiencies by year, absorber material and device structure. Updated from [47]

1.3.2 PEC technology for water treatment

Another important challenge that society faces is the access to clean drinkable water. Among the many pollutants present in water, organic molecules such as fertilizers or chemical and pharmaceutical industry waste are a challenging group of pollutants to treat. Traditionally, these pollutants were treated either by physical or chemical methods. However, physical methods such as filtration do not eliminate the pollutants but only transfer them from one physical phase to another. Chemical methods are able to eliminate the pollutants only up to certain concentrations, and are not always able to achieve complete conversion into CO₂ and H₂O, also called mineralization. Therefore, an alternative to conventional methods is needed. Advanced oxidation processes (AOPs) for water treatment are recently becoming more popular due to their capability to achieve low concentrations of organic contaminants

while maintaining the costs low. Particularly, PEC water treatment can reduce the energy demand of organic pollutant treatments, addressing simultaneously the global energy and water scarcity challenges.

PEC water treatment devices absorb light in a semiconductor material, generating charge carriers. These charge carriers are separated and collected at the semiconductor/liquid interfaces, generating OH radicals when reacting with the water in the solution. The direct electrochemical oxidation and reduction half-reaction can be written as [50]

Oxidation (anode): $H_2O \rightarrow OH + H^+ + e^-$ Reduction (cathode): $H^+ + e^- \rightarrow 1/2H_2$ Overall redox reaction: $H_2O \rightarrow OH + 1/2H_2$

The OH radicals are able to promote the degradation and mineralization of organic pollutants. [51] If the bond of the organic molecules with the semiconductor surface is strong enough, they could even be oxidized directly by the holes instead of the OH radicals. [52] The generation of charges in PEC devices is very similar to the one previously described for water splitting. The difference between the PEC devices designed for water splitting and water treatment lies in the reactions at the semiconductor/electrolyte interface.

There are many organic pollutants that could be degraded using the PEC technology, and each pollutant has slightly different requirements for the PEC device. Phenol is often used as a benchmark of organic pollutant degradation due to its relative ease for detection. The degradation pathway for phenol on a semiconductor under visible light irradiation is presented in Figure 1.12, showing the complete mineralization process of phenol. Hydroxyl radicals produced on the semiconductor surface react with phenol to produce hydroquinone. In addition phenol can also react with hydroxyl radicals to form resorcinol and catechol. [53] Hydroquinone can react with OH to form benzoquinone. Upon extended photo-oxidation, the benzene ring can open due to continuous oxidation, leading to the formation of aliphatic compounds, like formic acid, and ultimately mineralizing to form carbon dioxide (CO₂) and water upon complete oxidation. [53] PEC oxidation is able to remove toxic organic pollutants, ecologically hazardous cyanides and other residual compounds even at low initial pollutant concentrations, being an ideal candidate for advanced water purification. [51] The level of pollutant degradation and mineralization can be measured by two methods. First,

the concentration of phenol remaining in the solution can be measured by using UV spectroscopy on the solution. Second, the final mineralization of phenol can be estimated by carbon oxygen demand (COD) measurements. In this method, the remaining organic compounds are measured, giving an idea of the overall organic pollutants still in water. The final phenol concentration and remaining COD can differ significantly, since the reaction of phenol degradation uses only one OH radical, while complete mineralization requires at least 28 OH radicals.

Figure 1.12: Photo(electro)catalytic degradation pathways of phenol on a semiconductor under visible light irradiation.

The photoactivity of a PEC device strongly depends on the configuration and material properties of the electrode, as well as the presence of an applied voltage. [54, 55] PEC treatment of organic compounds has been widely studied since the first experiments by Carey et al. in 1976. [56] A wide variety of semiconductors have been tested as absorbers for PEC devices, such as TiO₂, [57–59] ZnO, [60], SnO₂, [61], WO₃ [62, 63] or bismuth based compounds. [64, 65] In particular, TiO₂ has often been used as the semiconductor of choice for photooxidation of pollutants, since it is cheap and chemically stable, [66] and has relatively good conductivity and band alignment with the PEC reaction energy levels in the solution. [67] However, its bandgap energy is rather high (3.2 eV), [68] meaning that it needs an artificial UV light source to excite enough charge carriers to efficiently degrade organic pollutants.

Artificial UV light sources are very energy intensive, making the process less cost-effective. In addition, PEC water treatment devices are dependent on an external applied voltage to overcome the energy barriers of the reaction. These challenges can be addressed by taking a similar approach than in the case of water splitting, by using lower bandgap materials and multijunction devices.

1.3.3 Areas for optimization for PEC device design

The areas for optimization for PV device design outlined in Section 1.2.3 are still valid for PEC devices. However, PEC devices present additional restrictions and considerations than those for PV devices. The additional level of complexity added in PEC devices is depicted in Figure 1.13. In this case, the areas of interest have been defined in a more general way to encompass all the challenges and considerations of PEC devices. The areas of interest have been defined as thermodynamic considerations, kinetic considerations, optical considerations and stability considerations.

Thermodynamic considerations. In a PEC device, the maximum energy that can be extracted from the system is related to the formation enthalpy of the molecules involved in the reaction. When translating these energies into voltages, the voltage produced by the semiconductor device should match with the necessary voltage for the reaction to optimize the spectral utilization. This optimization can be done by tuning the semiconductor bandgap or by using multijunction devices.

Kinetic considerations. In addition to the difficulties collecting charge carriers in a PV device and the recombination losses previously described, PEC devices present additional challenges related to the semiconductor/electrolyte interface. The band alignment of the Fermi level of the semiconductor with the redox reaction energy levels would determine the losses related to charge carrier injection from the semiconductor into the electrolyte. In addition, surface states related to the catalyst or other particles at the interface can affect the injection of charge carriers into the electrolyte, and therefore the efficiency of the PEC device. This challenge can be addressed by including additional buffer layers at the semiconductor/electrolyte interface to improve the band alignment at this interface. Finally, using a catalyst would reduce any overpotential needed and increase the selectivity to target

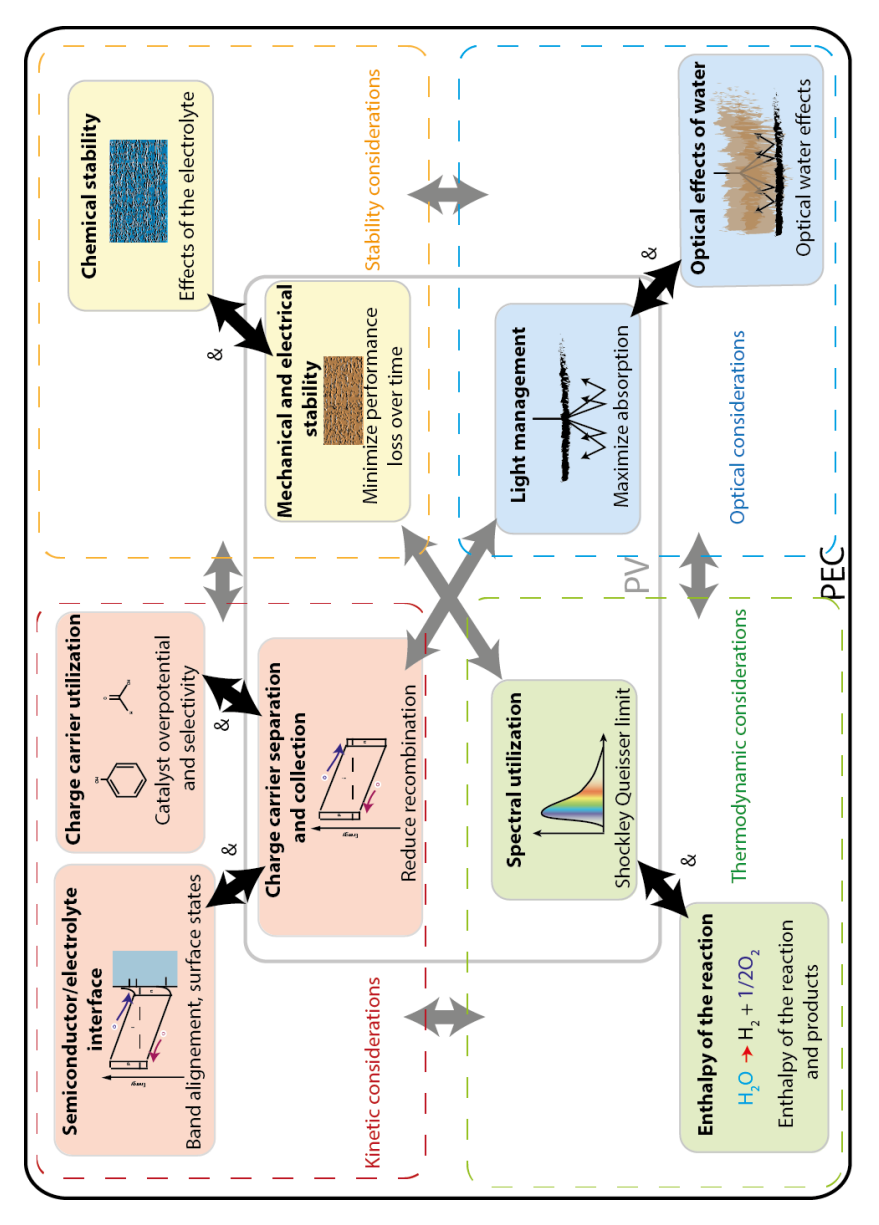


Figure 1.13: Schematic representation of the main areas for optimization involved in a PEC device

the desired chemical molecules, increasing the efficiency of the process by effectively utilizing the collected charge carriers to drive the target reactions.

Optical considerations. Light management can become more complicated in PEC devices with respect to PV devices, since there is less control over the media surrounding the semiconductor. The electrolyte must be considered when designing PEC devices, since it may absorb a fraction of the light. If the electrolyte is placed at the back of the device, the back reflector configurations that can be included in the device might be limited. On the other hand, if light passes through the electrolyte before reaching the semiconductor device, it would be partially absorbed. Therefore, the effects of the electrolyte must be considered when designing light management techniques in PEC devices.

Stability considerations. PEC devices are in direct contact with the electrolyte, which is often either acid or basic. This adds and additional source of chemical instability for the PEC device. Protective layers and alternative device configurations can be considered to limit the damage that the electrolyte might cause to the semiconductor device.

1.4 Research Questions and Outline of this Thesis

The aim of this work is to improve the PEC stand-alone device performance to either produce hydrogen as a fuel or degrade organic pollutants. To achieve this, the different areas of interest regarding PEC and PV device design have been explored, focusing on how to approach the different design challenges within these areas. Even though the general challenges of designing these two types of devices have many elements in common, there are also some differences in the fundamentals of each reaction and the level of maturity of the use of PEC devices for each of the reactions. Therefore, the research questions in this thesis are divided between the solar water splitting and water treatment reaction as follows:

Solar water splitting

• What is the role of the semiconductor/electrolyte interface in terms of charge carrier separation and collection, and band alignment? (Design challenges: charge carrier collection and utilization)

- What are the design parameters of a PV or PEC device that facilitate the necessary voltage at the operational point for water splitting? (Design challenges: charge carrier separation and collection, spectral utilization, enthalpy of the reaction)
- What strategies can be considered in terms of light management and optimum device architecture to achieve highly efficient solar water splitting? (Design challenges: spectral utilization, enthalpy of the reaction light management)

Solar water treatment

- What is the role of the semiconductor/electrolyte interface in terms of charge carrier separation and catalytic activity? (Design challenges: charge carrier collection and utilization, spectral utilization)
- What is the interplay between operational voltage and current applied to the (P)EC device? (Design challenges: charge carrier collection and utilization, spectral utilization, enthalpy of the reaction)
- What is the optimum device architecture to achieve efficient solar water treatment? (Design challenges: charge carrier collection and utilization, spectral utilization, enthalpy of the reaction)

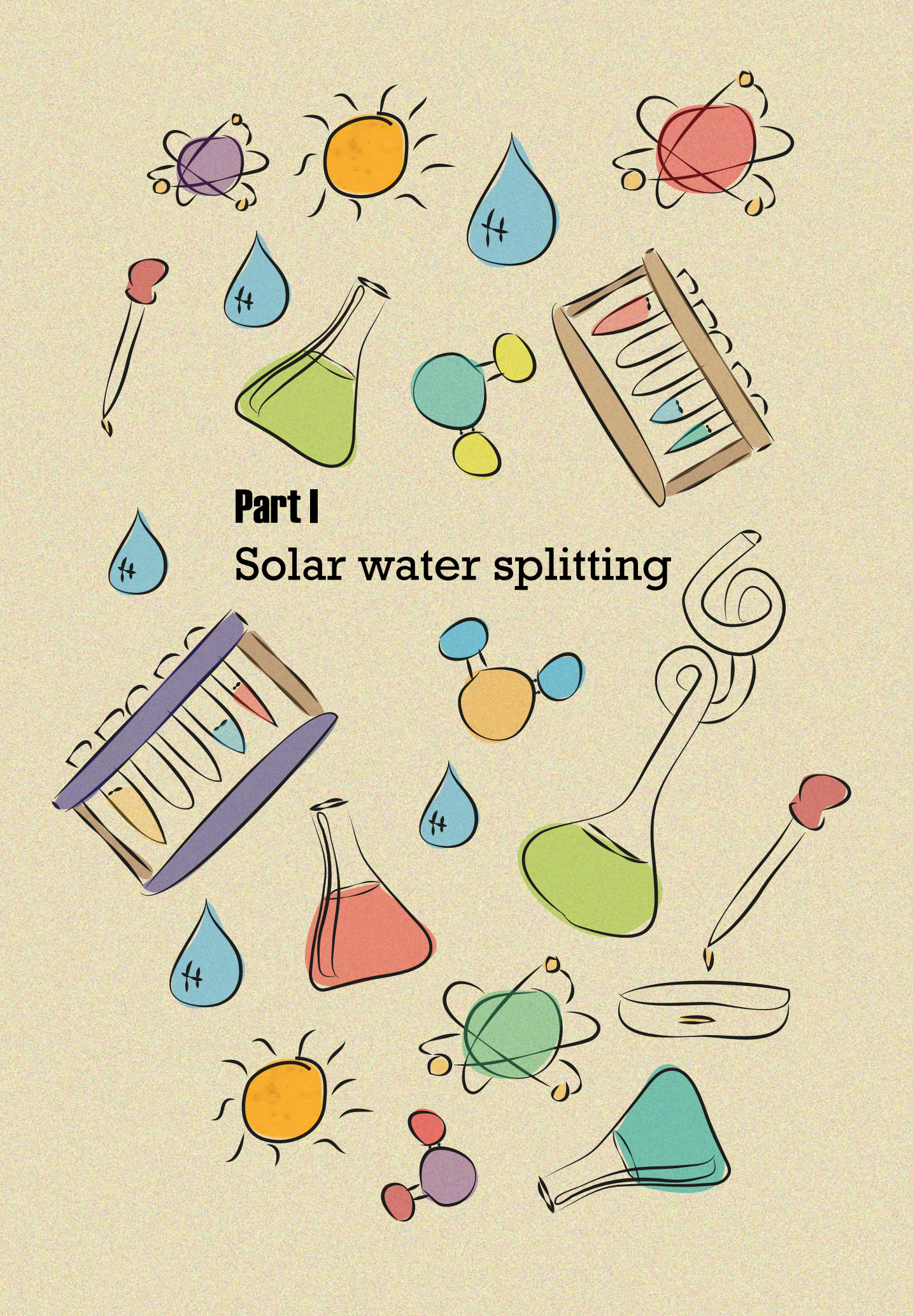
The thesis is divided in two main parts, corresponding to the two PEC reactions previously outlined: the first one regarding solar water splitting devices, and the second one regarding the photo-oxidation of organic pollutants, focusing on phenol, chlorophorm and methylene blue. Each chapter in these two parts addresses one or more of the design challenges of PEC devices.

Part I consists of three chapters. In Chapter 2, a photocathode based on a-SiC:H has been used to drive the water splitting reaction, concentrating on the effect of the back surface field and the semiconductor/electrolyte interface. a-SiC:H was chosen as photocathode material for its relatively high stability in the electrolyte. [69] From this research, it is apparent that a multijunction solar cell would be the most efficient approach to solar water splitting. Chapter 3 deals with the design of a hybrid monolithic multijunction solar cell, consisting of a micromorph thin film silicon solar cell on top of a SHJ solar cell (a-Si:H/nc-Si:H/c-Si). The focus of this research is first on the TRJ to maximize the open-circuit voltage and fill factor of this structure, as a demostrator for this hybrid solar cell concept. Once the TRJs of this

multijunction device have been optimized, the limiting factor is related to light management. Therefore, **Chapter 4** focuses on optimizing the substrate texture and absorber bandgap and thickness to achieve high current densities. Once the optimum device is developed, it is also tested in an electrolyzer to show its applicability for water splitting.

Part II consists of two chapters. In Chapter 5, a photoelectrode based on BiVO₄ is studied from a material science point of view. Moreover, this photoelectrode is combined with a thin film silicon solar cell to fabricate a stand-alone device for treatment of organic pollutants. Chapter 6 studies the effect of using a PV+EC approach instead of a PEC approach, concentrating in both the effect of using an electrochemical (EC) system and different photovoltaic (PV) devices. In addition, a complex interplay between the voltage and total power fed to the EC system is established.

Finally, Chapter 7 outlines some design parameters and device configurations that can help tackling several design challenges of PEC devices. In addition, some of the impacts of this research in a broader context are also discussed, with special focus on the possible upscaling of PEC devices.



2

Solar water splitting using a-SiC:H photocathodes

This chapter is based on the following publication:

P. Perez-Rodriguez, D. Cardenas-Morcoso, I.A. Digdaya, A. Mangel Raventos, P. Procel, O. Isabella, S. Gimenez, M. Zeman, W.A. Smith, A.H.M. Smets. Improving the back surface field on an amorphous silicon carbide (a-SiC:H) thin film photocathode for solar water splitting. *ChemSusChem* 11(11): 1797 –1804, 2018.

2.1 Introduciton

The growing world energy demand and the depletion of fossil fuels require alternatives to the current energy system. Solar energy offers a cleaner and more sustainable alternative due to the high amount of solar energy availability and relatively easy installation and maintenance of solar systems. However, due to daily and seasonal fluctuations in irradiance availability, energy storage plays an important role in the implementation of solar energy. Daily irradiance variations can be tackled by using batteries, but seasonal variations need alternative storage methods that offer a cheaper and more energy dense solution. [24] Hydrogen is a plausible option to tackle this problem, since it can be easily stored in tanks or combined with carbon dioxide (CO₂) to form other hydrocarbons with higher energy density and low cost. Moreover, the resulting products can be stored for long periods of time with minimum losses such as self-discharge. [27] Direct hydrogen production using solar driven water splitting has attracted considerable attention in the last years. [70–74] In particular, photoelectrochemical (PEC) devices provide a simple and elegant solution to hydrogen production using solar energy.

Photoelectrochemical production of hydrogen from water splitting is based on a material which absorbs light and generates electron-hole pairs. These charge carriers are then separated within the semiconductor and used to drive the two half-reactions at the cathode and anode, which produce highly pure hydrogen and oxygen on the electrode surfaces, respectively. There are several characteristics that a semiconductor needs to fulfil for its use in a PEC device: adequate optical properties, good charge separation, chemical stability, and correct band alignment with respect to the potentials of the water splitting reaction. [74] In addition, the materials used need to be earth-abundant in order to achieve a cost-effective solution. The PEC field has dedicated extensive effort to the search for a suitable material to drive the water splitting reaction. Among the thin-film semiconductors based on metal oxides tested for this application are TiO_2 , [28, 34, 35] Fe_2O_3 , [37, 75] WO_3 [38] or $BiVO_4$. [39] These semiconductors can produce relatively high photovoltages, due to their relatively large bandgap energy. However, they absorb only a small fraction of the solar spectrum. Therefore, there has recently been a shift to investigate non metal-oxide photolectrodes with smaller bandgap energies, such as silicon, which in theory could enhance the amount of photocurrent generation. [76–78] Zhu et al. [69] proposed an amorphous silicon carbide (a-SiC:H) photocathode with a bandgap energy of 2.0 eV. Moreover, Han et al. [79] introduced a gradient boron doped homojunction to improve the internal electric field and charge carrier collection. Thus, the attention has recently started to shift from material science towards device architecture design, using strategies such as the inclusion of different doped layers, [39, 79, 80] and the introduction of a surface field at the semiconductor/electrolyte interface for a more selective charge carrier collection. [81] These results show that not only the material used as photoelectrode is important, but also the charge carrier separation and collection. Therefore, the optimization of internal electric fields can play an important role on the performance of PEC devices. [82] However, the introduction of an internal electric field also modifies the interface energies between the semiconductor and the device, which might be detrimental to the charge carrier injection into the electrolyte. Thus, two main limiting factors to consider when designing the device architecture of a photoelectrode can be defined: the charge carrier separation and the charge carrier injection into the electrolyte. This paper aims at studying the principles behind the charge carrier separation, collection and injection of a photocathode when modifying the semiconductor/electrolyte interface.

In order to improve the charge carrier collection, the different electronic junctions formed in the device must be optimized. [83] If the interface contains many defects, Shockley-Read-Hall (SRH) recombination, also called defect-assisted charge carrier recombination, can occur at the junction. Homojunctions such as the (p)a-SiC:H/(i)a-SiC:H previously introduced lead to limited SRH recombination due to the reduced amount of defects such as dangling bonds or lattice mismatch at the interface. That is not the case with some other junctions like heterojunctions, semiconductor/metal or semiconductor/electrolyte junctions, where the differences between the material lattice, possible dangling bonds, voids and other defects can lead to higher levels of SRH recombination at the interface. To avoid this effect, an electric field and selective contacts can be introduced near the surface to screen away the minority charge carriers. This concept has already been successfully used for semiconductor/metal contacts in the photovoltaic (PV) field. [84, 85]

The present study focuses on the improvement of an a-SiC:H photocathode by using the concepts developed in the PV field such as passivation of interfaces, selective contacts and electric fields by optimizing a back surface field. In addition, the chemical reaction at the interface must be considered, and the band alignment between the energy levels of the reaction and the semiconductor bandgap energies must be considered. Here, the know-how of the PV field regarding the enhancement of the internal electric field and charge carrier collection

is combined with the PEC expertise on the solar water splitting reaction and charge carrier injection to develop a more efficient PEC device. To improve the overall performance of a-SiC:H photocathode, the effect of introducing a back surface field by adding an n-doped nanocrystalline silicon oxide (nc-SiOx:H) layer to create a p/i/n structure was studied. The characteristics of nc-SiOx:H can be tuned depending on the oxygen content, [86] and therefore it is widely used as an n-layer for thin film silicon solar cells. This layer enhances the electric field created inside the semiconductor, which facilitates the charge carrier separation. In addition, it serves as a selective contact to improve charge carrier collection, and to passivate surface defects that can lead to SRH recombination. Furthermore, when an undoped TiO2 protective layer is introduced at the semiconductor/electrolyte interface, both the band alignment and chemical stability can be improved. [87, 88]

2.2 Materials and methods

Photocathode deposition. The a-SiC:H and nc-SiO_x:H layers were deposited using Radio Frequency Plasma Enhanced Chemical Vapor Deposition (RF-PECVD). Asahi UV-type, consisting of a textured glass with an FTO coating, was used as a substrate. A p/i or p/i/n structure was used, in which the p-type layer was a 10 nm film of boron doped hydrogenated silicon carbide ((p)a-SiC:H), the i-type layer was a film of intrinsic hydrogenated amorphous silicon carbide ((i)a-SiC:H), and the n-type layer was phosphorous doped nanocrystalline silicon oxide ((n)nc-SiO_x:H). Unless otherwise stated, the i-layer was 100 nm and the n-layer was 20 nm. The precursor gases used were SiH₄, CH₄, H₂ and CO₂. Doping of p and n layers was was realized using the gases B₂H₆ and PH₃, respectively. Different layers (p, i, n) were deposited in different chambers of an Elettrorava cluster PECVD tool to avoid cross contamination. As a front contact, a 300 nm Al stripe was deposited on the FTO by electron beam evaporation in a Provac evaporator, and then a silver wire was attached to it using carbon paste.

For some of the PEC measurements, a titanium oxide (TiO_2) layer of 20 nm was deposited using an in-house Atomic Layer Deposition (ALD) system located at TU Delft. During deposition, the substrate temperature was 200 °C. Tetrakis (dimethylamino)-titanium (TDMAT) and water were used as precursors for the Ti and O, respectively. The growth rate was 0.6-0.8 \mathring{A} per cycle, measured by ellipsometry. The samples were further annealed at 300 °C for an

hour to crystallize the material. Subsequently, a layer of 1 nm Pt catalyst was deposited using sputtering with radio frequency (RF) in a PREVAC sputtering tool, with a deposition rate of 0.5-0.6 \mathring{A}/s . This relatively high deposition rate allows the formation of nanostructures, which improve its catalytic activity. [89]

Solid-state characterization techniques. The external quantum efficiency (EQE) represents the percentage of incident photons on the device that produce charge carriers that would be collected. Here, the EQE was measured with an in-house system in the PVMD group, TU Delft, consisting of a Xe lamp attached to a monochromator. A Ge calibration diode was used for correcting the spectrum. When measuring EQE, a back contact of 200 nm Ag, 30 nm Cr and 500 nm Al was deposited by physical evaporation on the photocathode. The short circuit current was obtained by integrating the EQE weighted with the AM1.5 solar spectrum.

The solid state measurements of the JV characteristics were done under a double lamp Class AAA Wacom solar simulator. Standard Test Conditions (STC) were maintained by a Julaboo cooling system integrated in the measurement stage. When measuring solid-state JV curves, a metal back contact was also deposited, defining a cell area of 0.16 cm². The short circuit current density (J_{SC}) obtained from these measurements was normalized by the J_{SC} obtained by integrating the EQE output throughout the AM1.5 spectrum.

Finally, amorphous silicon (a-Si:H) is known to degrade under illumination due to the Staebler-Wronski effect [14], related to metastable defects inside the material. In order to study if a-SiC:H has a similar behaviour, the a-SiC:H cells with a back contact were exposed to constant illumination of 1 sun at 25 o C for 1000 h, and the solid-state JV characteristics of these cells were measured several times during this process. The light-induced degradation produced is presented here as the normalized value of the external parameters with respect to the initial state.

Photoelectrochemical (PEC) techniques. The JV characteristic as a PEC device was measured using an aqueous 0.2 M potassium hydrogen phthalate (Alfa Aesar, 99.99%) solution at pH 4 as electrolyte. The measurements were carried out in a 3 electrode configuration,

as shown in Figure 2.1, with an Ag/AgCl reference electrode (XR300, Radiometer Analytical) and a Pt wire counter electrode. This configuration was chosen to focus on the photocathode performance, independently from the anode behaviour. The solar simulator used was a Newport Sol3A Class AAA. The illumination area in contact with the solution was a 3 mm radius circle, with a total area of 0.283 cm². Moreover, to determine the stability in the electrolyte, chronoamperometry measurements were performed, where the current was measured on time at a constant voltage applied.

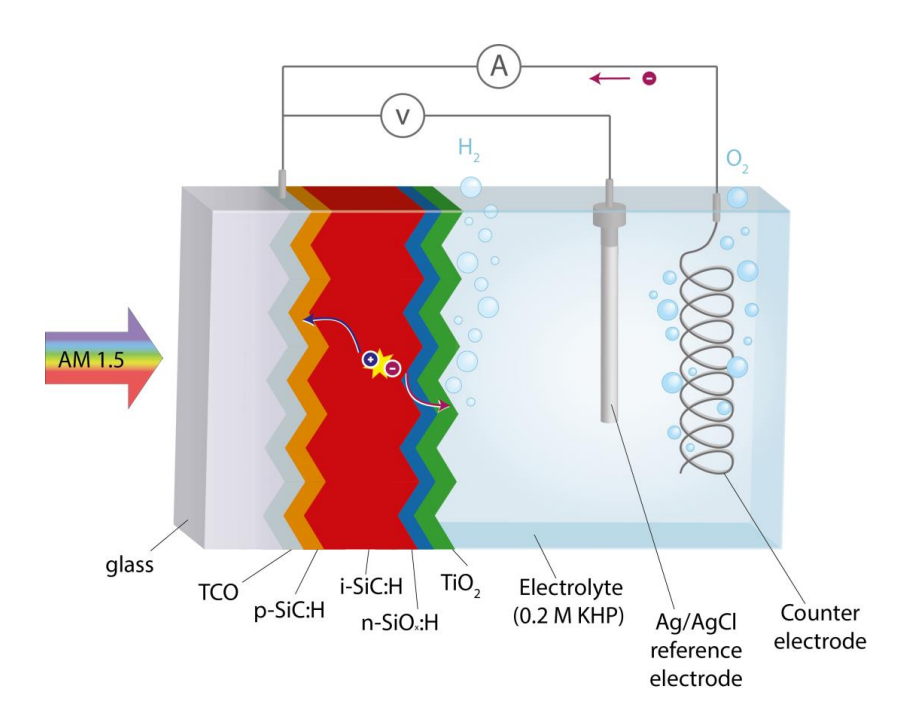


Figure 2.1: Schematic representation of the photoelectrochemical measurements carried out in a three-electrode configuration.

Electrochemical Impedance Spectroscopy (EIS) measurements were performed in the dark on an (n)nc-SiO_x:H layer of 100 nm deposited on a Asahi substrate, and on a 100 nm ${\rm TiO_2}$ sample in order to determine the flatband position of the relevant interfaces. EIS measurements were also carried out on the full photocathodes consisting of a-SiC:H and a-SiC:H/ ${\rm TiO_2}$ structures. A Metrohm Autolab potentiostat was used. Impedance data were collected between 10^{-2} and 10^6 Hz using a 20 mV amplitude voltage perturbation and analysed with the ZView software (Scribner associates). Finally, to better understand the obtained behaviour, electrical simulations were performed using the SENTAURUS software.

2.3 Results and discussion

Including an n-layer on an amorphous silicon carbide (a-SiC:H) photocathode is expected to improve its performance due to a better charge carrier separation and collection, and a reduction in the SRH recombination. Previously, protective layers such as TiO_2 have demonstrated not only to improve stability, but also to create a back surface field, improving the carrier injection at the semiconductor/electrolyte interface. [82] However, TiO_2 has a relatively high density of states and a relatively high lattice mismatch with a-SiC:H. [87] This causes recombination at the a-SiC:H/ TiO_2 interface, and therefore limits the photoelectrode efficiency. In addition, the electric field produced is lower, since TiO_2 has a lower donor density. Alternatively, a phosphorous doped nanocrystalline silicon oxide ((n)nc-SiO_x:H) could be included in this structure. Phosphorous doped nanocrystalline silicon oxide, (n)nc-SiO_x:H, is often used in thin film silicon solar cells as an n-layer to improve the internal electric field and charge carrier selectivity, in addition to its favourable optical properties. [86, 90] Thus, it is expected to improve the performance of the a-SiC:H photocathode as well.

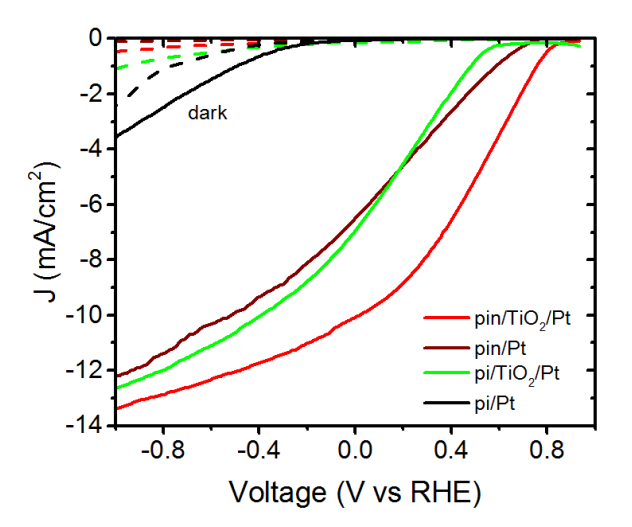


Figure 2.2: JV characteristics as a PEC device for the different samples with and without an n-layer, and with and without TiO_2 in a three-electrode configuration.

Figure 2.2 shows the photoelectrochemical behaviour of different a-SiC:H photocathodes with and without a (n)nc-SiO_x:H layer and with and without a TiO₂ layer. These results show that the introduction of a back surface field, either by introducing an (n)nc-SiO_x:H or a

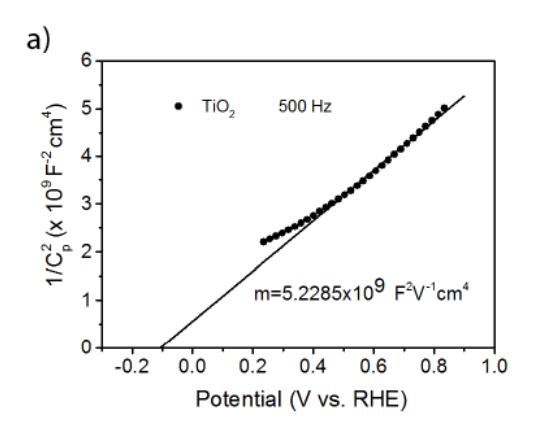
naturally n-type TiO_2 layer, largely improves the onset potential of the photocathode, from approximately -0.4 V vs. RHE to about 0.6-0.7 V vs. RHE. The photocathode with only the $(\text{n})\text{nc-SiO}_x$:H layer has a slightly higher onset potential, but the one with only TiO_2 presents a steeper JV slope, indicating a lower series resistance, which suggests that the injection of charge carriers into the electrolyte is facilitated. This might be due to a better band alignment of the TiO_2 , which would reduce the resistance at the TiO_2 /electrolyte interface. Finally, by combining both layers, the performance of the photocathode is further improved, resulting in onset potentials higher than 0.8 V vs. RHE, a steep slope indicating lower series resistances, and a current density of 10 mA/cm² at 0 V vs. RHE. This current density is comparable to other state-of-the-art devices, with current densities ranging between 8-12 mA/cm² for a-SiC:H photocathodes. This study focuses on analysing the fundamental semiconductor physics associated with these high performances. First, the limiting mechanisms (charge carrier separation or injection) in each case are discussed, and then further optimizations are presented.

Analysis of the Limiting Mechanisms The main two limiting mechanisms in these devices are considered to be the charge carrier separation and collection, and the charge carrier injection into the electrolyte. The effects observed in Figure 2.2 have been associated with these two mechanisms. In order to confirm the effect of the band alignment and reduced series resistance of the (n)nc-SiO_x:H and the TiO₂ layer with the electrolyte, an EIS study at a range of frequencies $(10^{-1}-10^5 \text{ Hz})$ has been performed to identity the most suitable frequency to carry out a single frequency Mott-Schottky analysis. In this analysis, the capacitance is the depletion layer capacitance. Figure 2.3 shows the Mott-Schottky plots of the two materials in order to compare the band alignment effects of a (n)nc-SiO_x:H and a TiO₂ layer in contact with the electrolyte. [81]

From the dark EIS measurements, the flat band potential of (n)nc-SiO_x:H, V_{fb} , can be calculated by using the relation [91]

$$\frac{1}{C^2} = \frac{2}{e\epsilon_0 \epsilon_r N_D} \left(V - V_{fb} - \frac{kT}{e} \right) \tag{2.1}$$

where C represents capacitance, e is the elementary charge, ϵ_0 is the permittivity in vacuum, ϵ_r is the relative permittivity of the (n)nc-SiO_x:H, k is the Boltzmann constant and T is the temperature, taken as 298 K.



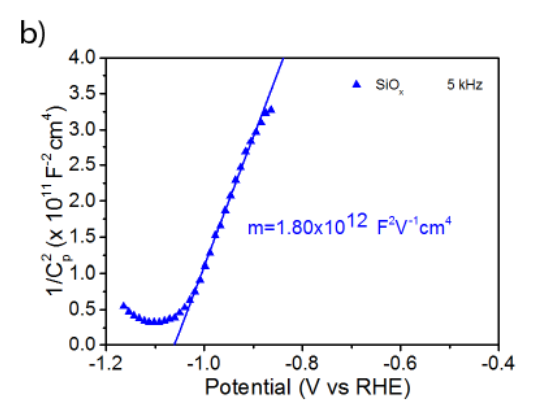


Figure 2.3: Mott-Schottky plots of a) a 100 nm TiO_2 layer, and b) a (n)nc-SiO_x:H layer with thickness of 100 nm. The variable m indicates the slope of the fitted linear function.

The flatband potential can be calculated from the intercept of the Mott-Shottky plot with the voltage axis displayed in Figure 2.3, as

$$intercept(voltage_{axis}) = V_{fb} + \frac{k_B T}{e}$$
 (2.2)

The obtained flatband potential estimates are -0.13 V vs. RHE for the TiO_2 sample of 100 nm, and -1.06 V vs. RHE for the case of 100 nm (n)nc- SiO_x :H samples. These values were used in further simulations of the different band diagrams in Sentaurus software, shown in Figure 2.4. These simulations estimate the energy band diagram structure of an entire structure based on the individual film properties.

Since the donor density of (n)nc-SiO_x:H is expected to be larger compared to TiO₂ due to the intentional doping introduced, the band alignment of (n)nc-SiO_x:H with the electrolyte is less optimal. This has been confirmed by measuring the activation energy of the layers, which represents the difference between the conduction band and the Fermi energy level. The activation energy was measured as 66.03 meV for (n)nc-SiO_x:H and 266.36 meV for TiO₂. The higher flat band potential of (n)nc-SiO_x:H suggests a higher band bending at the semiconductor/electrolyte interface, as it is shown in the electrical simulations presented in Figure 2.4. The higher flatband potential of (n)nc-SiO_x:H suggests a higher band bending at the semiconductor/electrolyte interface, creating the energy barrier shown in Figure 2.4d), leading to charge recombination at this interface. On the other hand, TiO₂ has a better alignment with the solution, where the flatband potential is close to zero. If TiO₂ is used at the surface of the (n)nc-SiO_x:H samples, the energy barrier at the interface with the

electrolyte is reduced, as shown in Figure 2.4b), facilitating charge injection and reducing recombination. This could explain the differences observed between the p/i/n/Pt and the $p/i/TiO_2/Pt$ photocathodes. It must also be noted that the $(n)nc-SiO_x:H$ samples were not stable in the solution, creating uncertainities in the measurement. It is thus possible that the flatband potentials of this material are even more negative, highlighting the benefits of adding a TiO_2 layer on the surface. However, $(n)nc-SiO_x:H$ improves the internal electric field and charge carrier collection selectivity. The $p/i/n/TiO_2/Pt$ system outperforms the $p/i/TiO_2/Pt$ system due to the effects of the interface between (i)a-SiC:H and TiO_2 , where the charge carrier selectivity and electric field produced is not as strong as with the $(n)nc-SiO_x:H$. Another factor that these simulations show is the creation of a small energy barrier at the $(n)nc-SiO_x:H/TiO_2$ interface due to the work function of these different layers. However, the disadvantage of this interface is overcome by the advantages of an improved internal electric field and band alignment.

To deconvolute the surface effects of this combination of layers, an EIS analysis was performed for the (n)nc-SiO_x:H and (n)nc-SiO_x:H/TiO₂ samples, as shown in Figure 2.5. By fitting the resulting data to the Randles'equivalent circuit, the resistances and capacitances at the semiconductor/electrolyte interface could be obtained. It can be seen that the resistance at the interface is higher for the case of the (n)nc- SiO_x :H/TiO₂ combination both in dark and illuminated conditions. This is probably caused by the additional resistances included by the TiO₂ layer. This was confirmed by measuring the lateral conductivity of the layer at 25 °C, which resulted in a value of 0.304 S/cm for the (n)nc-SiO_x:H and 6.60 10^{-5} S/cm for the TiO₂. Nevertheless, the reduction of the resistance upon illumination is higher when TiO₂ is included due to a better charge carrier injection from the semiconductor into the electrolyte. Regarding the capacitance, both the (n)nc-SiO_x:H sample and (n)nc-SiO_x:H/TiO₂ combination show a fairly constant capacitance with voltage, and an increase when illuminated with respect to dark conditions. This suggests the possibility of a double layer at the interface in both cases. The overall capacitance is however higher in the (n)nc-SiO_x:H sample, which could stem from photocorrosion, but it does not appear in the other sample due to the protection that TiO_2 offers.

To explore if these trends can be extrapolated to the whole device, the same measurements were performed on p/i/n a-SiC:H samples, with and without a TiO₂ layer, as shown in Figure 2.6. The impedance spectroscopy measurements carried out for this analysis did only show

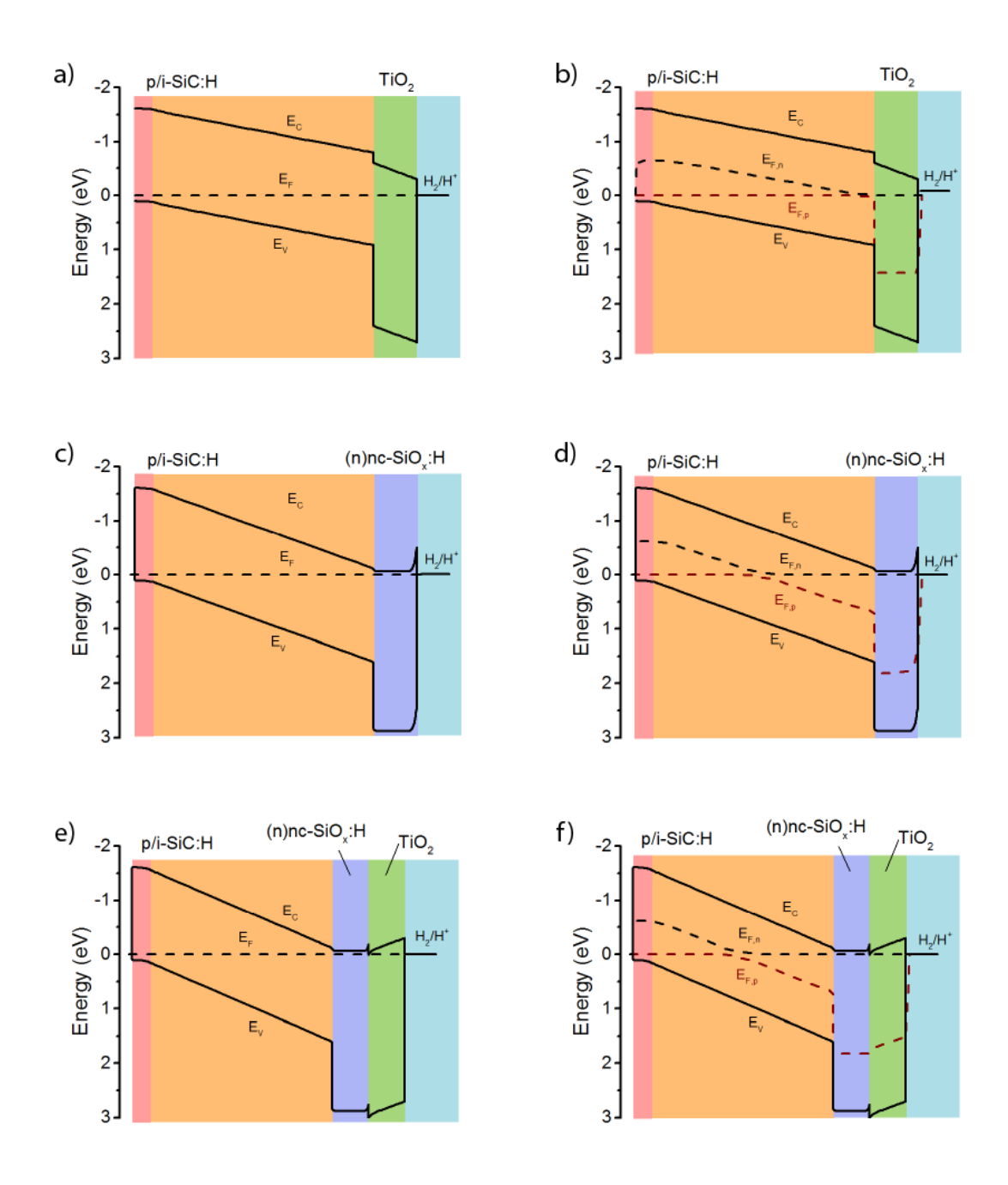


Figure 2.4: Simulations of the band alignment of the photoacthode with respect to the solution with a p/i/n junction including a,b) TiO_2 , c,d) $nc-SiO_x$:H and e,f)the combination of both in the dark (a,c,e) and illuminated under one sun (b,d,f)

a single arc. This means that a single process is dominating the response of the system, although there are different processes taking place, which are invisible for impedance spec-

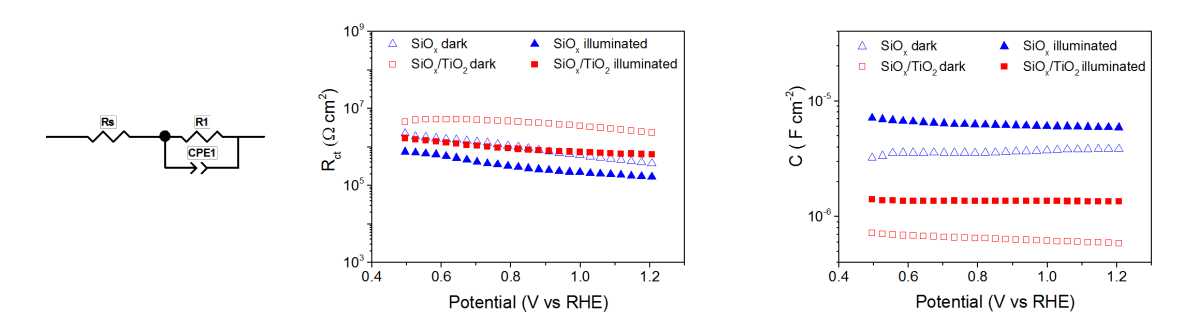


Figure 2.5: EIS analysis of a 100 nm (n)nc-SiO_x:H and a 100 nm (n)nc-SiO_x:H /20 nm TiO₂ film in dark conditions and under AM1.5 illumination (0.5M KHP pH4), together with the equivalent Randles'circuit. Note that these measurements have been done for positive potentials, and thus under reverse bias.

troscopy, probably because they appear at a time scale not sensitive for our experimental technique. We assigned the resistance to the charge transfer process, since it is extremely high to account for any other internal process in the multi-layered structure. Additionally, the constant evolution of the capacitance versus applied voltage is also an indication of a double layer dielectric capacitance, so it is reasonable to associate the elements of the Randles' circuit to the double layer capacitance and charge transfer resistance. The presence of a Warburg element in the equivalent circuit of Figure 2.6 accounts for the diffusion of electrolyte species. The resistance shows less variation between dark and illuminated conditions compared to the results in Figure 2.5 The inclusion of the TiO_2 layer in this case results in a lower resistance, probably due to the better band alignment and easier charge carrier injection. Regarding the capacitance, it increases with illumination in both cases, especially in the case of the sample with a TiO_2 layer. However, it must be noted that these capacitances have been reduced by at least one order of magnitude as compared to the individual layers, indicating the benefit of having a p/i/n structure for charge carrier transfer at the interface.

In summary, the introduction of a TiO_2 layer improves the band alignment of the photocathode. Regarding the introduction of a (n)nc- SiO_x :H layer between the absorber material and the TiO_2 , it seems to achieve a lower defect density, lower SRH recombination and higher charge carrier selectivity and internal electric field. By combining these two layers, a more efficient photocathode can be achieved.

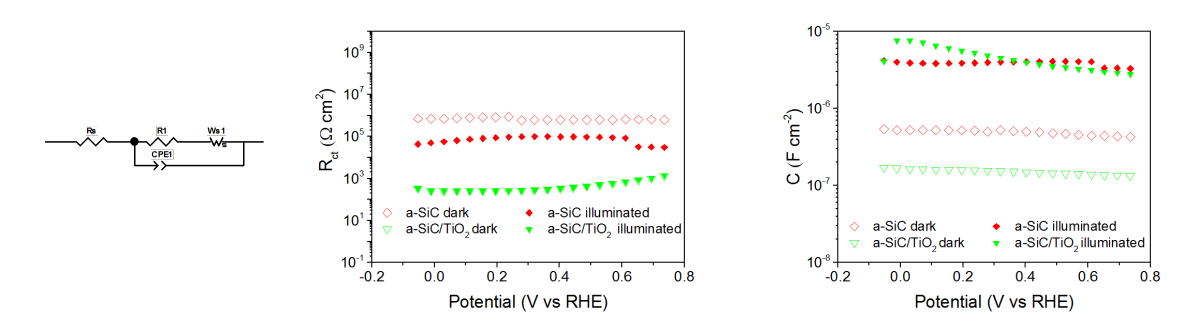


Figure 2.6: EIS analysis of a-SiC and a-SiC/TiO₂ samples in dark and under AM1.5 illumination conditions. (0.5M KHP pH4), together with the equivalent Randles' circuit including a Warburg element. Note that these measurements have been done for positive potentials, and thus under reverse bias.

Photocathode Optimization and Stability. In order to further study and optimize the effects of the improvement of charge carrier separation and collection in the semiconductor device, and the extraction of charge carriers at the semiconductor/electrolyte interface, the two considerations were decoupled. First, the semiconductor internal electric field and optical absorption were studied by isolating the semiconductor device as a PV solar cell, where the charge carrier extraction is assumed not to be the limiting factor (Figure 2.7 a, b). Second, to look at the effects of the catalyst and electrolyte, the electrochemical characteristics were measured (Figure 2.7c). The improvements in the internal electric field when introducing a (n)nc-SiO_x:H layer in the p/i structure were confirmed for different n-layer thicknesses, as can be seen in Figure 2.7 and Table 2.1. The n-layer thickness can change the optical performance of the photoelectrode, as well as affecting possible tunnelling effects through this layer. Moreover, if the layer is too thin, pinholes might appear creating short-circuit paths. When no n-layer is present, the open circuit voltage when measured as a solid-state PV junction is less than 0.4 V. When a layer as thin as 10 nm is introduced, the open circuit voltage and short circuit current are drastically improved, reaching almost the same values as thicker layers. However, the fill factor in this case is very poor, probably due to inhomogeneities in the layer thickness that may cause areas without n-layer within the cell and possible tunnelling effects. A thickness of 20 nm for the n-layer appears to be large enough for a good performance, reaching an open circuit voltage of 0.8 V and short circuit current density of more than 10 mA/cm², with a fill factor of almost 0.60. Further increase of the n-layer thickness leads to a slight increase in the fill factor and short circuit current that could be related to the optical properties of (n)nc-SiO_x:H, which enhance the back reflection.

[90, 92] Figure 2.7b shows that when no n-layer is included, a big fraction of the light with wavelengths higher than 450 nm is not absorbed. The introduction of an n-layer as thin as 10 nm highly improves this EQE. The optimum appears to be 30 nm, especially due to a higher current density. However, this improvement is not so apparent in the PEC measurements in Figure 2.7c), where the differences of the saturation current densities are within measurement error. This difference could be caused by the absence of Ag back reflector when measuring PEC JV characteristics. In addition, it seems that the (n)nc-SiO_x:H thickness is not the limiting factor of the photocathode performance, as long as it is present. This can be seen in the onset potential in Figure 2.7c), where virtually no difference can be seen. Finally, it is interesting to compare these onset-potentials (0.78-0.81 V) with the open circuit voltages of the solid-state measurements (0.81-0.83 V) when the thickness has reached the thickness of 20 nm. There seems to be a difference of around 20-30 mV between these two measurements, which can be related to the dependence of the overpotentials on the charge carrier injection into the electrolyte and the catalytic effects at the semiconductor/electrolyte interface.

Table 2.1: External parameters of the solid state JV characteristics with different n-layer thickness

n-layer thickness (nm)	$V_{OC}(V)$	$J_{SC}~(mA/cm^2)$	FF	Efficiency (%))
0	0.32	7.25	0.41	0.94
10	0.74	9.53	0.33	2.35
20	0.81	10.25	0.59	4.82
30	0.83	11.05	0.59	5.36
40	0.82	10.32	0.62	5.26

These results suggest that once the layer has reached the critical thickness of 20 nm, the properties cannot be improved much further by increasing the n-layer thickness. Moreover, the PEC characteristics of the 40 nm sample suggest that if the thickness of the n-layer is increased too much, the charge carriers might not be able to be easily injected into the electrolyte due to the additional resistances, hindering possible tunnelling of charge carriers.

When performing the light induced degradation experiments shown in Figure 2.8, an additional advantage of the (n)nc-SiO_x:H layer was found. The performance of the cells measured as solid-state devices degraded up to open circuit voltages of almost 0 V in 1000 h of exposure for the samples with thinner n-layer. On the other hand, samples with thicker n-layer have a

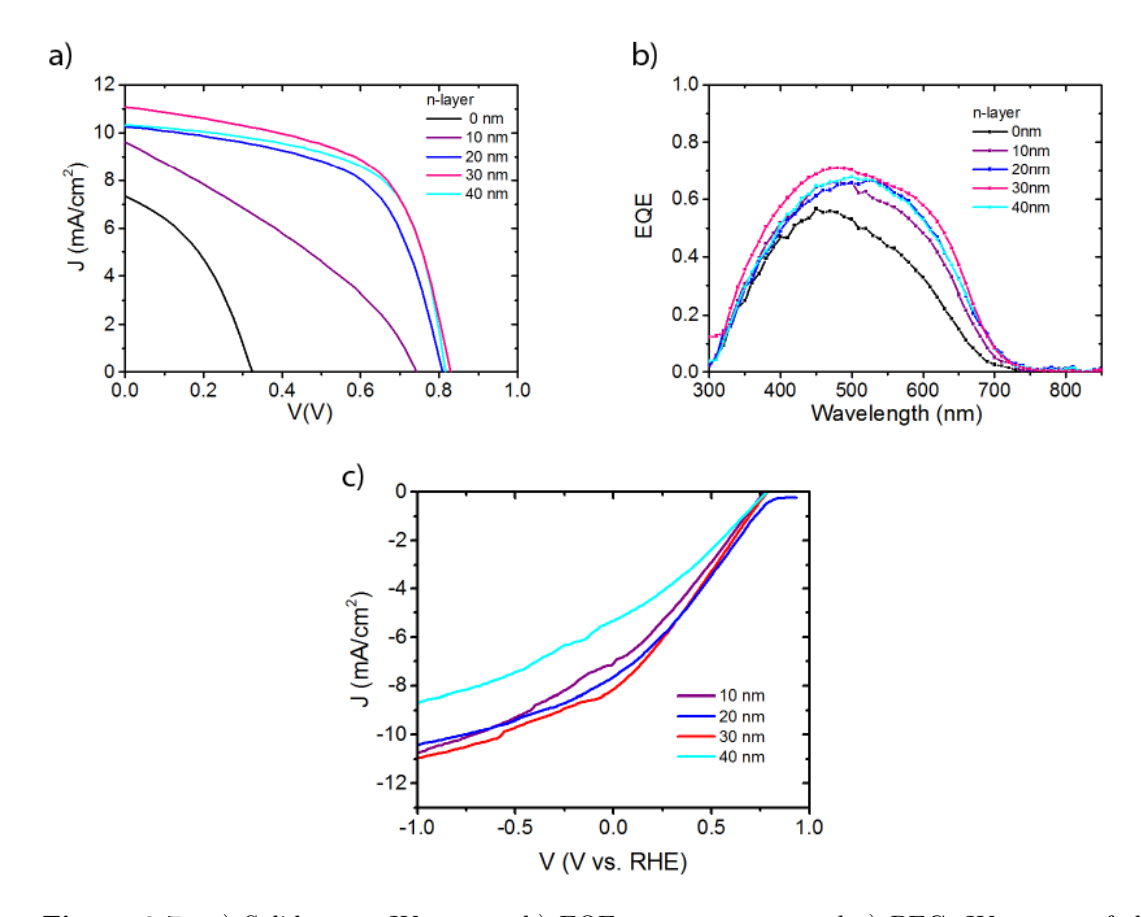


Figure 2.7: a) Solid state JV curves, b) EQE measurements and c) PEC JV curves of the a-SiC:H photocathodes at different n-layer thicknesses including a TiO₂ protective layer and a Pt catalyst.

 V_{OC} change in the order of 5 % in 1000 h with respect to the initial value. This suggests that the a-SiC:H absorber layer without an n-layer tends to degrade upon illumination. This could be explained by the mechanism of the Staebler-Wronski effect. [14] When charge carriers are generated in the absorber material but cannot be separated, they will recombine. Upon recombination, this energy is released within the absorber material, creating the metastable defects that cause light induced degradation. By introducing efficient means of separating the charge carriers and reducing recombination inside the absorber material, this effect can be reduced.

Thus, the introduction of an n-type $\operatorname{nc-SiO}_x$:H improves the optical and electrical characteristics of the photoelectrode, as well as enhancing its stability upon illumination at ambient conditions. Note that the results regarding 0 and 10 nm are not consistent with this trend.

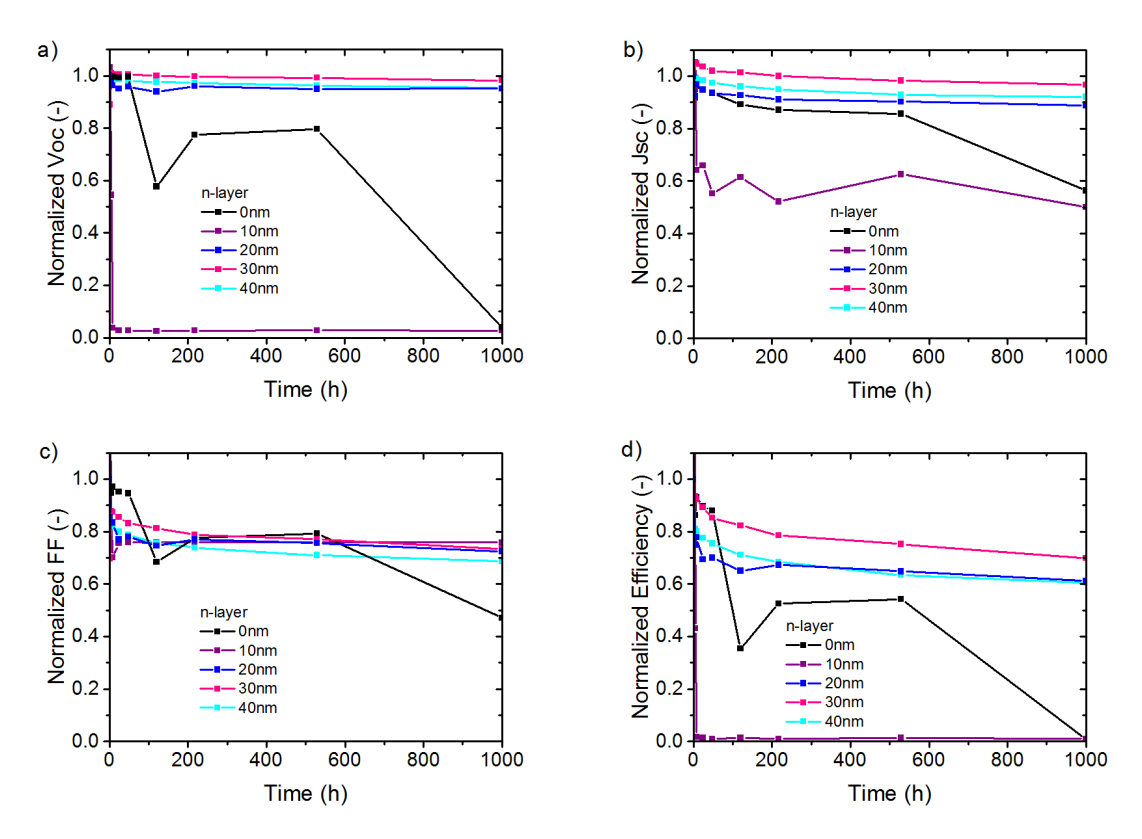


Figure 2.8: Light-induced degradation of the a) V_{OC} , b) J_{SC} , c) FF and d) Efficiency during 1000 h for varying n-layer thicknesses

This is due possible deposition and measurement irregularities. However, the lower performance with respect to the samples with 20 nm or over have consistently measured for shorter stretches of time. Since increasing the thickness of the n-layer further than 20 nm does not have a big effect on the optical or electrical properties of the photocathode, this thickness has been chosen as the standard for further studies.

To further improve the photocathode, also the light absorption in the absorber layer must be taken into account. Thus, to increase the light absorption in the p/i/n a-SiC:H photocathode, the i-layer thickness can be optimized. Figure 2.9 shows an increase in short circuit current density with thicker i-layer due to the higher light absorption. Figure 2.9a) indicates that if the i-layer thickness is as small as 50 nm, extra resistances and possible pinholes may appear, causing shunts and a very poor fill factor. For thicker layers this is not a problem anymore, since the i-layer is thick enough to maintain homogeneity. This effect is also reflected in the fill factor shown in Table 2.2. Regarding the optical effects, the photocathodes

with i-layers thicker than 150 nm show a saturation of the current density, display only a slight improvement in absorption in the red part of the spectrum (Figure 2.9b). However, the solid-state JV measurement shows a lower fill factor for 200 nm than for 150 nm. Thus, the additional absorption would be compensated by the enhanced recombination, creating a balance between the optical and electrical properties of the layer. It is also apparent from the EQE measurements in Figure 2.9b) that the EQE in the short wavelength region reduces with an increase of i-layer thickness. This can be explained by the reduced charge carrier collection at the p-layer, since the electric field is weakened.

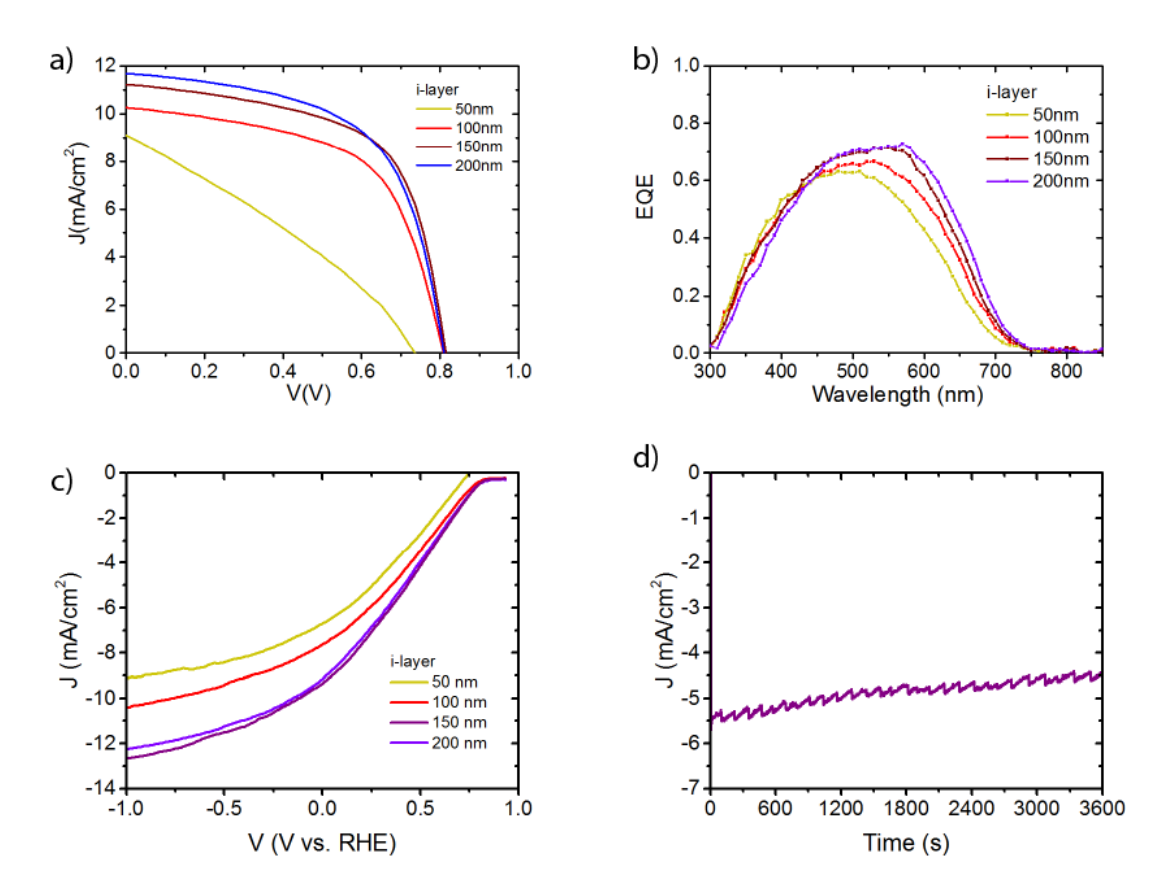


Figure 2.9: a) Solid state JV curves, b) EQE measurements and c) PEC JV curves of the a-SiC:H photocathodes at different i-layer thicknesses with a TiO₂ protective layer and Pt catalyst, and d) stability test for the 150 nm a-SiC:H photocathode with an applied voltage of 0 V vs. RHE

When looking at the PEC performance, the trend again seems to saturate at 150 nm. In this case, the series resistance for both 150 nm and 200 nm is the same, indicating that the series

Table 2.2: External parameters of the solid state JV characteristics with different i-layer thickness

i-layer thickness (nm)	$V_{OC}(V)$	$J_{SC} (mA/cm^2)$	FF	Efficiency (%)
50	0.74	9.02	0.32	2.09
100	0.81	10.25	0.59	4.82
150	0.82	11.21	0.60	5.58
200	0.81	11.68	0.59	5.57

resistance in the solution is probably the limiting factor. Since there is not much difference between 150 nm and 200 nm, 150 nm was chosen as the optimum layer thickness for this device as it will suffer less from light induced degradation. [14] Chronoamperometry measurements were performed on the p/i/n/TiO₂ photocathode with an i-layer thickness of 150 nm to determine its stability in the electrolyte, displayed in Figure 2.9d). This measurement shows that the photocathode can be reasonably stable for more than an hour, with a reduction of the photocurrent of less than 20%. When only considering the solid state degradation upon illumination, the photocathode with 20 nm n-layer showed a reduction in the short circuit current of about 10%. Thus, it could be assumed that about half of the stability loss is related to the Staebler-Wronski effect, while the other half would be caused by chemical degradation. Therefore, it seems that, at least in the first hour, the solid state stability and chemical stability are comparable.

2.4 Conclusions

This study demonstrates the importance of device design to enhance the separation and collection of charge carriers, and reduce the recombination losses, not only for PV but also for the PEC field. By introducing an n-doped nanocrystaline silicon oxide (nc-SiO_x:H) layer onto an amorphous silicon carbide (a-SiC:H) photocathode, its performance for solar water splitting can be improved. It can highly enhance the internal electric field and charge carrier selectivity of the photocathode, improving the charge carrier separation and collection. In addition, this layer also protects the photocathode of degradation upon illumination by reducing the SRH recombination. However, to improve the band alignment with the electrolyte, a TiO_2 layer is needed. The minimum thickness of the n-SiO $_x$:H layer was determined to be 20 nm. To enhance light absorption without affecting the charge collection performance, the

optimum absorber a-SiC:H layer thickness of this p/i/n photocathode was found to be 150 nm. Using these specifications, an onset potential of $0.8~\rm V$ vs RHE and a current density of $10~\rm mA/cm2$ at $0~\rm V$ vs. RHE can be achieved, with a loss in efficiency of only 20% after 1 h of operation.

2 Solar water splitting using a-SiC:H photocathodes

3

Designing a silicon based multijunction for water splitting

This chapter is partially based on the following publication:

P. Perez-Rodriguez, W. Vijselaar, J. Huskens, M. Stam, M. Falkenberg, M. Zeman, W. Smith, A.H.M. Smets. Designing a Hybrid Thin-film/Wafer Silicon Triple Photovoltaic Junction for Solar Water Splitting. *Under Review*.

3.1 Introduction

Due to the intermittent nature of solar energy sources, energy storage is a key factor for its implementation. Chemical fuels such as hydrogen, carbohydrates or ammonia are one of the most feasible options, since they are highly energetic fuels that can be easily stored for long periods of time. [27] Electrochemcial (EC) splitting of water offers a promising way to convert solar energy into hydrogen for long-term storage due to its low conversion losses. Hydrogen production requires a thermodynamic electrochemical voltage of 1.23 V. Added to this voltage, there are overpotentials caused by the charge carrier transport in the semiconductor and the electrolyte, catalytic effects and other losses of the systems. As a result, the total voltage needed to drive the reaction is in the range from 1.6 to 2.0 V. [93] In this case, multijunction devices are chosen as a reasonable alternative.

Multijunction devices are able to effectively use the solar spectrum while still providing enough voltage to drive the reaction in a PV-EC system. Solar-to-hydrogen (STH) efficiencies of 18.3 % have been demonstrated with concentrated light and a III-V/c-Si multijunction device. [94, 95] However, III-V materials are not economically feasible in large scale due to their scarcity and associated high cost. Thus, there is a need for earth-abundant devices that can efficiently split water, such as silicon. Thin-film (TF) silicon devices are widely known for their application in solar cells for electricity generation. [96, 97] They have also been previously tested for solar water splitting. Rocheleau et al. [98] report a 7.8 %STH efficiency using a triple junction amorphous silicon solar cell combined with a catalytic $Ni/NiFe_yO_x$ electrode, and Urbain et al. [99] achieved an STH efficiency of 9.5 % using a quadruple junction silicon solar cell. Nevertheless, thin-film cells have a limited potential regarding their light absorption. To overcome the light management limitations of purely thin-film devices while still being cost-effective, some hybrid approaches have been proposed. Monolithic perovskite/c-Si cells have previously reported efficiencies of 23.6 % as PV devices. [100] However, the crucial shortcomings of these structures are the relatively low stability and presence of lead in the structure. [101] As an alternative, this work proposes a novel multijuntion consisting of a hybrid device that combines wafer (W) and thin-film (TF) silicon technologies. In particular, an a-Si:H(TF)/nc-Si:H(TF)/c-Si(W) triple junction device is proposed for solar water splitting. This device has been already tested by Kirner et al. [102]

The proposed device in this work is predicted to provide high enough voltages for solar water splitting, with a considerable increase in current density with respect to purely thin film silicon solar cells due to better spectral utilization. However, there are certain challenges that need to be overcome, including the tunneling recombination junctions (TRJ), the growth of the absorber layers and the light management strategies to be applied. [103, 104] This chapter focuses on proving the device concept by analyzing the TRJs between the three subcells, which were deposited in a flat surface to better recognize the electrical effects. A TRJ junction is expected to increase recombination from both sides of the junction, to ensure current continuity. To achieve high tunneling in a TRJ, the band alignment should be such that the conduction band of the n-side has an energy close to the p-side valence band. TRJs play a crucial role on the performance of multijunctions solar cells, particularly affecting the open-circuit voltage and fill factor, which are two crucial factors for water splitting. The junction between the a-Si:H cell and the nc-Si:H cells has been previously studied in other works. [105–107] However, the junction between the nc-Si:H cell and the silicon heterojunction (SHJ) cell is relatively unexplored. [108, 109] Thus, by studying these different key aspects of the TRJ on the proposed multijunction cell, the voltage and fill factor can be improved, showing its potential for water splitting.

3.2 Materials and methods

The work presented here is divided in several steps, as presented in Figure 3.1. First, the single junctions were tested to determine the potential of this combination, which can also be suggested by the spectral irradiance characteristics of AM1.5 in Figure 3.1. The second step was to study the two different TRJs by depositing the top tandem and bottom tandem cells, depicted also in Figure 3.1. Finally, the triple junction was built following the optimized results of the two tandems and resulting TRJs. This section outlines the synthesis and characterization methods used to perform these experiments.

3.2.1 Synthesis methods

The device structure consists on a a-Si:H/nc-Si:H/c-Si triple junction, as shown in Figure 3.1, where the c-Si subcell has the structure of a SHJ cell. It was deposited on a flat c-Si Topsil n-type <111> FZ wafer of approximately 280 μ m, which was cleaned using a sequence of 99 % HNO₃ at room temperature for 10 min, 69.5 % HNO₃ at 100 °C for 10 min and 0.55 % HF at room temperature, with an intermediate step of de-ionized (DI) water after each acid step.

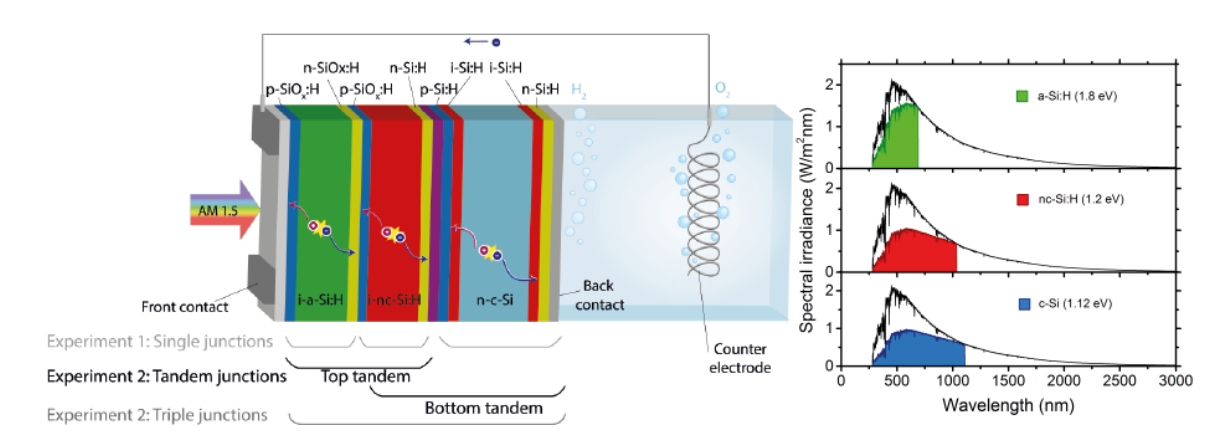


Figure 3.1: Schematic of the solar cell configuration when used for solar water splitting applications, including the different experiments performed; and the AM1.5 spectral utilization of the different subcells based on the bandgap of each material

Both the p-n structure of the SHJ and the p-i-n structure of the a-Si:H and nc-Si:H subcells were deposited using a plasma enhanced chemical vapor deposition (PECVD) multichamber system. Silane (SiH₄), hydrogen (H₂), carbon dioxide (CO₂), phosphine (PH₃) and diborane (B_2H_6) were used as precursor gases. The p- and n-layers of the p-i-n junctions are based on doped nanocrystalline silicon oxide ($nc-SiO_x:H$), nancocrystalline silicon (nc-Si:H) and amorphous silicon (a-Si:H). The highly doped layers used for the TRJs were deposited by increasing the phosphine flow by 50 % and the diborane flow by 100 % with respect to the standard flows. These flows were optimized to maximize the cell performance and minimize the internal stress at the nc-Si:H absorber material, which might cause detachment of the thin film cell from the crystalline silicon wafer. Sputtering was used to deposit the transparent conductive oxides (TCO), both indium-doped tin oxide (ITO) and hydrogenated indium oxide (IOH). In particular, ITO was deposited as a graded layer to minimize the damage caused by ion bombardment, starting at conditions of 60 °C and 40 W, and increasing it to 110 °C and 100 W. The IOH was deposited at room temperature with a power of 135 W and 30 ubar of H₂O partial pressure, and then annealed at 175 °C for 150 min. The contacts were deposited via physical vapour deposition (PVD). The front contact consists of a grid of 500 nm Al. The back contact, which also acts as a back reflector, is formed of 200 nm Ag, 30 nm Cr and 500 nm Al, and covers the complete back side. The cell area used was 1 cm². The cells have been deposited in an n-i-p configuration, but are illuminated in a p-i-n sequence.

3.2.2 Characterization methods

The external quantum efficiency (EQE), defined as the percentage of photons reaching the device surface that generate free charge carriers, was measured to further understand the current matching between the three subcells. An in-house EQE setup in TU Delft was used, consisting of a Xe lamp and a monochromator to define the wavelength range. To measure the three subcells separately, bias light was provided to saturate the other cells. The top cell was saturated using light with wavelengths between 365 and 448 nm, the middle cell was saturated using light between 470 and 530 nm, and the bottom cell was saturated with light between 655 and 950 nm. The JV measurements for the solar cell were obtained from a Wacom AAA solar simulator using two lamps (Xe and halogen), and an AM 1.5 filter. The current density was normalized with the short circuit current obtained from the weighted integration of the cell EQE measurement with the AM1.5 spectrum. The reflectance of the solar cells was measured using a Perkin Elmer Lambda 950 UV/Vis apparatus with an integrating sphere (IS). The reflectance was measured for the solar cell active area, therefore excluding the reflectance of the metal grid. In addition, the characterization of the TRJ has been done by depositing the doped layers of the TRJ on textured Asahi UV glass covered by a fluor doped tin oxide (FTO) as TCO. Then, the EQE and dark JV characteristics were measured at different temperatures.

3.3 Results and discussion

In order to assess the viability of this configuration, the three separate single junctions were fabricated, with the external parameters shown in Table 3.1. Looking at the voltages obtained, the total sum of the individual open circuit voltages is equal to 2.07 V, which is promising for an integrated triple junction for solar water splitting. In addition, it is also important to realize the moderate fill factor of 0.61 for the nc-Si:H, a good result considering that the nc-Si:H was deposited on a flat surface.Based on these cells, multijunctions were fabricated. However, even though the final aim is to produce a triple junction cell, the top (a-Si:H/nc-Si:H) and bottom (nc-Si:H/c-Si) tandems have been studied separately to better isolate the effects of each junction, as shown in Figure 3.1. Finally, these tandems were combined in a triple junction cell.

The junction between the a-Si:H and nc-Si:H subcells has been widely studied for the micromorph cell, [20, 110] and the concept of intermediate reflectors such as a combination of n-a-Si:H and $n-nc-SiO_x:H$ layers has been shown to improve the optical and electrical properties of the tandem cell. [111, 112] Thus, in this work, a combination of 6 nm n-nc-SiO_x:H/ 10 nm n-a-Si:H was used as opposed to a simple $n-SiO_x$:H layer. The small thickness of these layers also ensures the transmission of light to the bottom cell without significant parasitic absorption. Figure 3.2 shows the characteristics of the micromorph cell with and without an intermediate reflector. The intermediate reflector composed of a n-layer combination reaches an open-circuit voltage (V_{OC}) of 1.28 V, a fill factor (FF) of 0.57 and a short-circuit current (J_{SC}) of 7.83 mA/cm², as summarized in Table 3.1, which represents an improvement of all parameters with respect to the single n-nc-SiO_x:H layer. One of the effects that can be seen is the better utilization of the blue light in the top cell, due to the intermediate reflector. Moreover, looking at the single junction cells, the addition of the a-Si:H and nc-Si:H open circuit voltages is 1.38 V, showing that the actual open circuit voltage achieved is only 0.09 V lower than the maximum potential voltage that could be achieved based on these single junctions. Finally, the fill factor is also improved, probably due to the improved functionality of the TRJ, and showing that the thickness used for the n-layer is enough to maintain the electric field for charge carrier separation and collection. This is also seen in the open-circuit voltage, where there is an improvement of 20 mV between the reference and n-bilayer samples, 1-2 mV of which this is due to the increased short circuit current.

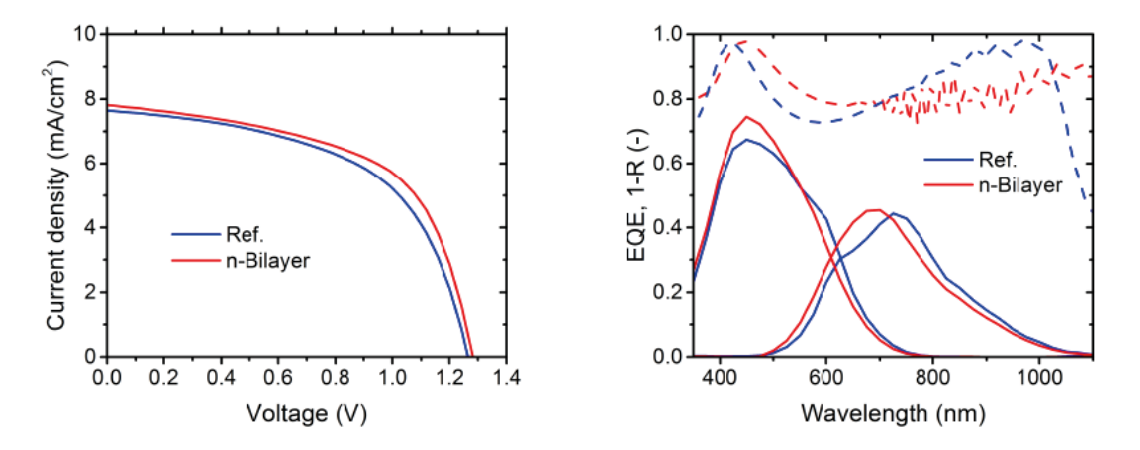
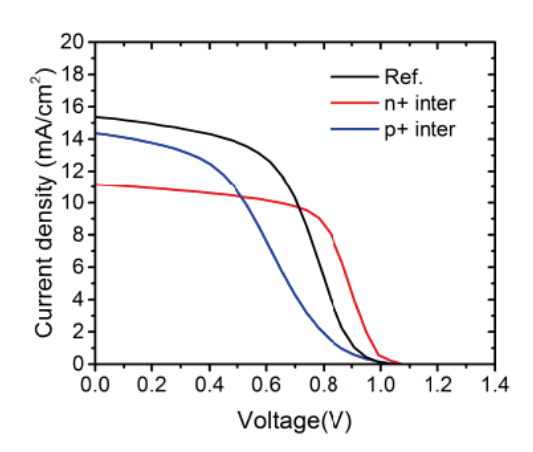


Figure 3.2: JV and EQE characteristics of the top tandem deposited on flat substrates with different recombination junctions, where Ref. represents a simple 40 nm n-nc-SiO_x:H and n-Bilayer represents a combination of 6 nm n-nc-SiO_x:H and 10 nm a-Si:H, which act as an intermediate reflector



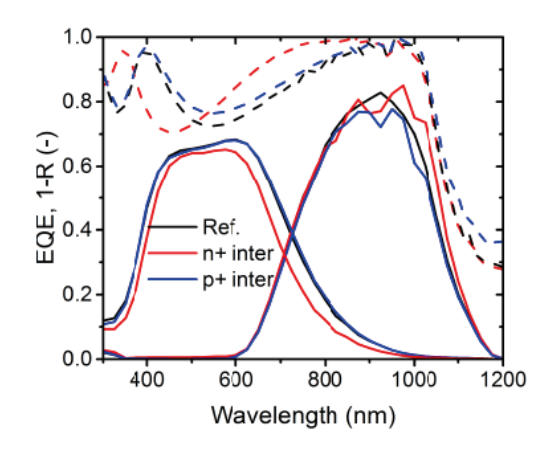


Figure 3.3: JV characteristics and EQE measurements of the bottom tandem deposited on flat substrates with different TRJ intermediate layers

The bottom TRJ is the most crucial and innovative junction of this device, since it combines the difficulties of c-Si wafer passivation and the growth of nc-Si:H on flat surfaces, on top of all the other traditional challenges of TRJs. Two main approaches were used to create an effective TRJ. In the first approach, an additional layer was added to act as TRJ, either a highly n- or p-doped a-Si:H layer. This higher doping was achieved by increasing the flow of doping gas during PECVD processing. This case is depicted in Figure 3.3, showing that the TRJ based on a highly doped a-Si:H intermediate does not improve the overall performance. This is confirmed when looking at the external parameters in Table 3.1. It is important to notice that all the JV characteristics show an S-shape, which indicates the presence of energy barriers inhibiting charge carrier transport. In particular, the solar cell with a p⁺ intermediate shows a very poor FF and strong S-shape behaviour, suggesting the presence of a high electrical barrier. In the case on the n⁺ intermediate, the effect of this TRJ on the performance of the tandem cell is an improved FF and open-circuit voltage, but a reduced short-circuit current. These parameters suggest better selectivity at the desired interface, but a negative optical effect. However, it is also possible that the improved fill factor is partly due the bigger current mismatch.

In order to further explain the effect of these junctions, a more detailed study was conducted following [108]. The isolated TRJ stacks, including all p- and n-layers, have been deposited on UV Asahi glass and tested in terms of their optical and electrical behaviour. By measuring the EQE and dark JV curves of these junctions, the possible losses and recombination

Table 3.1: External parameters of the different solar cells used in the different experiments, namely single, double and triple junction

		V_{OC}	J_{SC} top	J_{SC} middle	J_{SC} bottom	J_{SC} total	FF	Eff.
		(\)	(mA/cm^2)	(mA/cm^2)	(mA/cm^2)	(mA/cm^2)	-	(%)
Single	a-Si:H	0.87	7.6	1	ı	1	99.0	4.4
junction	nc-Si:H	0.51	ı	17.7	ı	ı	0.61	5.5
	SHJ	69.0	ı	1	30.7	ı	0.64	13.6
Top	$n-SiO_x$:H 40 nm	1.26	9.1	7.7	1	16.8	0.55	5.3
tandem	$\text{n-SiO}_x \text{:H/a-Si:H}$	1.28	11.0	7.8	ı	18.8	0.57	5.7
Bottom	Bottom Ref (no intermediate)	1.03	1	15.4	15.1	30.5	0.48	9.7
tandem	n ⁺ a-Si:H inter.	1.08	1	11.1	15.8	26.9	0.59	7.1
	p ⁺ a-Si:H inter.	1.00	ı	15.5	14.3	29.8	0.38	5.37
	-u	1.20	ı	14.8	17.8	32.6	0.54	89.6
	+d	1.12	ı	15.8	20.4	36.2	0.49	9.13
Triple	$ITO/(p)nc-SiO_x$:H	1.98	8.7	7.1	16.7	32.5	0.62	8.71
junction	IOH/(p)nc-SiO _x :H	1.88	9.5	8.3	17.0	34.8	0.64	86.6
	IOH/p-Bilayer	2.03	6.6	8.1	16.7	34.7	0.64	10.42

mechanisms can be identified. Finally, the dependence of the JV curve on temperature can help to elucidate the tunnelling mechanism present in the device. When looking at the TRJ performance, it must be taken into account that it should not present a rectifying diode behaviour so that no reverse bias is triggered during illumination.

The results shown in Figure 3.4 suggest that by including a highly doped region, the rectifying diode behaviour is enhanced rather than suppressed, which could partially explain the lower performance of these junctions. Figure 3.4a) shows the EQE of the different TRJs. In general, the lower the EQE, the less it acts as a rectifying diode and the better the TRJ operates. Based on this assumption, these intermediate layers increase the EQE response, meaning that upon illumination this junction would create a reverse bias. This could explain the relatively low open-circuit voltages achieved by the tandem solar cells (1.08 V), especially when comparing them on the sum of the single junctions (1.20 V). Looking at the electrical performance shown in Figure 3.4b) and c), the p⁺ intermediate shows higher series resistance, probably caused by the high density of defects that boron creates within the lattice. This could partly explain the poor FF of this cell shown in Figure 3.1 and Table 3.1. Another interesting factor to consider is the maxima of the function $\partial (lnI)/\partial V$ depicted on Figure 3.4b), where the p⁺ intermediate shows a local maximum at around 0.6 V, [108] suggesting that there are several transport mechanism playing a role on these TRJs. To elucidate the transport mechanisms present, the temperature effects were measured as presented in Figure 3.4d). The reference sample, with no intermediates, shows the least current dependence with temperature, suggesting a temperature-independent transport mechanism such as tunneling. [108] On the other hand, n⁺ intermediate samples show a rather high dependence on the temperature, which suggests that in these junctions, thermionic emission might play a bigger role during the tunnelling effect. [113]

This analysis thus suggests that both including an n⁺ or a p⁺ intermediate causes an undesired rectifying diode behaviour. Therefore, a different approach was taken, consisting of highly doped n- and p-layers on the subcells, without an intermediate layer to act as TRJ. Figure 3.5 shows the effects of including a higher p and n-doped layers next to the junction. Both for the case of higher dopant concentration in the p- and n-layers, the performance of the tandem solar cell is improved in terms of open-circuit voltage and fill factor, as shown in Table 3.1 and Figure 3.5. It must be noted that the highly doped p-layer cell also includes a thicker (i)a-Si:H passivating layer for the SHJ subcell in order to avoid the boron atom

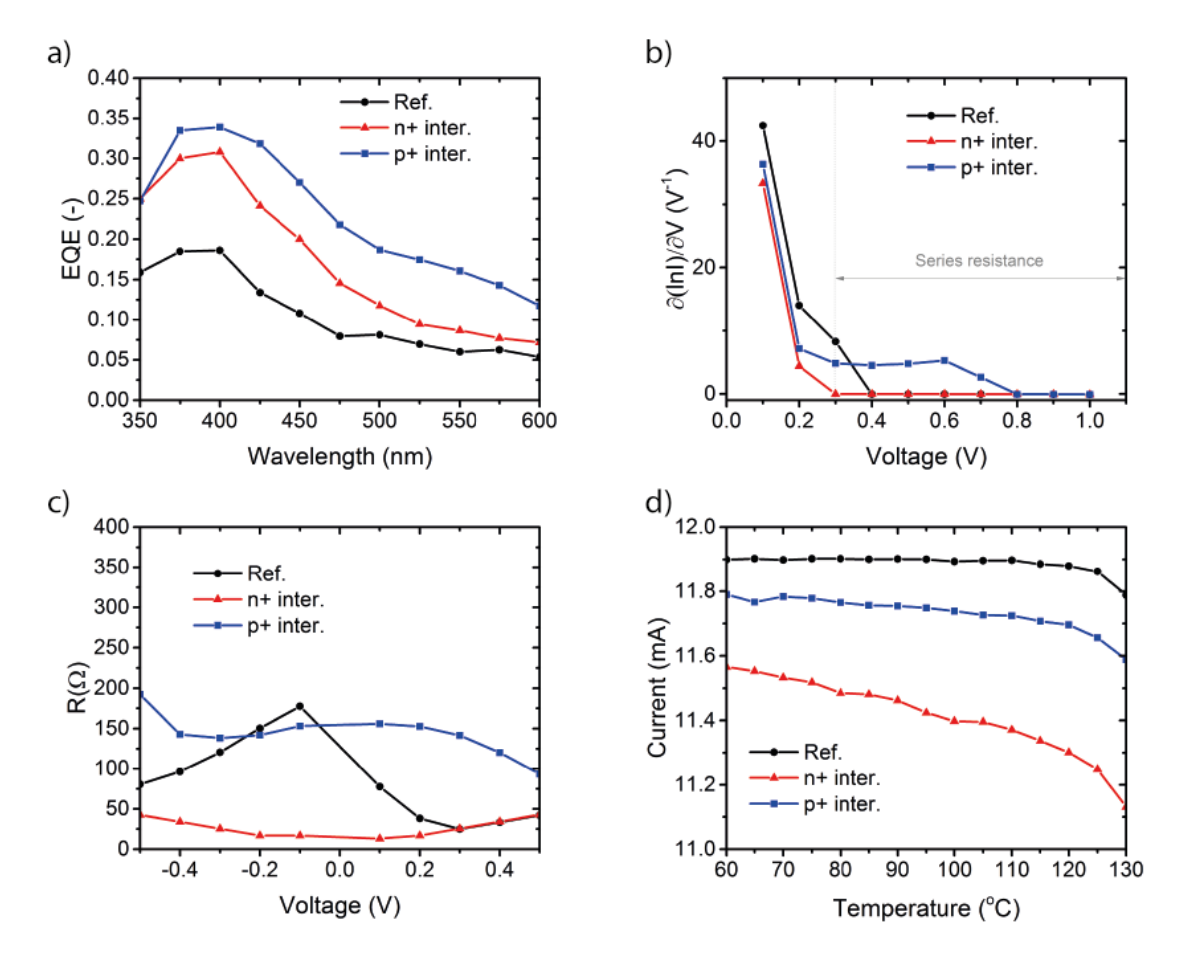


Figure 3.4: Tunnel recombination junction study for the bottom tandem when including an intermediate layer deposited on an Asahi UV substrate. a) EQE, , b) $\partial(lnI)/\partial V$ with respect to the voltage applied, c) resistance in dark conditions at different voltages, and d) dark current dependence on temperature.

migration to the c-Si surface and the subsequent loss in c-Si passivation. [109] This strategy does improve the V_{OC} , but lowers the fill factor, indicating the introduction of high series resistance in the cell due to the thicker a-Si:H layer. The best results were obtained using a higher doping in the n-layer of the nc-Si:H subcell, which does not introduce any further resistances in the system and increases the tunneling at the TRJ interface. This can also be seen when comparing the open circuit voltage of this cell (1.20 V) to the maximum potential based on the single junction cells (1.20 V), confirming a negligible loss of voltage. However, it can be seen in the EQE characteristic that when using a higher doping in the n-layer, the optical response of the top cell also varies, showing lower EQE values on the blue part of the spectrum. This might be caused by a difference in reflection at the cell front surface due

to instabilities and lack of reproducibility within the ITO deposition. In any case, since the highly doped n-layer samples show the best FF and open circuit voltages without a major detrimental effect on the short-circuit current, it is assumed to be the best choice for this TRJ, and thus it would be used further in the triple junction configuration.

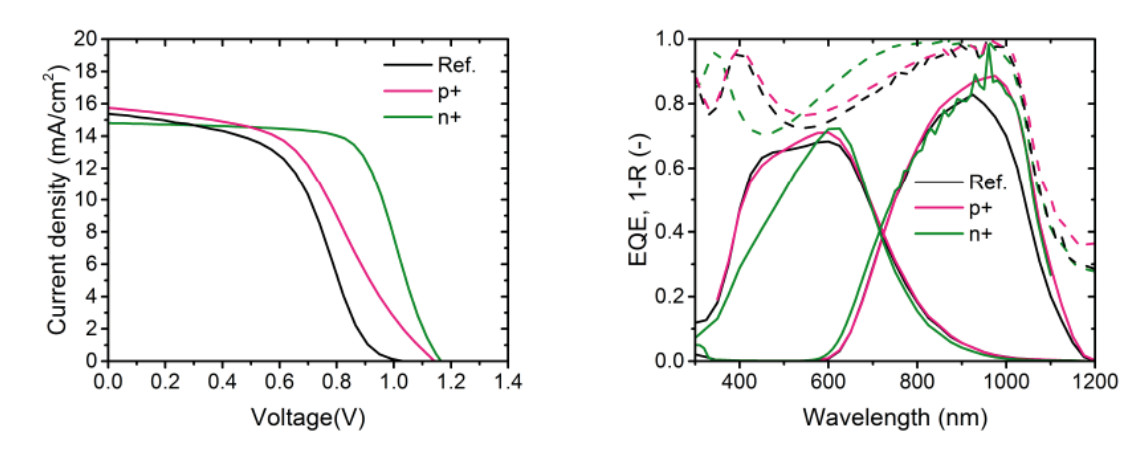


Figure 3.5: JV characteristics and EQE measurements of the bottom tandem deposited on flat substrates, with different doping at the TRJ interface

Using the TRJs developed and an ITO layer as front TCO, a triple junction was fabricated, achieving an open-circuit voltage of 1.98 V, a FF of 0.62, a current density of 7.13 mA/cm² and a final efficiency of 8.71 %, as shown in Figure 3.6 and Table 3.1. To further improve the efficiency of the triple junction cell, the limiting parameters must be identified. Since the open-circuit voltage and fill factor achieved are relatively close to the theoretically possible values based on the single junction cells, other strategies must be considered. An important factor when improving this cell is the light management, and in this case it must be focused on the current limiting middle subcell. For practical reasons, the thickness of the nc-Si:H subcell was limited to 3.5 μ m. Thus, other strategies were used to improve the optical performance of the middle subcell. A factor that can be improved is the front TCO, which is responsible for a large amount of reflection at the cell surface, as seen in the 1-R depicted in Figure 3.6, especially in the wavelength range between 400 and 700 nm. Therefore, ITO was replaced by the more transparent and conductive IOH, which would avoid high reflection in the region between 500 and 900 nm, and thus would allow for more light to reach the middle cell. By using IOH, an open-circuit voltage of 1.88 V was achieved, with a FF

of 0.64, a current density of 8.28 mA/cm² and a final efficiency of 9.98 % as shown in Table 3.1.

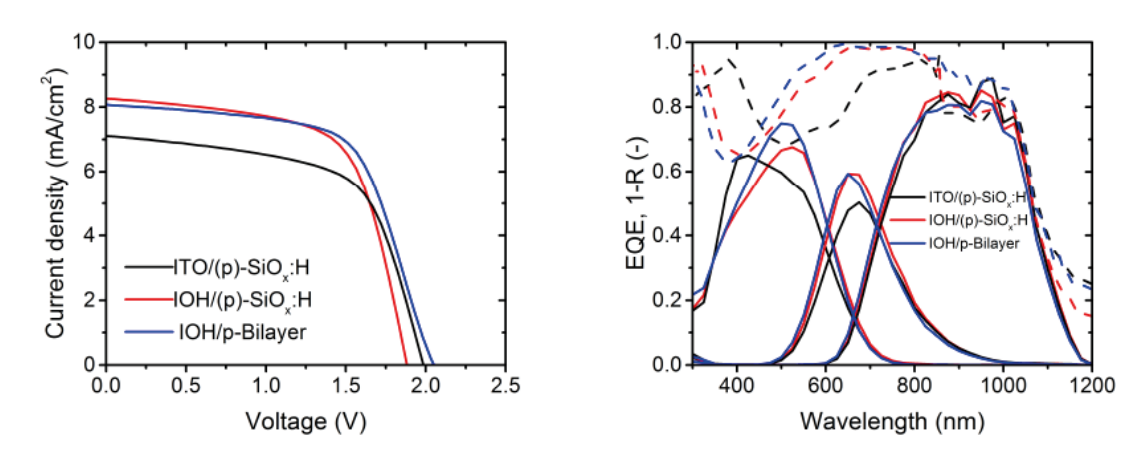


Figure 3.6: JV characteristic and EQE measurements of the triple junction cells deposited on flat substrates with different TCOs and different top p-layer in contact with the TCO, where the p-Bilayer refers to a combination of p-nc-SiO_x:H (8 nm) and p-nc-Si:H (4 nm).

Finally, since the IOH layer improved the light management but decreased the open circuit voltage, the contact between the front p-layer and the TCO needs to be further studied. A p-doped nanocrystalline silicon thin layer is placed on the front of the cell, followed by a H₂ treatment to passivate any dangling bonds. This strategy has the potential to lower the energy barrier at the interface between p-layer and TCO [114], because nc-Si:H materials are able to achieve a lower activation energy (51.3 meV) than the p-SiO_x:H material previously used (240.9 meV). The open circuit voltage achieved by this configuration is 2.03 V, with a fill factor of 0.64 and a higher efficiency of 10.47 %. Interestingly, looking at the EQE measurements in Figure 3.6, it seems that there is also a slight improvement in the optical performance of the top cell, while the EQE of the other two subcells slightly decreases. Even though this increase on the top subcell EQE does not affect the overall performance of the cell, since they are limited by the middle subcell, this change is interesting. There might be both optical and electrical effects by this change in p-layer. Introducing a p-bilayer with different refractive indexes can reduce the reflection at the front of the cell, increasing the overall performance of the cell. Most importantly, the electrical properties are improved by facilitating the charge carrier injection from the solar cell into the TCO, suggesting that a IOH/p-bilayer configuration is beneficial to fabricate an efficient triple junction cell.

When comparing the achieved results to the potential of this triple junction based on the single junction performance, there are several conclusions to be made. First, regarding the open-circuit voltage, there are minimal losses considering the sum of the open-circuit voltages produced by the single junction cells (2.07 V) compared to the open-circuit voltage of the triple junction solar cell (2.03 V). The fill factor of 0.64 is also comparable to that of the single junction cells (Table 3.1), suggesting that the tunnelling recombination junctions are not the main loss mechanism of this cell. Secondly, looking at the currents produced, the short-circuit current densities of the different subcells are highly mismatched, with the middle cell being the limiting factor. If the subcell short-circuit current densities are added to calculate the spectral utilization, it results on 34.61 mA/cm², which is only about 4 mA/cm² more than what the SHJ single junction produces. This suggests that further light management techniques are needed to achieve current matching and higher spectral utilization. By realizing such a current matched cell, high STH efficiencies can be realized. Finally, although current mismatches could occur in this cell due to a variable solar spectrum, the operational point of the PV-EC device can still be unchanged due to the resulting higher fill factor of mismatched cells.

3.4 Conclusions

We proposed a triple junction heterostructure consisting of a-Si:H(TF)/nc-Si:H(TF)/c-Si(W) in order to achieve the desired voltages for solar water splitting, which is considered to be between 1.6 and 2 V. The development and study of the tunneling recombination junctions (TRJ) is an crucial component to optimize the performance of this structure. The optimum top TRJ considered was based on 6 nm of n-nc-SiO_x:H and 10 nm n-nc-Si:H, while the bottom TRJ is enhanced by increasing the doping on the n-layer. This allows for efficient charge carrier separation within the cell, while enhancing the recombination at the interface between each subcell. Finally, the performance can be improved by using IOH as TCO and a combination of p-nc-Si:H and p-nc-SiO_x:H at the front surface to improve the electric contact of the cell to the TCO. The final device was able to achieve an open-circuit voltage (V_{OC}) of 2.03 V, a fill factor (FF) of 0.64, a short-circuit current density (J_{SC}) of 8.07 mA/cm² and an efficiency of 10.42 %. These high voltage and fill factor are a promising step towards fully autonomous water-splitting devices based on earth-abundant materials that can facilitate long-term solar energy storage. Based on the loss analysis, further optimizations should focus on light management techniques to achieve current matching.

3 Designing a silicon based multijunction for water splitting

4

Light management of a hybrid silicon cell for water splitting

This chapter is partially based on the following publication:

P. Perez-Rodriguez, W. Vijselaar, J. Huskens, M. Stam, M. Falkenberg, M. Zeman, W. Smith, A.H.M. Smets. Designing a Hybrid Thin-film/Wafer Silicon Triple Photovoltaic Junction for Solar Water Splitting. *Under review*.

4.1 Introduction

The urgency for renewable energies to substitute fossil fuels is increasing. Among the possibilities, solar energy seems one of the most promising ones. [1] However, the availability of solar energy is intrinsically intermittent, both in the long and short term. Tackling this challenge is especially important to be able to integrate solar energy at a large scale into the electricity grid. Solar fuels are a promising option to address this problem, especially regarding the long-term energy storage. [27] In particular, direct solar-to-hydrogen (STH) routes offer a promising way to produce hydrogen by using solar energy.

In order to produce hydrogen based on direct solar light conversion, a solar device needs to comply with certain design parameters for highly efficient conversion. The electrochemical (EC) reaction of water splitting requires a thermodynamic potential of 1.23 V. However, due to losses and overpotentials in the solar cell, cabling, catalysts and electrolyte among others, the practical potential needed for efficient water splitting would be between 1.6 and 2 V. [93] In order to achieve this voltage with a direct solar device, several solar cells in series are needed. This has been demonstrated among others, by Schuttauf et al. [48], who connected three silicon heterojunction (SHJ) cells in series to an electrolyser, achieving a STH efficiency of 14.2 %. Moreover, in order to optimize the solar spectrum utilization, a stacked configuration could be used. Licht et al. [115] used this approach with an AlGaAs/Si cell with a STH efficiency of 18.3 %. However, these type of cells are based on rare elements, limiting their cost and feasibility. Using a more commercially feasible approach, Urbain et al. [99] demonstrated a quadruple cell based on amorphous silicon (a-Si:H) and nanocrystalline silicon (nc-Si:H) achieving an efficiency of 9.5 %. Nevertheless, the use of materials with similar bandgaps limits the spectral utilization of these cells. In order to further improve direct solar water splitting devices based on earth-abundant materials with good spectral utilization, a new configuration was proposed, namely a hybrid thin-film/wafer solar cell consisting of an a-Si:H/nc-Si:H/c-Si solar cell. This has already been demonstrated in the previous chapter, as well as in literature. [102]

Previous studies have focused on the novel tunneling recombination junction between the nc-Si:H thin film cell and the SHJ c-Si cell, demonstrating a cell with an open circuit voltage of 2.03 V and a fill factor of 0.64. [109] Nevertheless, there are still some issues associated with this cell, especially related to the photocurrent density produced. In order to improve this

current density, light management techniques need to be implemented. However, many of these light trapping techniques tend to negatively affect the electrical and material properties of the cell. Therefore, a trade-off is established between optical and electrical performance. The aim of this work is to establish a balance between these two parameters in order to achieve high STH efficiencies. First, texturing of the crystalline silicon substrate was studied to increase the light absorption within the cell, exploring its light trapping capabilities, and the adhesion, crystallinity and material quality of the nc-Si:H absorber layer. Second, it must be consider that this cells tend to be limited by the middle cell, partly due to the overlapping absorption between the top and middle cell. Thus, this work explores the use of a different absorber, optimizing the current matching of the cells. With the optimization of these two parameters, it is expected that the final cell would be able to efficiently split water as a stand-alone device. This will be tested by directly connecting this cell to a Pt/IrO_x electrolyzer.

4.2 Materials and Methods

4.2.1 Synthesis Method

The device structure consists on an a-Si:H/nc-Si:H/c-Si triple junction, as shown in Figure 4.1. The c-Si wafers used were Topsil n <111> FZ wafers of 280 μ m, cleaned by sequential 99 % HNO₃ at room temperature, 69.5 % HNO₃ at 100 °C and 0.55 % HF at room temperature. When textured, the pyramids on the wafers were created by a TMAH solution of 5 % for 35 min at 75 °C and 100 rpm. The p-i-n structures of the solar cell were deposited using a Plasma Enhanced Chemical Vapor Deposition (PECVD) multichamber system. Silane (SiH₄), hydrogen (H₂), carbon dioxide (CO₂), phosphine (PH₃) and borane (B₂H₆) were used as precursor gases. The transparent conductive oxide (TCO), namely hydrogenated indium oxide (IOH) was deposited by sputtering at room temperature, and further crystallize by an annealing step at 175 °C for more than 2 hours. The contacts were deposited via PVD evaporation. The front contact consists of 500 nm Al. The back contact, which also acts as a back reflector, is formed of 200 nm Ag, 30 nm Cr and 500 nm Al. The cell area used was 1 cm².

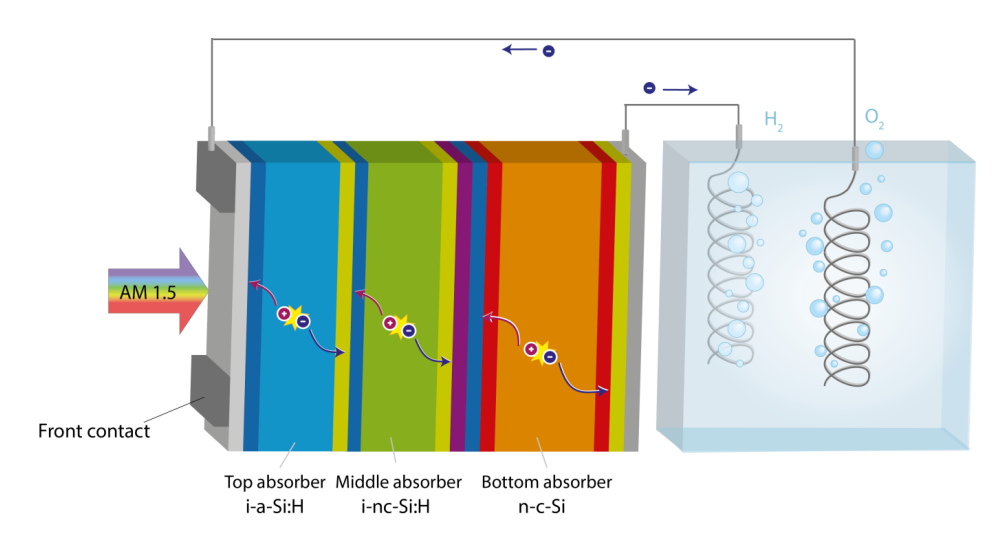


Figure 4.1: Schematic of the solar cell configuration when used for solar water splitting applications

4.2.2 Characterization Method

The crystallinity was measured using Raman spectroscopy, and the different peaks were fitted to a number of Gaussian disributions following the method proposed in [116]. The setup used was a Renishaw InVia apparatus, employing a 25 mW Ar laser as excitation source with a wavelength of 514 nm and focused on a spot of approximately 1 μ m. A Hitachi S4800 system was used to capture the scanning electron microscope (SEM) images of the surface and profile. The samples used were approximately 3 μ m thick.

The external quantum efficiency (EQE) was measured to further understand the effect of the various absorber bandgaps on the current matching of the three subcells of the multijunction cell. To measure the three cells separately, bias light was provided. An in-house EQE setup in TU Delft was used, consisting of a Xe lamp and a monochromator to define the wavelength range. To measure the three subcells separately, bias light was provided to saturate the other cells. The JV solid state measurements of the solar cell were obtained from a Wacom AAA solar simulator. The current density was normalized using the short circuit current obtained from the integration of the current-limiting cell EQE weighted by the AM1.5 spectrum. The reflectance of the solar cells was measured on the active area using a Perkin Elmer Lambda 950 UV/Vis apparatus with an integrating sphere (IS).

The optimized multijunction solar cell was combined with al electrolyzer based on an IrO_x

anode and a Pt cathode. Both electrodes were fabricated by depositing Pt and Ir using an in-house built sputtering setup in TU Twente. Subsequently, the electrochemical growth of IrO_x from Ir was carried out in a 0.5 M H_2SO_4 solution with a Versastat 4 potentiostat. The electrolyzer was tested using a potentiostat (VersaSTAT 4) in a two-electrode configuration, where the cathode with an exposed projected surface area of 3.14 cm² acted as the working electrode (WE), and the anode was the counter electrode (CE). The electrolyte used was 0.5 M aqueous sulfuric acid (H_2SO_4). The light source used was a 300 W xenon arc light source, fitted with Air Mass filter (AM 1.5 G) from Newport, Oriel Instruments. Before every measurement the lamp was checked by a calibrated reference solar cell (91150V).

4.3 Results and Discussion

Previously, a triple junction solar cell based on a-Si:H/nc-Si:H/c-Si structure was explored, focusing on the importance of the tunnelling recombination junctions. However, the absorber materials also play an important role in the optimization of this triple junction cell, especially regarding the photocurrent densities that can be achieved. One of the most challenging aspects of building this multijunction cell is the growth of the nc-Si:H subcell. This material does not grow well on flat surfaces, due to internal stresses leading to cracks and poor adhesion to the substrate. [103, 104] To overcome this barrier, two approaches were taken: to texture the substrate [104] or to vary the silane ratio during deposition, which would affect the crystallinity of the absorber. [117] First, the silane flow in the PECVD chamber was varied from 3.4 to 3.6 sccm in both a flat and textured crystalline wafer, while maintaining the H₂ flow constant at 120 sccm. This range was chosen as since previous work determined it to be the optimum region for nc-Si:H growth. [118] The crystallinity was then measured using Raman spectroscopy and following ref. [116], and it is shown in Figure 4.2. Note that this crystallinity refers to the top part of the bulk of the material, and it might vary at the interface with the crystalline silicon substrate. [118] These results show that the crystalline fraction depends on the silane ratio, but the substrate texture does not have a big impact on the crystallinity of the sample. Therefore, it will be assumed that the optimum crystallinity will be the same in both cases.

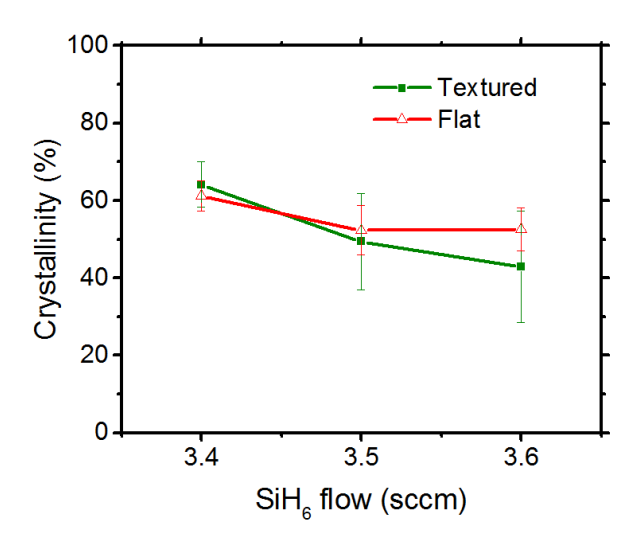


Figure 4.2: Crystalline fraction of nc-Si:H films depending on the silane (SiH₆) flow and the substrate conditions. Note that the H_2 flow during deposition is 120 sccm

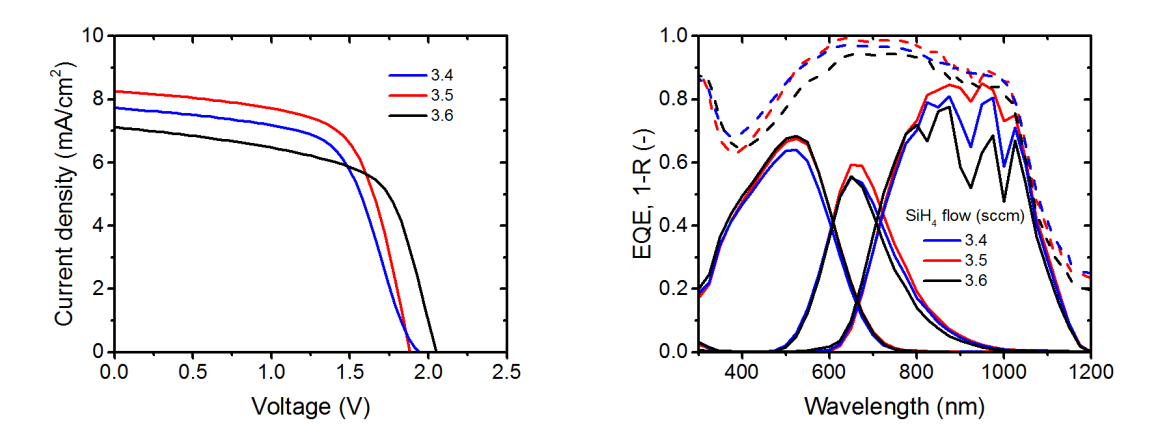


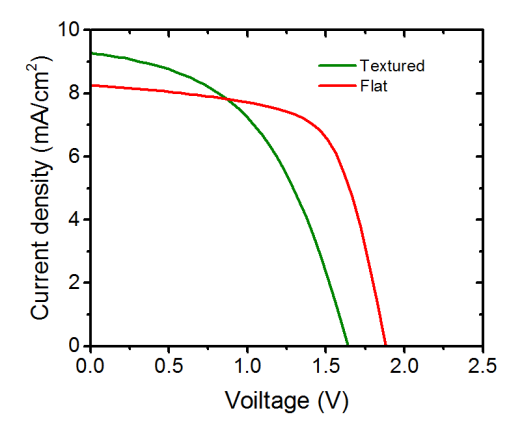
Figure 4.3: Solar cell JV characteristics and EQE of flat cells at different crystalline fractions

To determine how these parameters affect an actual triple junction cell, the devices based on these absorbers were made. First, the effect of the crystallinity was determined based on a flat device, as shown in Figure 4.3 and Table 4.1. From these results, a silane flow of 3.4 sccm seems to have added an electrical barrier in the structure, lowering the fill factor of this cell and showing a slight S shape. This might be associated with the increased grain boundaries due to the increased crystal fraction. Since the material crystallinity is higher than 60 %, it might introduce different phases in the absorber layer and creating energy barriers. [119, 120] For a flowrate of 3.6 sccm, the fill factor and open-circuit voltage are higher

than for 3.5 sccm, but the current is lowered, probably due to the fact that the crystallinity is lower and thus the middle cell absorber has a higher bandgap, closer to that of a-Si:H. This can also be observed in the EQE, where the 3.6 sccm cell has a lower absorption in the middle cell in the range around 800 nm when compared to 3.5 sccm. Thus, a silane flow of 3.5 sccm seems the most suitable, which is in accordance with the literature, suggesting that a crystallinity fraction of around 50-60 % would be optimum for thin film solar cells. [104, 118] This flow was used for further comparison between flat and textured surfaces.

	SiH_6	V_{OC}	J_{SC} top	J_{SC} middle	J_{SC} bott.	J_{SC} total	FF	Eff.
	(sccm)	(V)	(mA/cm^2)	(mA/cm^2)	(mA/cm^2)	(mA/cm^2)	(-)	(%)
Flat	3.4	1.96	8.86	7.73	15.96	32.55	0.60	9.03
	3.5	1.88	9.50	8.28	16.95	34.73	0.64	9.98
	3.6	2.03	9.58	7.14	15.17	31.89	0.63	9.07
Text.	3.5	1.64	10.04	9.25	16.97	36.26	0.48	7.32
a-Si(H)	3.5	2.03	8.65	9.20	17.14	34.99	0.60	10.57

Table 4.1: External parameters of the flat triple junction cells with different crystalline fractions



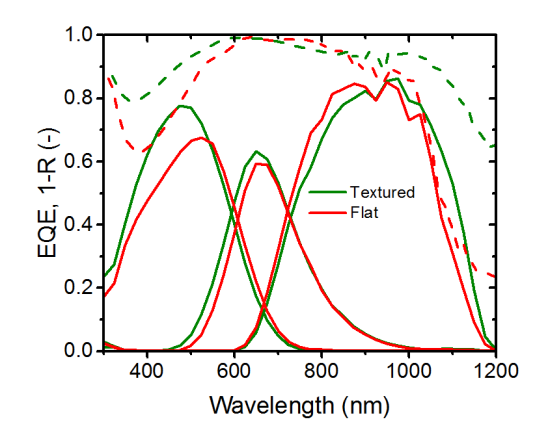


Figure 4.4: Comparison of solar cell JV characteristics and EQE of between flat and textured solar cells with a silane flow of 3.5 sccm.

When comparing the textured and flat surfaces, there seems to be a trade-off between the optical properties (current density) and the electrical properties (voltage and fill factor) of the flat and textured cells, as shown in Figure 4.4. The textured cells are able to achieve better current densities due to better light trapping characteristics, especially in the blue wavelength

range, as seen in the EQE in Figure 4.4. In addition, the R is significantly reduced, and the short circuit current achieved by the textured wafer is 9.25 mA/cm², as opposed to the 8.28 mA/cm² obtained by the flat device. Finally, the adhesion of the cells to the crystalline silicon wafer that acts as a substrate qualitatively improved, since the internal stresses in the nc-Si:H layer are reduced. However, there is a significant loss in the open-circuit voltage and fill factor when the substrate is textured, as shown in Table 4.1. In particular, the open-circuit voltage drops from 1.88 V to 1.65 V, and the fill factor is reduced from 0.64 to only 0.48. This is expected to be due to shunts that appear in the nc-Si:H and a-Si:H structures when the texture features are too sharp. [16] These losses would finally cause a reduction in overall efficiency of -2.66 % absolute, from 9.98 % to 7.32 %.

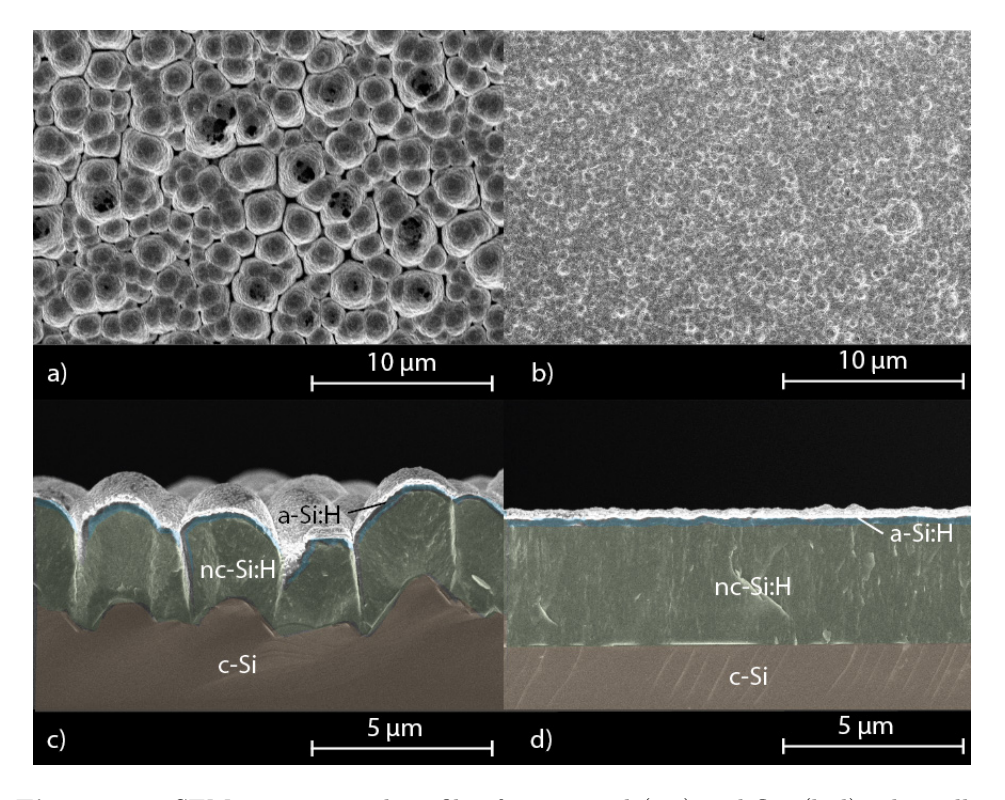


Figure 4.5: SEM top view and profile of a textured (a,c) and flat (b,d) solar cells.

To confirm the effect of the textured wafer on the nc-Si:H growth, SEM measurements have been performed, as shown in Figure 4.5. The front view of the textured samples show much bigger, and sometimes disconnected crystals. This is confirmed when looking at the profile view, where the cracks and shunts in the nc-Si:H layer are clearly apparent, as opposed to the smooth and relatively crack free layer of the flat device. This would explain the low shunt

resistance observed for the textured device in Figure 4.4. Moreover, the slightly higher series resistance of the textured device could also be related to the big grain boundaries and cracks, which can cause some disconnected areas in the TCO layer. Smoother textures on the c-Si wafer could result in less cracks and thus better fill factor and open-circuit voltage. However, such optimization is out of the scope of this work, and further experiments presented here will be performed on a flat device.

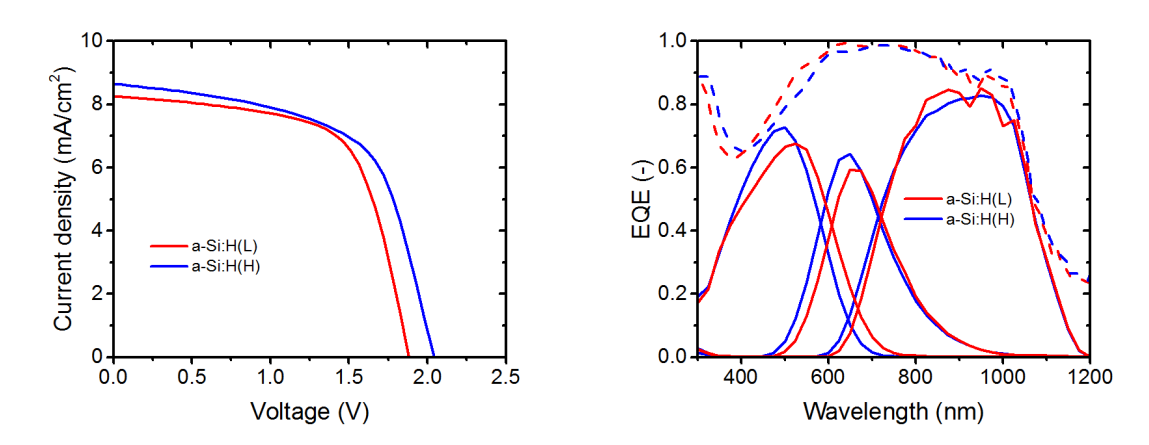
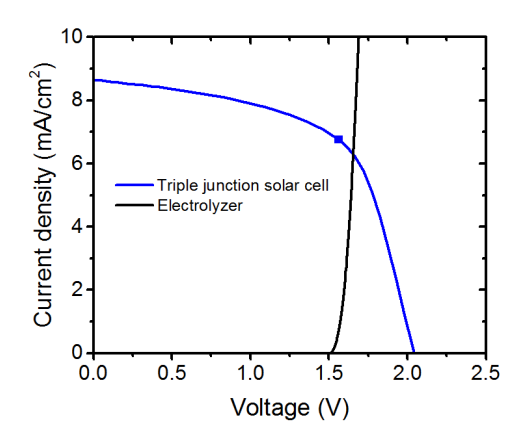


Figure 4.6: Solar cell JV characteristics and EQE of flat cells with a high bandgap a-Si:H top cell of different thicknesses.

Even though the middle absorber layer has been optimized in terms of bandgap and crystallinity, these results show that the current limiting junction would still be the middle subcell. Thus, to further optimize the cell, the top a-Si:H subcell light absorption needs to be considered. By reducing the light absorption of the top subcell, the middle cell would receive more light, and the multijunction cell would be better current matched. In order to do so, the 150 nm a-Si:H top absorber can be changed to a higher bandgap a-Si:H material previously developed, [12, 107, 121] using higher hydrogen dilution and lower deposition temperatures. In addition, the absorber thickness had to be re-optimized for the new material. The optimum thickness for the high bandgap a-Si:H is 175 nm, slightly higher than for the lower bandgap material. The comparison between the low a-Si:H bandgap and high a-Si:H bandgap is shown in Figure 4.6 and Table 4.1. The change in bandgap resulted in a higher short-circuit current density compared to the reference cell. Moreover, since the material bandgap of the top absorber is slightly higher, the resulting voltage slightly increased from 1.88 V to 2.05 V. However, compared to the previous top absorber material with a fill factor of 0.64, this cell

has a lower fill factor of 0.60, especially considering the lower shunt resistance. This suggests that the material quality is slightly decreased. Nevertheless, the overall efficiency is increased from 9.98% to 10.57%, and thus, it is the chosen configuration for driving the water splitting reaction.

To further analyze the suitability of the developed triple junction solar cell for water splitting, it was attached to an electrolyzer. The JV characteristics of both the solar cell and the electrolyzer are shown in Figure 4.7, where the intersecting point would be the operational point of the overall device. According to this comparison, the operational point would be at a voltage of 1.65 V, very close to the maximum power point of the solar cell, indicated by the square dot in the JV curve. When the device was tested for stability a relatively constant current density was achieved for the 10 h of measurement, changing only from 6.9 to 6.7 mA/cm². The resulting STH efficiency is 8.3 %. To further increase this efficiency, the FF must be increased to achieve a better fitting between the maximum power point of the solar cell and the operational point of the water splitting device. Moreover, soft textures on the substrate would also increase the operational current density without degrading the electrical properties



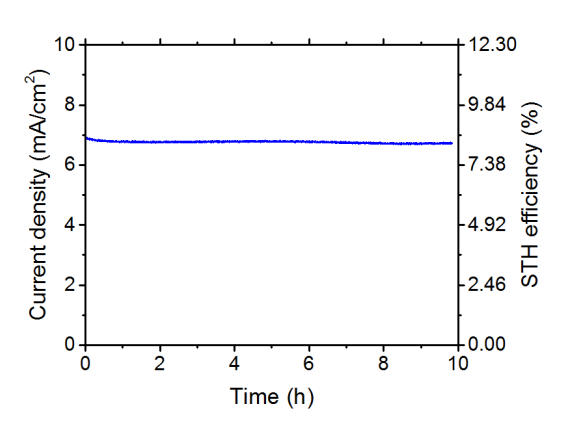
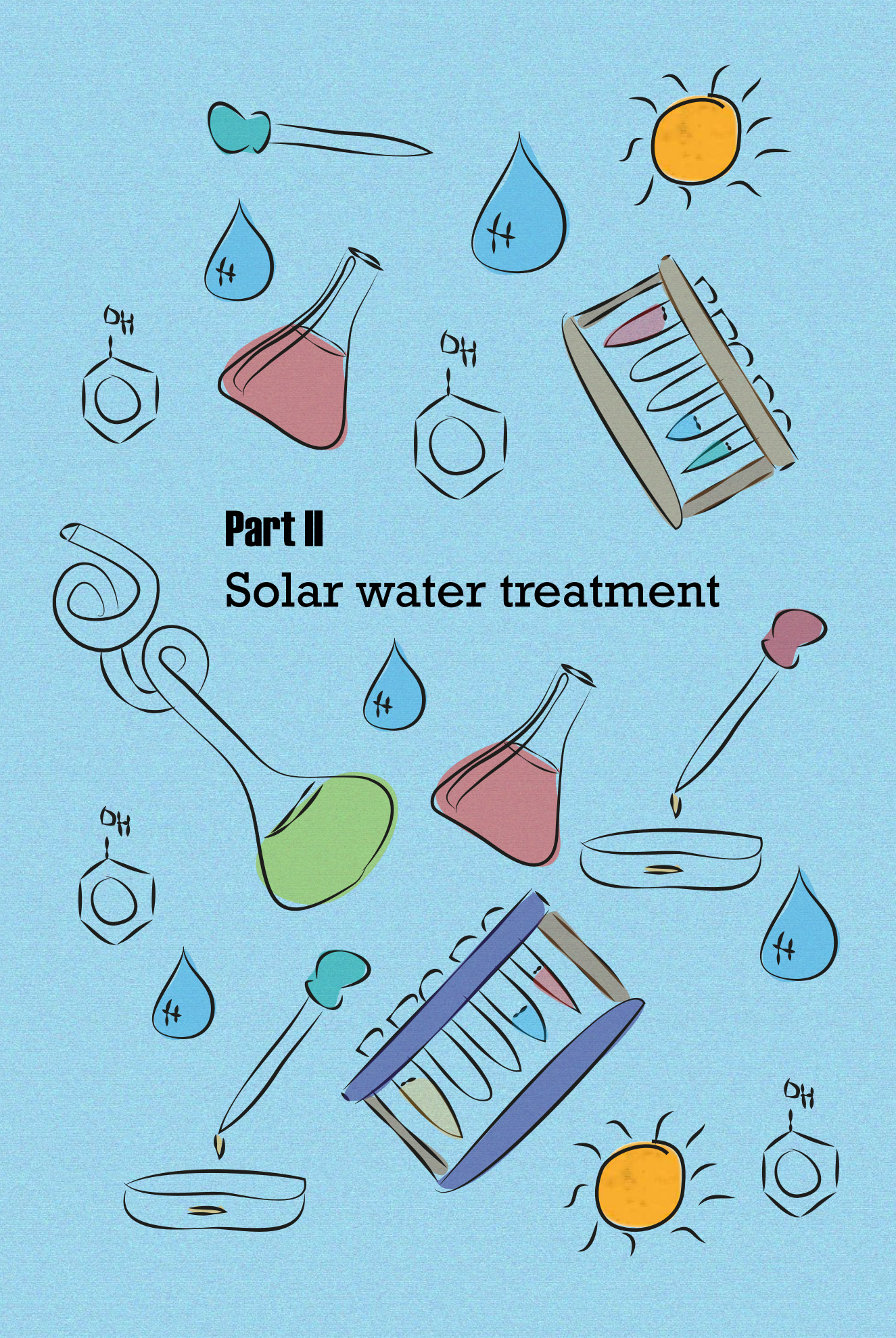


Figure 4.7: JV characteristic of the best solar cell compared to the JV characteristic of the electrolyser, and the corresponding stability characteristic of the complete system. The maximum power point of the solar cell is indicated in the JV characteristic by a square dot Note that the JV measurements and the Jt measurements were taken under two slightly different solar simulators.

4.4 Conclusions

We proposed a triple junction hybrid cell based on an a-Si:H/nc-Si:H/c-Si structure in order to effectively drive the solar water splitting reaction. Specifically, the light management is considered in order to improve the produced photocurrent, and thus the solar-to-hydrogen efficiency. The optimum crystallinity for the nc-Si:H absorber layer is determined as 52 %, which is achieved by fixing the silane flow to 3.5 sccm and a H₂ dilution flow of 120 sccm. Moreover, although wafer texturing can achieve higher current densities due to light trapping and anti-reflection effects, it also creates cracks and short circuits in the nc-Si:H absorber layer, resulting in an overall reduced open-circuit voltage, fill factor and efficiency. Thus, flat wafers are chosen as the preferred solution. Finally, to improve the current matching, a top absorber a-Si:H with a slightly higher bandgap energy was introduced. This improves the cell efficiency, achieving a solid state efficiency of 10.57 %, with a fill factor of 0.60, an open-circuit voltage of 2.05 V and a short-circuit current density of 8.65 mA/cm². When connected to an electrolyser, a STH efficiency of 8.3 % was achieved. The performance was stable for the 10 h of measurement.

:	Light management of a hybrid silicon cell for water splitting								



Oxidation of organic pollutants by a BiVO₄ photoanode and a solar cell

This chapter is based on the following publications:

- Y. Bennani, P. Perez-Rodriguez, M.J. Alani, W.A. Smith, L.C. Rietveld, M. Zeman and A.H.M. Smets. Photoelectrocatalytic oxidation of phenol for water treatment using a BiVO₄ thin-film photoanode. *Journal of Material Research*, 31(17):2627-2639, 2017.
- P. Perez-Rodriguez, Y. Bennani, M.J. Alani, W.A. Smith, L.C. Rietveld, M. Zeman, A.H.M. Smets. Treatment of Organic Pollutants Using a Solar Energy Driven Photo-oxidation Device. *Advanced Sustainable Systems*, 1:1700010, 2017.
- Y. Bennani, PhD Thesis Photoelectrocatalysis in water treatment, 2017, TU Delft.

5.1 Introduction

Access to clean water is, along with energy and food, one of the most important challenges that our society will face in the near and long term future. Currently, 1.25 billion people have no access to electricity [122] and a similar number of people have no access to clean water. [123] These problems cannot be tackled independently from each other, since poor electrification goes together with the lack of access to clean water. Thus, the main metrics used to evaluate the performance of water purification methods are cost-effectiveness and the minimum pollutant concentrations reached after purification. However, these two metrics are in competition. Costs are driven by the extent of the treatment, the energy consumption, and the usage of chemicals and other materials such as membranes. As a result, the more sophisticated treatment processes, that result in low pollutant concentrations, are typically more expensive. This work aims at decoupling these two variables by using solar methods, which would result in lower input costs, while still maintaining high degradation efficiencies.

Hazardous effluents pollute many major water supplies, caused by heavy industrialization and urbanization. Among the most common contaminants are organic pollutants such as pesticides, pharmaceuticals, phenol compounds, chloroform or dyes. [124, 125] Currently, these pollutants are hardly removed using traditional methods like filtration, chemical coagulation or aerobic and anaerobic treatments. [125–127] The biological processes are considered economically favorable, but many toxic compounds cannot be degraded by this method. [128] Physical methods such as filtration by membranes or adsorption are also widely used. [129, 130] However, in most cases these methods do not destroy the pollutants but only transfer them from one phase to another. Thus, other methods must be considered. Finally, chemical methods for water treatment offer a flexible and safe alternative to remove a wide variety of contaminants. [131] In particular, photocatalytic (PC) and photoelectrochemical (PEC) treatments are able to remove toxic organic compounds, including ecologically hazardous cyanides and other residual compounds, even at low concentrations, making this approach very suitable for the last stages of water purification. [132]

In PC water treatment, an electron-hole pair inside the material upon illumination. Both charge carriers are then separated and migrate to the catalyst/water interface, producing OH radicals that would react with the organic molecules. [51, 133] However, PC faces the problem of rapid charge carrier recombination and poor oxidation kinetics, since the charge

carriers are separated within the same particle or electrode. [134] Compared to PC, in PEC, photogenerated charge carriers are separated to different electrode materials, where they perform the catalytic process. For example, electrons migrate toward the cathode and perform a reduction reaction, while holes remain at the surface of the anode and perform an oxidation reaction. This enhances the charge carrier separation mechanisms and minimizes the recombination of electron hole pairs, thus enhancing the degradation efficiency of the chosen pollutant. [135–137]

The photoactivity of a PEC device strongly depends on the material properties, configuration of the electrode and the presence of an applied potential. [54, 55] Regarding the material choice, a wide variety of semiconductors have been studied for this purpose, being TiO₂ the most commonly studied due its favorable price and stability. [57–59] However, its bandgap energy is rather high (3.2 eV), [68] meaning that it can only be excited by UV light. Therefore, this material needs an external UV light source, which is very energy intensive, making the process less cost-effective.

Instead of using only UV light, directly utilizing the entire solar spectrum is more attractive, as it increases the amount of energy that can be converted. Solar utilization in PEC technologies may thus improve the process effectiveness without substantially increasing the costs of the water treatment. Suitable materials with good solar spectrum utilization are bismuth based compounds. [64, 65] In particular, BiVO₄ is a suitable material to use as a photoanode due to its bandgap energy of approximately 2.4 eV, high stability and low price. BiVO₄ is already used as a yellow pigment for paint and has been successfully demonstrated as a promising photoanode for solar water splitting and other photoelectrochemical reactions. [138–141] It has also been used for photocatalytic degradation of contaminants in a spindle-like structure modified by polyaniline (PANI/BiVO₄), as a nanostructured electrode, and in a heterostructure as a photocatalyst for dye degradation. [70, 142, 143] These films are especially suited due to their easy deposition process [39] and their compatibility with light trapping structures such as surface texturing, already widely applied in solar cells. [41, 144]

In this study, we propose BiVO₄ as a photoelectrode for the oxidation of phenol and other organic pollutants in water. Phenol has been chosen as a representative organic contaminant due to its toxicity at high concentrations, potential harm at low concentrations, and its easy detection using a UV/Vis spectrophotometer. [53] Due to the novelty associated with

BiVO₄ in the water treatment field, this study characterizes the BiVO₄ film properties to explain the suitability of the material for PEC water treatment using solar illumination. The performance as a photoanode for water treatment is associated with the optical, electrical, and catalytic properties of BiVO₄. Absorption spectrophotometry characterizes the optical properties of the semiconductor. The electrical properties, which affect the charge carrier separation process, were determined by electrochemical impedance spectroscopy (EIS), dark conductivity, and cyclic voltammetry measurements. Atomic force microscopy (AFM) was used to characterize the surface morphology of the photoelectrodes, which is also an important feature affecting the chemical activity. Furthermore, since the internal structure of the atoms can affect all of these properties, x-ray diffraction (XRD) measurements were conducted to determine the crystal phase composition of the films. Finally, the suitability of the films for water treatment was tested by determining the incident photon to current efficiency (IPCE) and the efficiency of this photocatalyst for phenol oxidation. The photoactive characteristics of BiVO₄ were compared with TiO₂, one of the most widely used semiconductors for photocatalytic water treatment. [53, 145] In addition, a gradient doping of BiVO₄ with tungsten (W) was studied to improve the charge carrier separation in the material. This improvement can potentially promote the photocatalytic activity and degradation efficiency, as already shown for the case of solar water splitting. [39, 70]

However, a potential difference needs to be produced inside the material so that the charge carriers are able to deliver enough energy to the electrolyte to drive the reaction. Since these semiconductors are not able to produce such high potentials by themselves, an external bias voltage is needed. Here, we propose to use a solar cell that utilizes the spectrum transmitted by the BiVO₄ photoanode, as illustrated in Figure 5.1, to create the voltage needed as extra bias. The options available include III-V technologies, perovskites, crystalline silicon (c-Si), thin-film amorphous and nanocrystalline silicon (a-Si and nc-Si), and CIGS. [7, 8] Depending on the needed voltage, multijunction solar cells, which consist of several cells monolithically stacked and series connected, may be required. [146–148] Thin-film silicon was chosen due to the flexibility of its design, know-how on possible multijunction devices, relative stability of the devices and the low cost of materials. [149] The final device would consist of a photelectrode, a solar cell and a counter electrode. To realize this device, each element will be analyzed separately, including the photoanode, counter electrode and supporting solar cell.

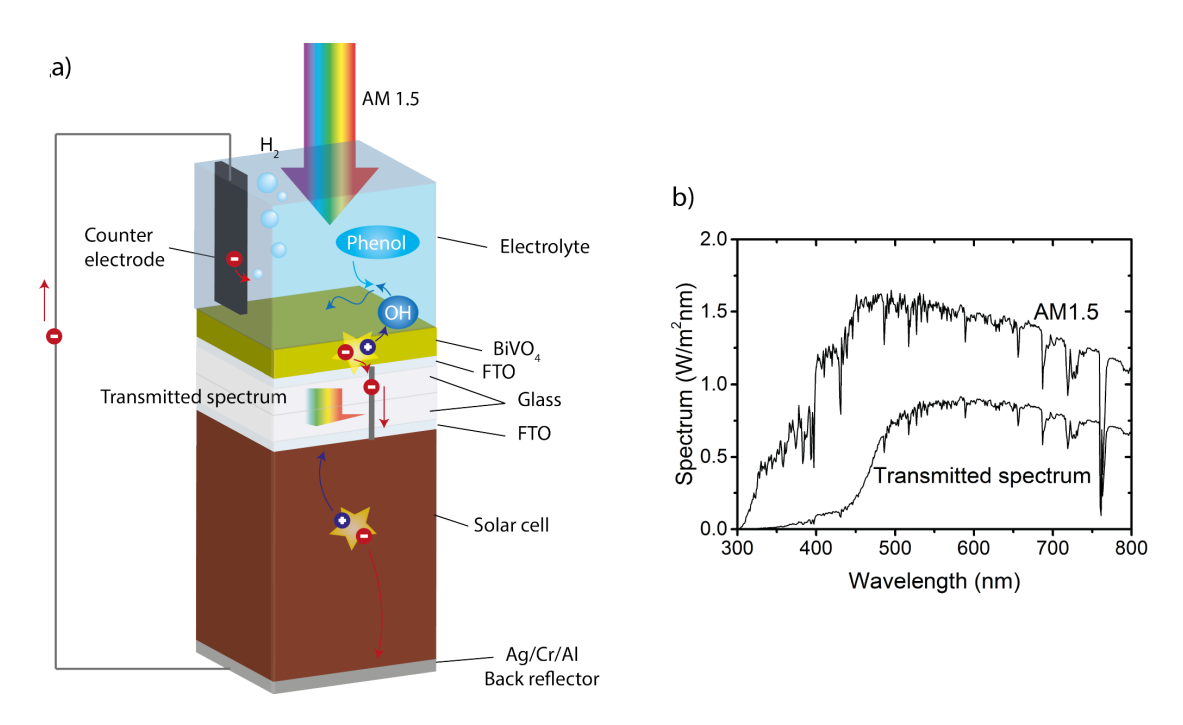


Figure 5.1: a) Schematic of a stand-alone device configuration combining a BiVO₄ photoanode and a solar cell and b) the AM1.5 spectrum compared to the transmitted spectrum after the $BiVO_4$ photoanode

5.2 Materials and methods

5.2.1 Fabrication methods

BiVO₄ fabrication The BiVO₄ thin films were synthesized via spray pyrolysis. The substrate was commercial Asahi UV type (textured glass with an FTO coating), and it was cleaned using a sequence of acetone and isopropanol solutions. Prior to the BiVO₄ deposition, a thin layer of 5 nm SnO₂ was deposited to avoid recombination in the FTO/semiconductor interface. For the BiVO₄ thin film spraying, a precursor solution was needed. The precursor solution was made by mixing a 19.4 g/L Bi(NO₃)₃5H₂O (98% Alfa Aesar) solution in acetic acid (AcAc) (98% Sigma Aldrich) with a 1.7 g/L V(AcAc)₂ (99% Alfa Aesar) solution in absolute ethanol (Sigma Aldrich) in equimolar quantities. This solution was then pumped through a nozzle and sprayed onto the substrate, which was 20 cm away from the nozzle and kept at a temperature of 450 °C. Each spray cycle consisted of 5 s of spraying at a rate of 0.2 mL/s followed by a 55 s idle to allow the solvents to evaporate off the substrate, leaving behind BiVO₄. After deposition, the samples were annealed in a furnace with air. The temperature was raised to 450 °C at 5 °C/min and then maintained for 2 h. By modifying the

spray time, different thicknesses were deposited (200, 250, 300, and 350 nm). The contacts were deposited as a 300 nm stripe of aluminum on the TCO by electron beam physical vapor deposition (EBPVD). To fabricate tungsten (W)-doped BiVO₄ with gradient doping from 1% W in contact with the TCO to 0% W at the surface, the precursor solution was made with a 1% W content, and then V containing solution without W was added in steps. When depositing 1% W-doped BiVO₄, W(C₂H₅O)₆ was added to the V(AcAc)₂ solution prior to the mixing with the Bi(NO₃)₃ solution.

TiO₂ film electrodes were manufactured by Magneto special anodes B.V. (Schiedam, The Netherlands) according to the paint-thermal decomposition method. [53] Electrodes coated with TiO₂ film were prepared by applying a layer of a solution containing an organic, solvent-based titanium oxide precursor on a flat titanium substrate. After air drying for several hours, the support with paint was transferred to an air-circulating oven for its first heat treatment at temperatures between 400 °C and 600 °C for 2 h. This heat treatment decomposed and oxidized the salt, giving an oxide layer. Up to six layers of paint were applied first, followed by drying and heat treatment for all the applied layers. [150] The TiO₂ film electrodes were further modified by an annealing process, to gain the optimal ratio of anatase to rutile crystals in the TiO₂ structure. [54] The annealing treatment of the TiO₂ film was carried out in a furnace (NeyTech Vulcan Benchtop Muffle Furnace 3–550, Cole-Parmer, Schiedam, The Netherlands), according to the procedures already used in a previous study. [54] The TiO₂ film was annealed for five hours at ambient pressure at 650 °C, and the temperature was ramped up at 8 °C/min from room temperature. The final thickness of the TiO₂ was 2.04 μm and anatase to rutile ratio (A/R) was 82/18. [54]

Solar cell fabrication The solar cells were deposited by plasma enhanced chemical vapour deposition (RF-PECVD) using a cluster tool from Electtrorava. The a-Si:H and a-Si:H/a-Si:H solar cells were deposited on Asahi UV substrates, while the a-Si:H/nc-Si:H solar cells were deposited in wet etched textured glass with Aluminium-doped Zinc Oxide (AZO) as a transparent conductive oxide (TCO). The texturing of the glass used for the a-Si:H/nc-Si:H cell is described elsewhere. [151] Nanocrystalline silicon oxide (nc-SiO_x:H) was used as player (boron doped) and n-layer (phosphorous doped). The thickness of the absorber layers (intrinsic a-Si:H and nc-Si:H) has been tuned by varying the deposition time. The deposition rates of a-Si:H and nc-Si:H were 0.16 and 0.71 nm/s, respectively. The contacts have been

deposited using electron beam physical vapour deposition (EBPVD). A 300 nm Al stripe in contact with the TCO has been used as front contact. A stack of 200 nm Ag, 30 nm Cr and 500 nm Al has been used as back reflector and back contact. The solar cell area was 1 cm².

5.2.2 Characterization

X-ray diffraction (XRD) For the BiVO₄ and TiO₂ films, quantification of the phase proportions was carried out by XRD (Bruker D8 Advanced diffractometer Bragg-Brentano with graphite monochromator and Vantec position sensitive detector; Bruker Corporation, Leiderdorp, The Netherlands). [152] The analyses for the TiO₂ film were done using the method described by Spurr and Myers, which utilizes the ratio of the rutile (110) peak at 27.355 H₂ to the anatase (101) peak at 25.176 H₂. The X-ray film diffraction patterns were obtained using the Bruker D8 Discover with Eulerian cradle (Bruker Corporation), goniometer radius 300 mm. [153] The BiVO₄ measurements were coupled H-H₂ scan 10–110° with step size 0.034° H₂.

Absorbance spectrophotometry The optical properties were determined by measuring the reflectance, transmittance, and absorbance using the spectrophotometer PerkinElmer Lambda 950 UV/VIS (PerkinElmer, Waltham, Massachusetts). The optical band gap of the material was determined using a Tauc plot. [154] In this method, $(\alpha h\nu)^{1/2}$ is displayed against $h\nu$, in which α is the absorption coefficient, h is Planck's constant, and ν is the frequency. Such plot shows a distinct linear regime that corresponds to the onset of the absorption. By extrapolating this linear trend to the abscissa, the energy of the optical band gap was determined.

Atomic force microscopy (AFM) Surface roughness was measured by AFM (NTMDT Ntegra, Moscow, Russia). Commercially available tips (Digital Instruments standard tips) were used and the surface was imaged in tapping mode. The BiVO₄ films deposited on textured glass were investigated. The roughness of the film surface was quantified by means of a statistical data analysis of AFM images. The most used parameters in characterizing the surface topography are the average roughness (R_a) and the root mean square (RMS) roughness. The RMS roughness takes the mean squared absolute values of the surface roughness profile, making it more sensitive to peaks and valleys than the average roughness. RMS is particularly used to study temporal changes in the creation of a new surface as well as spatial differences when studying the surface feature using different scales. [155]

Incident photon-to-current conversion efficiency (IPCE) To estimate the maximum possible conversion efficiency and gain more insight about the limiting factors in the photoelectrodes, IPCE was measured. The IPCE represents the fraction of incident photons that is converted to electrons (that are used to drive catalysis for PEC) and can be measured in the external circuit as a function of wavelength. An incident light beam from a Newport 6902, 150 W Xe gas discharge lamp was modified to a single wavelength by a Oriel Cornerstone 130 monochromator (Oriel Instruments, Stratford, Connecticut) and a Keithley 236 source. The measurement was done for a wavelength range from 300 nm to 600 nm with a step size of 6 nm. The photocurrent was measured with respect to the wavelength of the incident light. The potential applied during this measurement is 1 V vs. Ag/AgCl. The photoelectrochemical cell used for the IPCE measurements consisted of a fused silica window through which the incident light entered. The working solution was contained in the central chamber into which the platinum counter electrode (CE) and the Ag/AgCl reference electrode were immersed via separate ports. A calibrated photodiode measured the intensity of the incident light. An EG&G potentiostat controlled the potential of the photocathode and measured the current. From the obtained photocurrent the IPCE was calculated.

Electrochemical impedance spectroscopy (EIS) The photoelectrochemical performance is largely dependent on charge carrier transfer and the level of recombination of the photocatalyst. [156] EIS was used to analyze the charge carrier transfer and recombination processes at the photocatalyst/electrolyte interface. [157] Impedance is represented as a complex number, where the reactance is the imaginary part and the resistance is the real part. The real part is plotted on the x-axis and the imaginary part is plotted on the y-axis. [156] The EIS was conducted while maintaining a direct current voltage between the working electrode and the reference electrode. EIS was performed at a potential of 1 V vs. Ag/AgCl, with a perturbation amplitude of 0.1 V and in the range of frequencies from 105 to 0.01 Hz. The values were measured in both dark and light periods. To interpret the EIS data, the electrochemical system was simplified to an equivalent electrical circuit model. This model uses a combination of resistance, capacitance and other electrical elements, which have a clear physical meaning, related with the response of the electrochemical system. [53] In this work the characteristic equivalent circuit model presented in Figure 5.2 was used. The simple circuit consists of a series resistor (R_s) connected to a resistor (R_p) and capacitor (C_p) in parallel. This circuit model has been used to describe a similar EIS responses. [158] The impedance is expressed in a Nyquist plot. The left intersection with the x-axis is the solution resistance (R_s, Ω) and

the diameter of the semicircle is the charge transfer resistance (R_p , Ω). The double-layer capacitance is equal to:

$$C_{dl} = \frac{1}{\omega R_{ct}} \tag{5.1}$$

where $\omega = 2\pi f$ is the angular frequency and f [Hz] is the frequency at the top of the semicircle. [158]

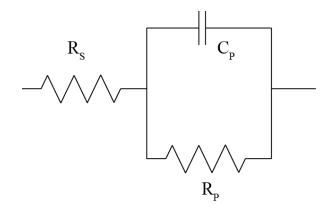


Figure 5.2: The equivalent circuit model representing the EIS response of the films.

Solar cell characterization External Quantum Efficiency (EQE) was measured in an inhouse setup in TU Delft, the Netherlands, to obtain the amount of charge carriers generated per photon of a given wavelength incident on the solar cell. The JV curves of the solar cells have been measured using a Wacom solar simulator (Class AAA), and the short-circuit current density has been corrected with the value obtained from the integration of the EQE weighted with the AM1.5 spectrum. The BiVO₄ photoanode has been used as a filter to obtain the transmitted spectrum during both measurement.

Phenol degradation experiments Photoelectrochemical experiments for phenol degradation were carried out in a set-up consisting of a cylindrical quartz glass reactor with an effective vessel volume of 300 mL, an external solar light source Atlas solar simulator (SUNTEST XXL1, Atlas Material Testing Technology LLC, Deerlijk, Belgium), consisting of a day filter, three Xenon lamps irradiating solar light (UV 300–400) with intensity of 60 W/m² in the wavelength region between 300 and 400 nm, and a three-electrode configuration. [136] The initial volume of the working solution was 250 mL phenol (99%, Sigma Aldrich) with initial concentration of 20 mg/L. Demineralized water (RiOs 5 Reverse Osmosis System, RiOs Essential, Amsterdam, The Netherlands) was used throughout the experiments for dilution. To eliminate the influence of solution resistance, 14.2 g/L Na₂SO₄ was chosen as the supporting electrolyte because it is an inert electrolyte which does not produce any reactive species during the photo(electro)lysis, except under special conditions where it may generate

persulfate. [159, 160] It is possible that the presence of the inorganic ions in the reaction medium can modify the oxidation rate of the organic compounds as function of their nature and concentration. [161] Inorganic anions can scavenge the OH radicals to form the corresponding anion radicals. Additionally, as function of the nature of the inorganic anions, at higher concentrations of 0.1 mol/L, the inhibition order of oxidation rate is the following: $H_2PO_4^- > Cl^- > HCO_3^- > CO_3^{2-} > SO_4^{2-}$. [162, 163] However, Zhu et al. found that OH scavenging by Cl^- , SO_4^{2-} or HPO_4^{2-} or direct oxidation of organics did not influence the reaction rate. [162] The 2 mL samples were collected from the reaction solution at regular time intervals (every 1 h), added to a cuvette and measured with a UV/Vis spectrophotometer to determine the absorption/residual concentration of phenol. The phenol concentration was monitored with a Hach Lange DR 5000 spectrophotometer (Hach, Düsseldorf, Germany) by using Hach Lange cuvette tests (LCK 345 with a measuring range of 0.05–5.00, 5–50 and 20–200 mg/L, [128] diazotized 4-nitroaniline method).

Unless otherwise indicated, the photoanodes used in this experiment had an active surface area of 16 cm². At the start of each experiment, the TiO₂/Ti and BiVO₄ electrodes were kept in the stirred phenol solution in the dark for one hour for adsorption to reach equilibrium. A graphite plate was used as a cathode and placed at a distance of 1 cm from the anode. The pH of the solution was kept constant at 7.2 and was measured before the experiment, using a Sentix 81 pH meter (Sentix, Weilheim, Germany). The temperature was maintained at 25±1 °C by recirculating cooling water in a water bath equipped with a cooler (FL300, Julabo, Seelbach, Germany). During the experiments, the reactor was closed using a UV permeable quartz lid to prevent phenol from evaporating. The electrode potential and working current were controlled with a potentiostat-galvanostat system (Autolab PGSTAT128N with a BOOSTER10A, Metrohm Autolab, Utrecht, The Netherlands). An Ag/AgCl electrode was used as the reference electrode. Nova software provided the electrochemistry routine software, which included chronoamperometry (CA), cyclic voltammetry (CV), and EIS. The phenol photodegradation experiments using BiVO₄ were performed by applying different potentials, ranging from 0 to 1.2 V (vs. Ag/AgCl, KCl saturated), to determine the optimum working point. The optimal potential for TiO₂/Ti composite electrode of 1 V (vs. Ag/AgCl, KCl saturated) was taken from previous studies. [136] Dark current and photocurrent were recorded, and the net current was then calculated by subtracting dark current from photocurrent to determine the photoactivity of the films.

5.3 Results and discussion

The different elements studied in this work are the photoelectrode, focusing on a BiVO₄ photoanode, the counter electrode, and the solar cell that would provide the necessary additional voltage. Finally, an energy balance was performed to show the potential of this approach.

5.3.1 Photoelectrode Characterization

The performance of BiVO₄ as a photoanode for water treatment depends partly on the optical properties of the material. The light absorption of the different photocatalysts studied is shown in Figure 5.3, as well as the reflectance and transmittance of each sample. Using a Tauc plot, it was determined that the optical band gap of the undoped BiVO₄ is $2.47~\pm$ 0.02 eV, while TiO_2 a band gap of 3.30 eV. The band gap energy of the 1% W gradient doped samples (2.53 eV) was found to be slightly bigger than the one for undoped BiVO₄ (2.47 eV). At longer wavelengths than those corresponding to the band gap (lower energies), the observed absorption is attributed to the substrate, namely FTO coated textured glass for BiVO₄ and Ti plate for the TiO₂/Ti composite. This would explain the much higher values in the case of the TiO₂/Ti. Regarding the thickness of the BiVO₄ films, it could be expected that the thicker the film, the higher the light absorption. However, in this case the highest light absorption was obtained with a 250 nm BiVO₄ sample. The slightly lower absorption in the thicker 300 nm BiVO₄ could be explained by the reflection and transmittance measurements (Figure 5.3c) and d)). The reflection of the 300 nm BiVO₄ was higher with respect to the other two thicknesses, suggesting that at 300 nm the surface structure could have changed, as can be seen for the 350 nm sample, leading to an increased reflectance and reduced light absorption. This effect was seen in all three samples made of undoped 300 nm BiVO₄ film and not in the samples made at other thicknesses. However, the phenomenon of higher reflectance at certain thicknesses was not observed in the case of tungsten (W) doped BiVO₄ samples (Figure 5.3a)), in which the light absorption follows the trend of the increasing thickness of the film.

It is known from the photovoltaic field that the surface texture highly affects the optical properties of devices, especially of thin film devices. [144, 157] Therefore, to assess the role of the surface roughness on the optical properties seen in the absorption measurements, AFM measurements were performed. In addition to the optical effects, the semiconductor surface area is also important for the electrode activity, since the area in contact with the electrolyte

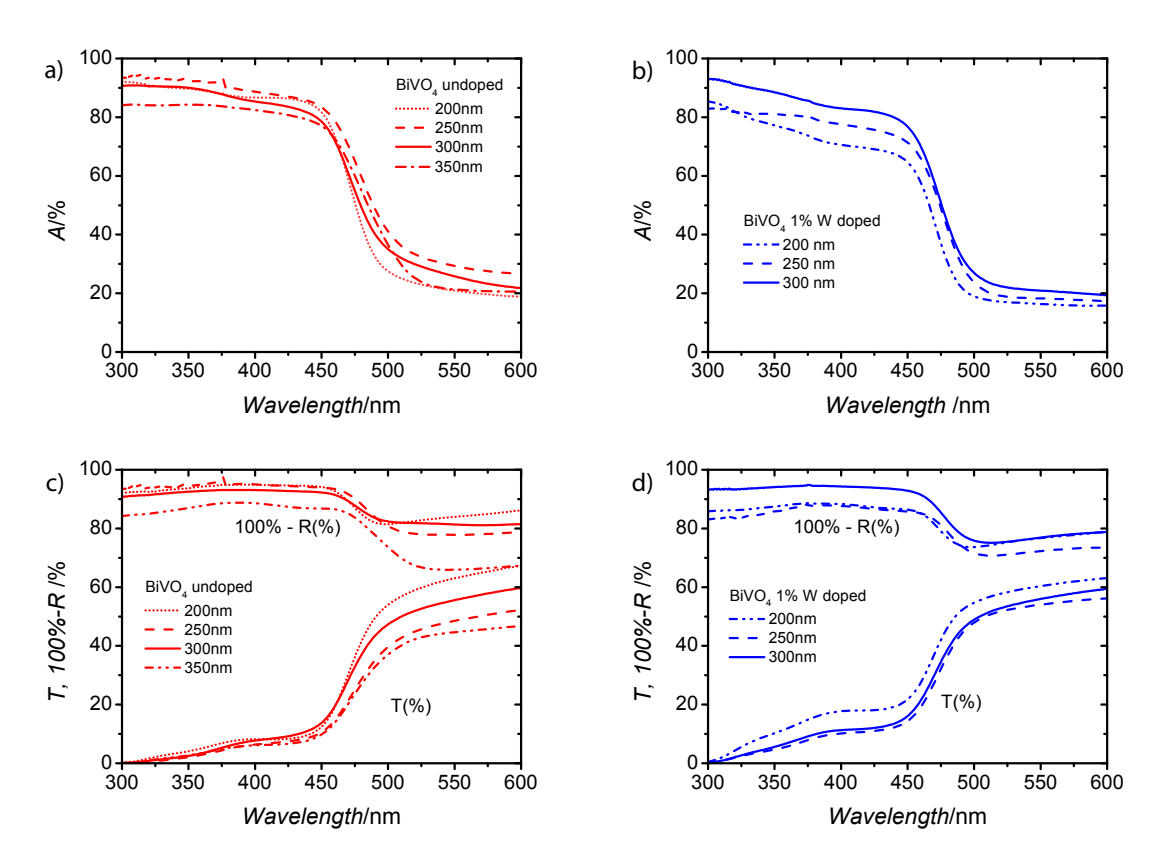


Figure 5.3: Absorption of light on a) both TiO_2/Ti composite and undoped $BiVO_4$ films, b) and 1% W gradient doped $BiVO_4$ films, and reflectance and transmittance of c) undoped and d) 1% W gradient doped $BiVO_4$ at different wavelengths.

should be increased to enhance the number of catalytically active sites. Thus, a higher surface area will generally translate into higher reaction rates. Figure 5.4 shows the AFM measurements of the different BiVO₄ samples to determine how the surface characteristics change with thickness and doping. It can be seen that the surface roughness of undoped samples increases with thicknesses up to 300 nm and the decreases. These differences add to the hypothesis that varying surface texturing at different thicknesses affects the optical properties. The relatively flat roughness of the undoped 350 nm sample would correspond to the relatively high reflectance with respect to the other samples seen in Figure 5.3c). The reasons for this surface change might be related to the phases present in the film. To determine that, the crystal structure was studied.

The crystal properties of the films were determined using XRD. The two possible structures

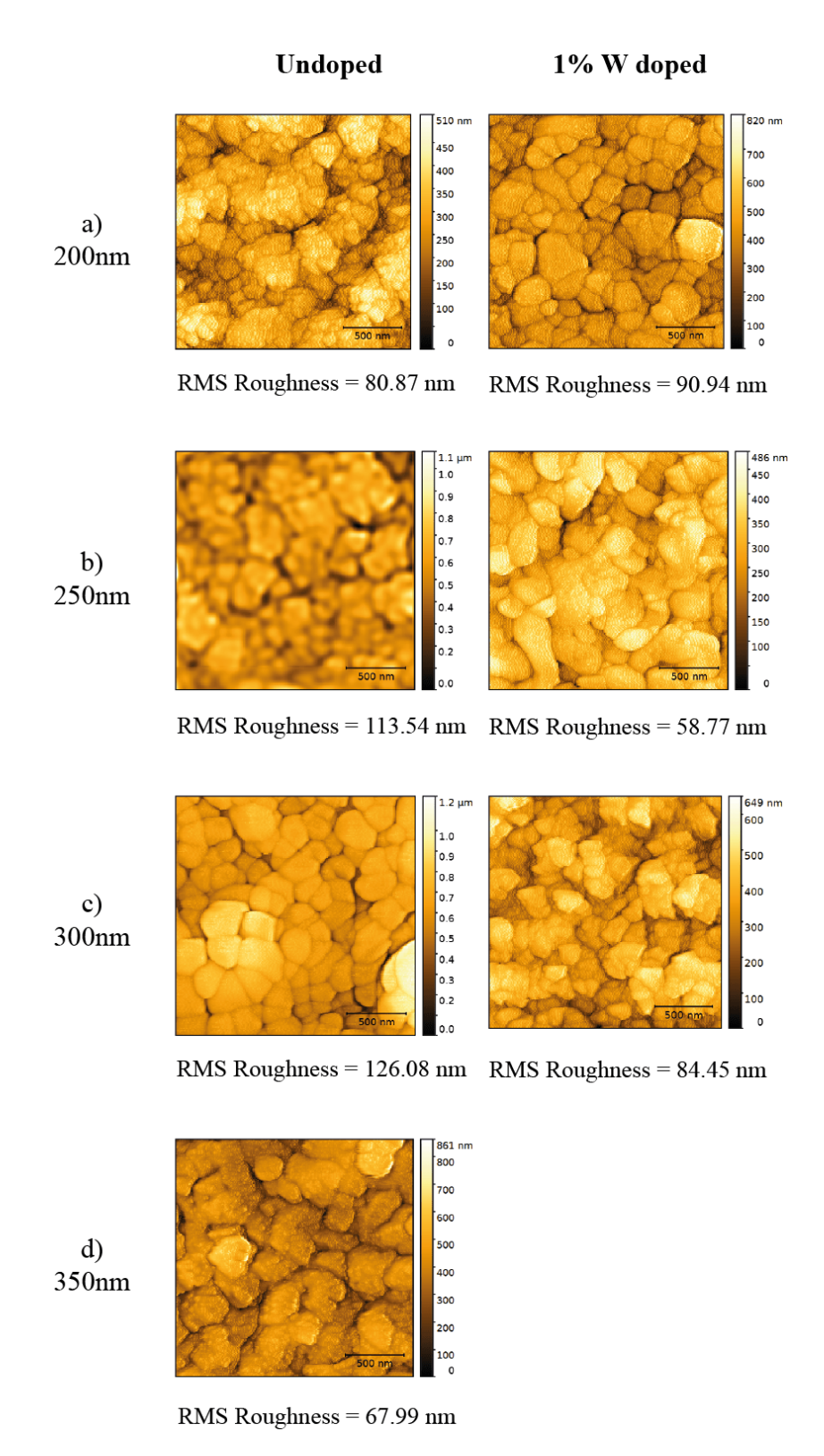


Figure 5.4: AFM scans from the different thicknesses a) 200 nm, b) 250 nm, c) 300 nm and d) 350 nm for 1% gradient W doped and undoped BiVO₄.

for the synthesized BiVO₄ are tetragonal crystals or monoclinic scheelite. [164] Monoclinic scheelite has more local distortion, which is claimed to result in a higher photocatalytic activity due to an increase in local polarization. [165] Figure 5.5 shows the XRD pattern of doped and undoped BiVO₄ at different thicknesses, where the vertical lines represent the characteristic peaks of monoclinic scheelite and the dots represent the FTO peaks. [166] The interpretation of these samples suggests that the amount of monoclinic scheelite increased when the thickness of the sample increased up to 300 nm, being especially noticeable for the undoped samples. That could also explain the differences in reflection and transmission seen in Figure 5.3b). The crystal structure depends on the heating process during fabrication and subsequent annealing. [129] This phenomenon may thus be caused by the fact that thicker samples have a longer deposition time, and therefore they are exposed to high temperatures for a longer time. Additionally, inhomogeneities in the annealing process due to the possible temperature profiles could have an effect on the crystal structure.

From these values, it can be seen what the 300 nm undoped BiVO₄ presents a much higher monoclinic scheelite peak than the rest of the samples, suggesting that at 300 nm, a phase change occurred, showing a bigger amount of monoclinic scheelite in the film. Also, it is important to note that the 1% W gradient doped samples have a lower peak height than the undoped samples, suggesting that the W doping affected the crystal properties of the material. In addition, a slight increase of the peak intensity of the 1% W doped samples can be observed with increasing thicknesses.

Since BiVO₄ is being used as a photoelectrode, the PEC oxidation process involves not only the optical and surface properties, but also the electrical properties. Figure 5.6 shows the Nyquist plot of the undoped and doped BiVO₄ thin films. The doped samples mostly showed a lower Z''for lower thicknesses compared to the undoped samples, which is related to the improved charge carrier separation by the electric field created inside the film with doping. However, the resistance in the 300 nm doped samples is the highest among all the samples. That is associated with the increase in defect density by doping and the reduction of the diffusion length of the charge carriers. Regarding the thickness dependence of undoped samples, the resistance to charge carrier transport reduced with increasing thickness, especially in the case of 300 nm. This might be related to a higher conductivity of the monoclinic scheelite. However, for doped samples the resistance to charge carrier transfer increased with

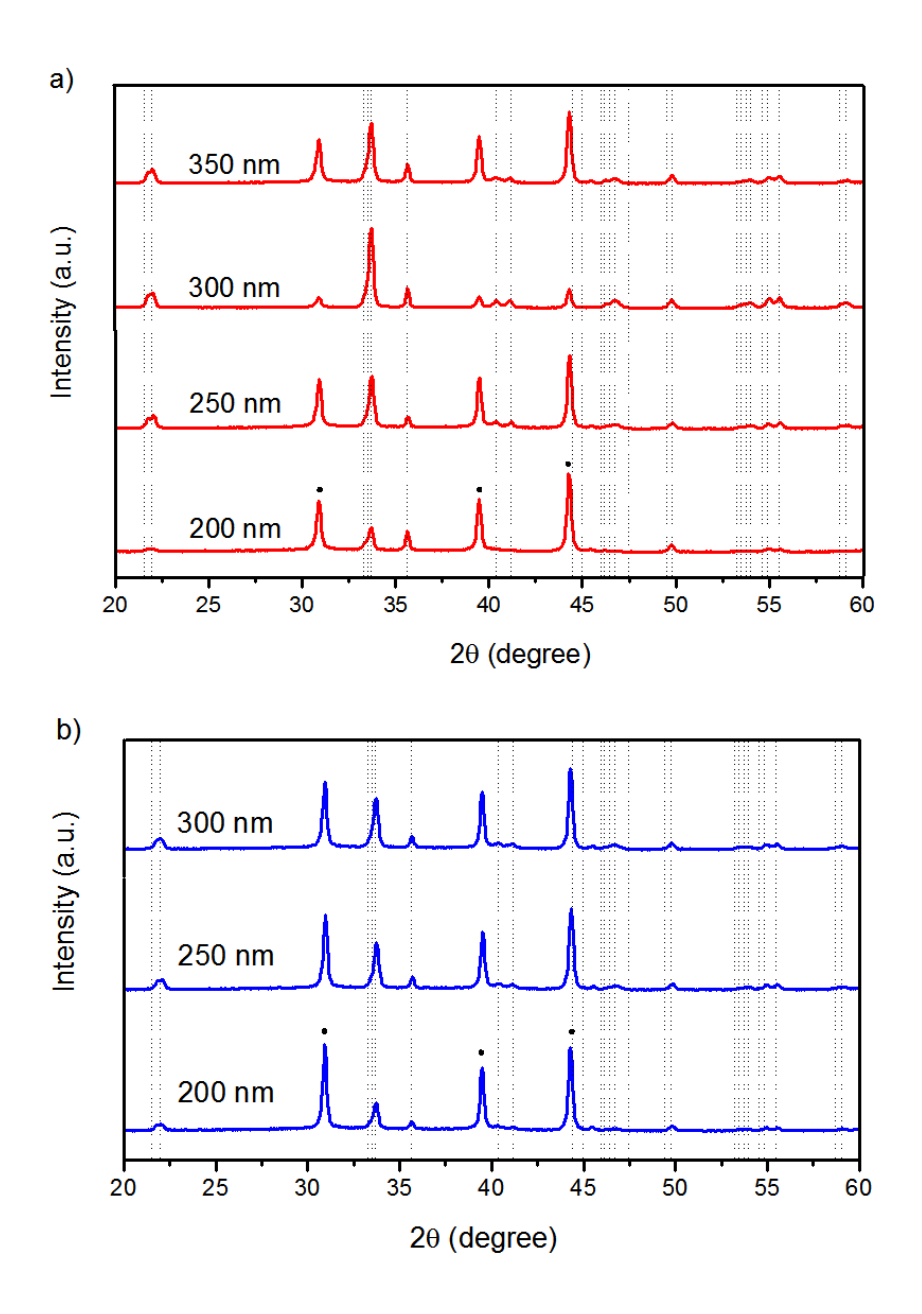


Figure 5.5: XRD pattern of samples of $BiVO_4$ a) undoped and b) 1% W gradient doped on FTO. The dotted peaks represent the FTO peaks and the vertical lines represent the monoclinic scheelite peaks. The intensity of the XRD signal has been adapted to fit in the graph, but it must be noted that the signal of all the FTO peaks is approximately the same in all cases since the substrate is the same, and thus they must be taken as a reference.

increasing thickness. When introducing doping, more defects were created in the film, reducing the diffusion length of the charge carriers inside the material which thereby increases the Z'impedance. Another outcome from the EIS study is related to the solution resistance (R_S). Despite the solution being the same in all cases, there is a shift in the origin of the curve (Figures 5.6a) and b)) related to variations in R_S . These changes are associated with variations in the surface because of structural changes in the material phase, as shown previously.

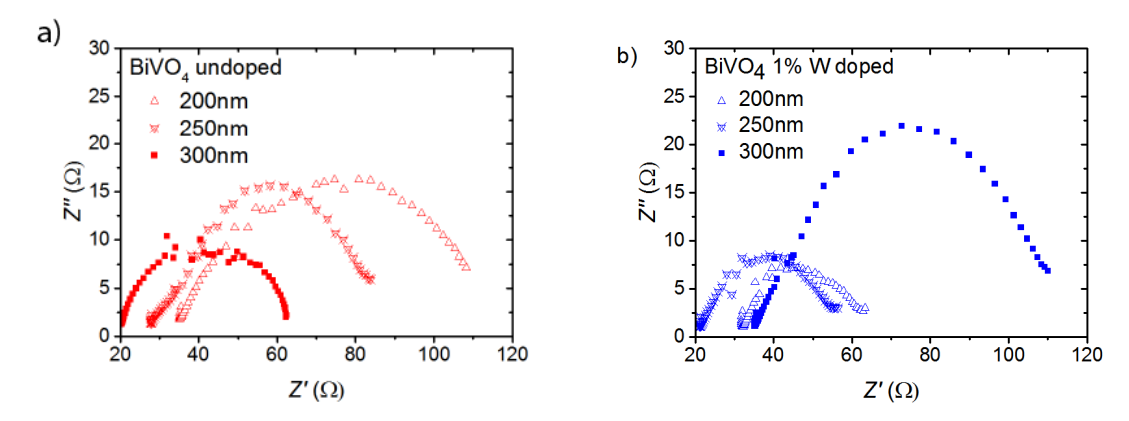


Figure 5.6: EIS measurements of a) undoped $BiVO_4$ and b) 1% W gradient doped $BiVO_4$ samples in phenol solution under solar light.

Finally, the photoresponse of BiVO₄ is an important measure to determine how well the optical and electrical properties translate into the actual photoelectrochemical performance. Due to the electrical defect structure of the material, not all the energy of an absorbed photon was converted directly into current. The IPCE, shown in Figure 5.7, gives more information about the actual conversion efficiency from photons into current that is used in the chemical reaction. Due to the band gap of each material, TiO₂ produced a measurable current only at wavelengths lower than 400 nm, with a peak at a wavelength between 350 and 370 nm (Figure 5.7 a)). Undoped BiVO₄ films showed a peak around 450 nm, due to its lower band gap energy compared to TiO₂. Increasing the thickness of the undoped BiVO₄ film increased the IPCE response due to the higher light absorption of the material. The doped samples showed a better IPCE response for the 200 nm, mainly due to the enhancement of the charge carrier separation. However, when the thickness is increased, the IPCE decreased. This could be the sign of electron transport loss occurring by enhanced electron generation at higher BiVO₄ loading and doping. The mentioned phenomena reflect that there is an additional resistance between interconnected BiVO₄ structures and doped elements which can be seen

in Figure 5.6b) as an increase in impedance with increase of the thickness layer, suggesting a higher recombination of the charge carriers. [167]

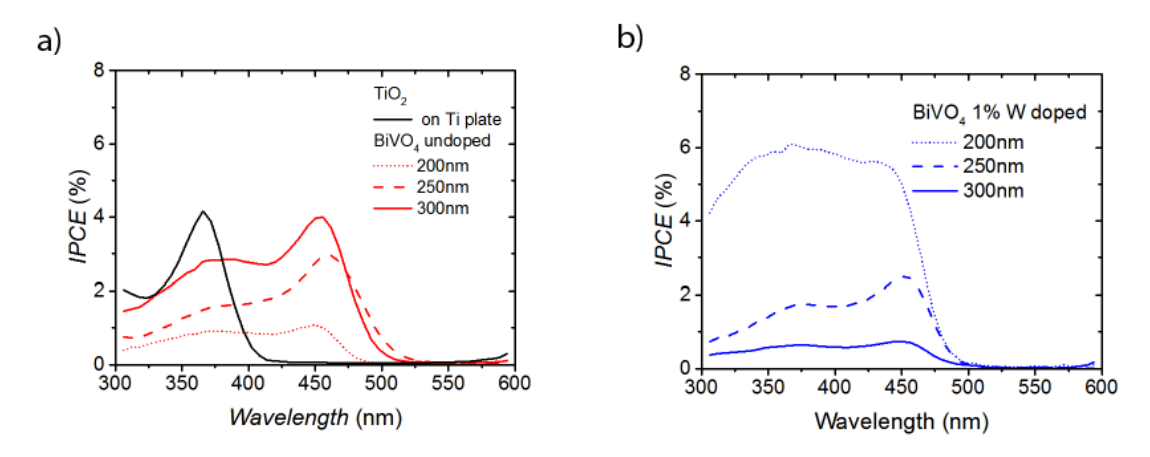


Figure 5.7: IPCE measurements for a) TiO₂ and BiVO₄ undoped and b) BiVO₄ 1% W gradient doped electrodes using front illumination.

The optical, structural, and electrical properties have been summarized in Figure 5.8. The absorption and IPCE values shown in this graph are taken at a wavelength of 450 nm because, since it is slightly above the band gap energy, it can be used as a comparison of the absorption for the different samples. To compare the different XRD measurements, the monoclinic scheelite peak at 35.68 degrees has been normalized with the FTO peak at 30.92 degrees. These peaks have been chosen as representative of the amount of monoclinic scheelite in BiVO₄ because of their unlikely interaction with other peaks. It can be seen in Figure 5.8a) that the optical band gap does not significantly change with thickness or doping. The absorption at a wavelength of 450 nm increased with thickness for the doped samples, but showed a maximum at 250 nm for the undoped samples. The peaks at 300 nm in the RMS roughness and XRD peak suggest that there was a change in the structure and surface morphology after 300 nm that translate in a reduction of absorption and increase in reflection. The IPCE measurements showed an increase with thickness for undoped samples and a decrease for 1% W gradient doped samples. These results are in agreement with the EIS measurements, which showed a decrease in electrical resistance in undoped samples with thickness, and an increase in 1% W gradient doped films. This suggests that the doping profile introduced more defects in the material, creating new recombination centers, without enhancing the charge carrier separation.

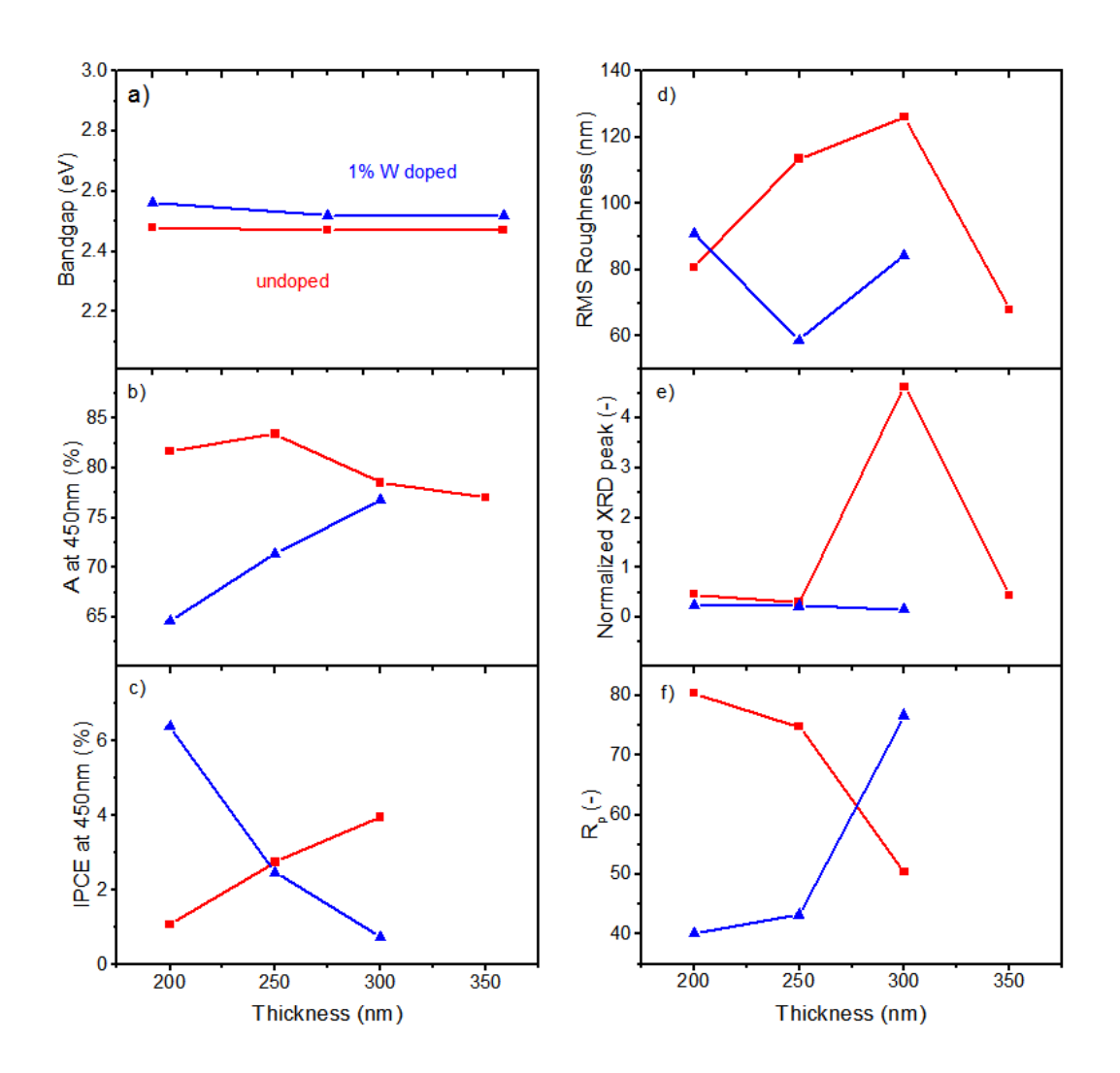


Figure 5.8: Summary and comparison of the measured properties for both 1% W gradient doped (blue) and undoped BiVO₄ samples (red). a) Optical band gap, b) absorption taken at a wavelength of 450 nm, c) IPCE taken at a wavelength of 450 nm, d) RMS roughness, e) XRD monoclinic scheelite peak normalized with the FTO peak, and f) R_p electrical resistance calculated from EIS measurements.

The current density vs. potential (JV) plots of the photodegradation of phenol give more information on the optical, electrical, and catalytic properties of the photoelectrodes. Figure 5.9 shows that the BiVO₄ doped samples had the best JV characteristic, i.e., they demonstrate the lowest onset potential and highest current densities, followed by the BiVO₄ undoped samples and finally the TiO₂ samples. For undoped samples, the current corresponds with

the fraction of monoclinic scheelite in the film, having 200 and 250 nm similar currents while the 300 nm shows a higher current. For the doped samples, the currents are higher due to the superior charge carrier separation strategies. The current density increased from 200 nm to 250 nm due to the enhanced light absorption, and decreased after 250 nm due to the higher recombination caused by the doping, as seen in the EIS measurements. In this case, the crystalline structure does not play a big role because the fraction of monoclinic scheelite in all 1% W gradient doped samples was similar, as shown by the XRD measurements. However, a higher current density does not automatically translate in an improvement of the phenol degradation characteristics, and the actual degradation achieved must be measured. To perform degradation experiments, the optimum applied voltage was determined by using the undoped 300 nm BiVO₄ sample and by determining the highest kinetics of the phenol degradation reaction. Figure 5.10 shows the effect of the applied potential E on the firstorder degradation rate constant k of phenol using the 300 nm BiVO₄ electrode after solar irradiation for four hours. The experiments were conducted by applying electrical biases of 0, 0.2, 0.4, 0.6, 0.8, 1, and 1.2 V (vs. Ag/AgCl, KCl saturated). The applied potential causes an increase in the charge carrier separation. The rate constants of the phenol degradation with different constant potentials, k, were calculated through the linear relationship between $\ln([C_6H_6O]/[C_6H_6O])$ and time. Figure 5.10b) shows that when the applied bias potential was low (1.0 V vs. Ag/AgCl), the degradation rate constant increased with the applied potential. A further increase in the applied potential beyond 1 V vs. Ag/AgCl led to a decrease in the first-order degradation rate constant, possibly due to competing reactions such as water splitting. The data showed that at the potential of 1 V vs. Ag/AgCl, the highest constant rate of phenol degradation was obtained. Therefore, this potential was used in further degradation experiments. When the phenol degradation is measured at 1 V vs. Ag/AgCl at different thicknesses, undoped samples (Figure 5.10c)) showed the maximum performance at 300 nm, after which the fraction of monoclinic scheelite decreased, affecting the phenol degradation. Increasing the thickness of the doped samples (Figure 5.10d)) improved the performance, which is in agreement with IPCE. However, the differences between 250 and 300 nm were small, suggesting that there is a saturation point after which a thicker film does not improve the phenol degradation any more. The main reason for this improvement with thickness is the enhanced light absorption and conversion efficiency. EIS measurements showed a higher resistance for the thicker films in the 1% W gradient doped case, which is not reflected in the phenol degradation characteristic, suggesting that the electrical properties are not the limiting factor in this case. The observed optimal thickness was 300 nm, both for doped and

undoped samples, which balances the trade-off between good optical properties with good electrical properties. The results suggest that the monoclinic scheelite crystal structure could be the preferred one for degradation, since it shows better optical, electrical and catalytic properties both on the surface and in the bulk of the material. For the photodegradation experiments pure photobleaching was excluded as previous work on photoluminescence (PL) and use of terephthalic acid (TA) has shown the qualitative determination of OH generated during the experiments at the surface of the catalyst. [168]

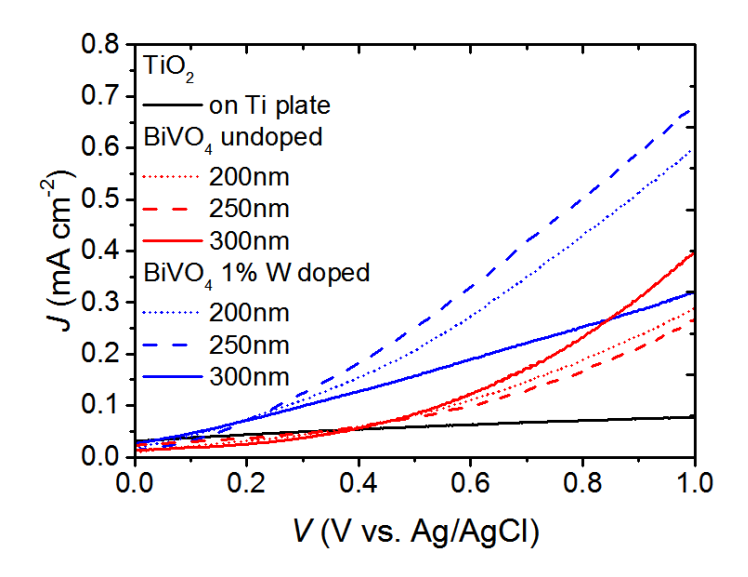


Figure 5.9: JV characteristics for the doped, undoped $BiVO_4$ and TiO_2 samples.

The suitability of BiVO₄ as a photoanode for water treatment and the effect of doping in the material can be further determined by comparing the best thickness of 300 nm for both undoped and 1% W gradient doped BiVO₄, and the performance of TiO₂/Ti composite. When comparing BiVO₄ and TiO₂, Figure 5.10e) and f) confirm that BiVO₄ was more suited for phenol removal from the solution by using solar light. The optimal BiVO₄, 300 nm of undoped film, was able to reduce the phenol concentration, having 30 % of the initial concentration remaining after four hours, while the TiO₂/Ti composite electrode was only able to reduce the concentration up to 56 % of the original value during the same time span. The 1% W gradient doping appeared not to improve the performance compared to undoped BiVO₄. The fitting for both 1% W gradient doped and undoped BiVO₄ was obtained with a first order reaction, with R₂ values of 0.96 and 0.98, respectively. The reaction rate con-

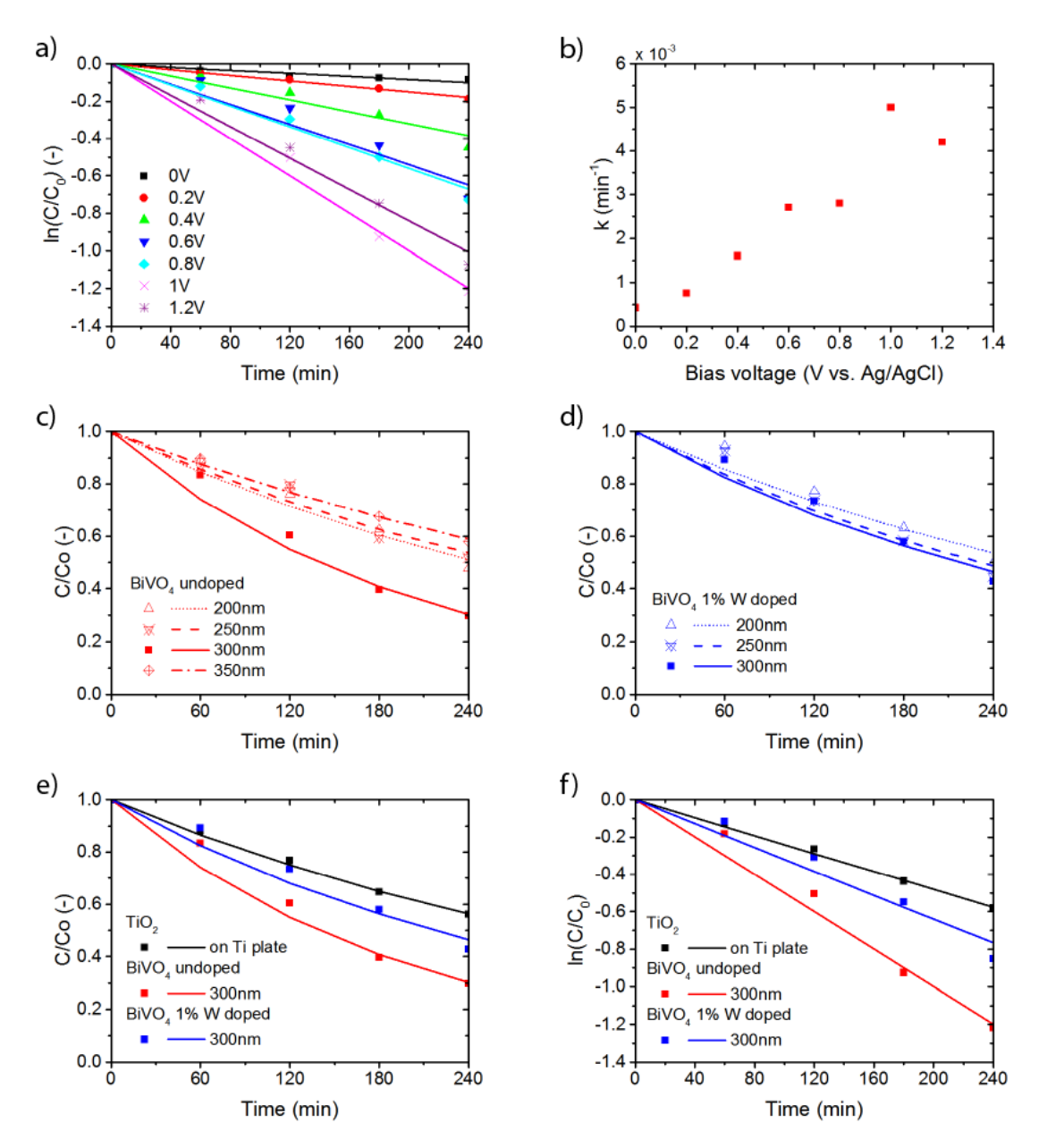


Figure 5.10: a) Kinetics plots and b) corresponding reaction rate for the first-order reaction of phenol degradation for the undoped 300 nm BiVO₄ photoanode at different applied potential. PEC degradation of phenol by using BiVO₄ photoelectrodes for c) undoped BiVO₄, and d) 1% W gradient doped BiVO₄ at different thicknesses. Comparison of the e) PEC degradation of phenol and f) corresponding kinetics plots for first order reaction of phenol degradation rate constant for the 300 nm thick 1% W gradient doped and undoped BiVO₄ with TiO₂/Ti composite.

stants were 0.0032 min^{-1} for the 1% W gradient doped samples, 0.005 min^{-1} for the undoped

samples, and 0.0024 min⁻¹ for the Ti/TiO₂ composite, confirming that the 300 nm undoped BiVO₄ gives the best reaction rates. The lower performance for the gradient doped samples could be due to two effects: the additional defects introduced in the structure by W atoms, which may lead to recombination centers and therefore poor electrical properties; and the surface and structural effects, as seen by the AFM scans and XRD spectra, which lead to less favorable catalysis at lower monoclinic scheelite fractions.

When integrated in a working device, other variables such as scalability or stability are important. In addition, it is preferable that this device can treat different contaminants. Here, these features are considered to assess the suitability of BiVO₄ for this device. For scalability considerations, a UV/ $\rm H_2O_2$ system, considered to be the most efficient AOP, [68] was compared to a PEC device using BiVO₄ at a bias voltage of 1 V vs. Ag/AgCl. (Figure 5.11a)). It must be noted that the first system is based on homogeneous catalysis with only $\rm H_2O_2$ added to the solution and then shined with UV light with an intensity of 60 W/m², while the second system is based on the heterogeneous catalysis happening at the surface of a photoelectrode that is being shined with the visible light of a solar spectrum. A concentration of 0.01 M was taken as a reference for $\rm H_2O_2$ from existing literature. S. Esplugas et al. [169] compared different advanced oxidation processes (AOP) for phenol degradation with the homogeneous catalysis of $\rm UV/H_2O_2$ at concentrations lower than 0.01 M. Other researches have also focused on comparing different systems to the homogeneous catalysis provided by $\rm H_2O_2$ at concentrations in the order of mM. [170–172]

The results in Figure 5.11a) show a slightly better performance of the H_2O_2 compared to the BiVO₄. A kinetic study of the photodegradation of phenol was further performed as a function of the irradiation time, and the data were fitted to a first-order rate model both for UV/H_2O_2 [173] and BiVO₄. The constant rate of the reactions were 0.0078 and 0.0053 min⁻¹ for UV/H_2O_2 and BiVO₄, respectively.

The rate constant was of the same order of magnitude in both cases, indicating that both processes are capable of delivering the same levels of reaction under the conditions described. It must be noted here that H_2O_2 is often used at higher concentrations and the UV lamps might have a higher intensity, achieving higher degradation efficiencies. However, a reactor based on a $BiVO_4$ photoanode can also be designed to maximize pollutant degradation by adapting the ratio between active area and the solution volume. Therefore, these data aim at showing

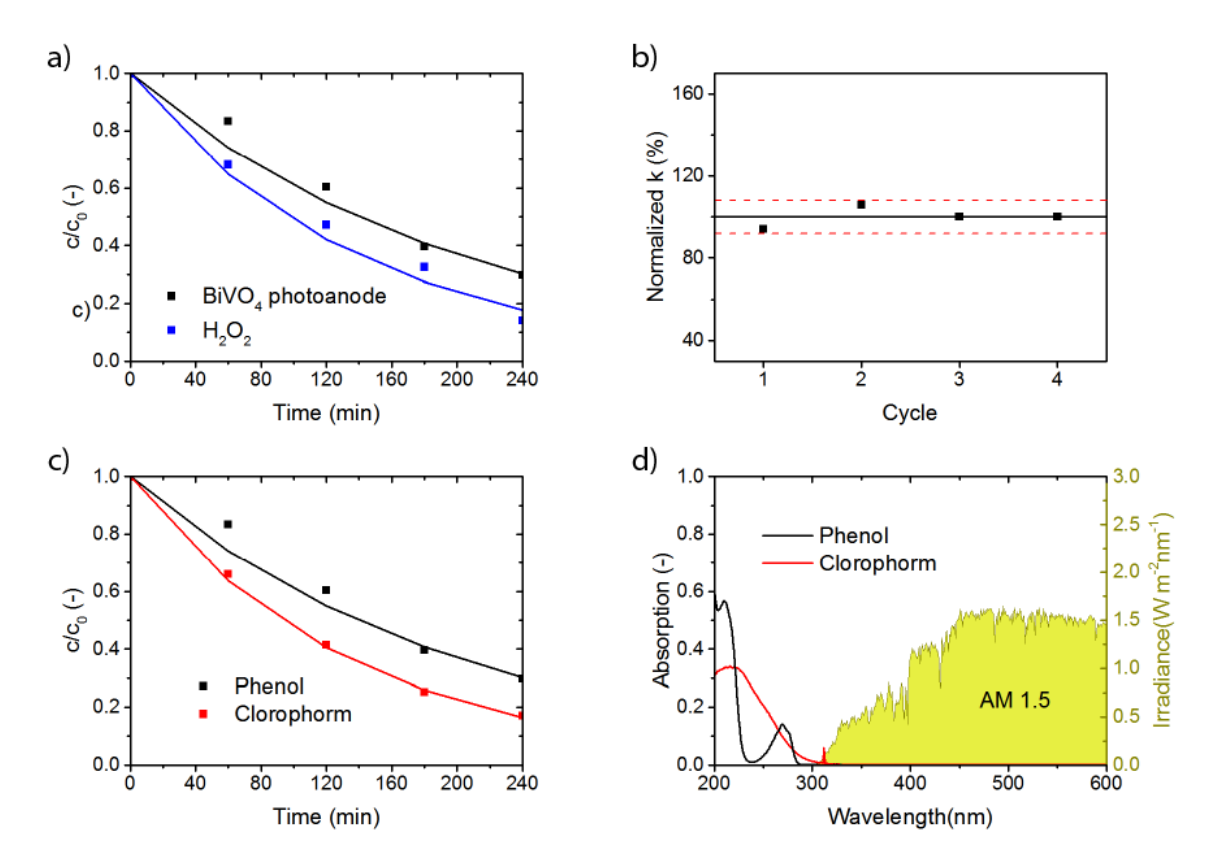


Figure 5.11: a) Phenol degradation using BiVO₄ as photocathode and H₂O₂ as homogeneous catalyst, and corresponding fitting considering first order kinetics, and b) reaction rate constant k normalized by the average reaction rate constant for several consecutive cycles on a BiVO₄ photoanode with applied bias voltage of 1 V (vs. Ag/AgCl, KCl saturated). The percentage represents how much the reaction rate constant has change with respect to the average value (black line). The dotted lines represent the estimated possible error inherent to the measurement equipment and fitting procedures (7.5%). c) Phenol degradation of phenol and chloroform solutions using a BiVO₄ photoanode with an applied bias voltage of 1 V (vs. Ag/AgCl, KCl saturated) and corresponding fitting considering first order kinetics and d) light absorption of the phenol and chloroform solutions used, compared to the solar irradiance (right axis).

that when using a BiVO₄ photoanode, the phenol removal kinetics could reach similar values as the kinetics of the homogeneous catalysis, while avoiding adding a molecule to the solution.

Regarding the stability of the BiVO₄ photoanode, four consecutive degradation cycles were performed on the same sample. The results in Figure 5.11b) show the constant rates of degradation (k), obtained and normalized by dividing by the average k value (black line). The reaction rate constant remained within less than 10 % of the initial value for the 4 consecutive

cycles tested. The possible measurement error of the Spectrophotometer is ± 5 %, [174] and the maximum error of the fitting was ± 2.5 %. Therefore, the added possible error of these measurements is 7.5 %, represented in Figure 5.11b) by the red dashed lines. That shows that the variations observed in the reaction rate constant among the different measurements is within the limits of measurement inaccuracies, and the photoelectrode can be considered stable.

Finally, the flexibility of pollutants that can be treated with BiVO₄ must be taken into consideration for a practical water treatment device. BiVO₄ is a promising material for water treatment of organic pollutants, not only for phenol degradation but also for other organic compounds such as clorophorm or dyes. [30] Thus, to further assess the flexibility of BiVO₄ regarding pollutants, the degradation characteristics of phenol and chloroform were measured, and the results are shown in Figure 5.11c). The reaction rate constants according to first order kinetics can be determined to be 0.0053 min⁻¹ and 0.0075 min⁻¹ for phenol and chloroform, respectively. This shows that BiVO₄ performed even better for chloroform removal than for phenol removal, with a higher reaction rate constant and reaching a final concentration of 17 % of the initial in 4 h. To determine if this effect might be due to the different light absorption of the two pollutants, [175, 176] the absorption was measured, as shown in Figure 5.11d). The absorption peak for phenol is at 200 nm, and the absorption peak for chloroform is found at 215 nm. Since the light spectrum used for these experiments, showed in yellow in Figure 5.11d), contains low amounts of light at wavelengths lower than 300 nm, [177] none of the solutions will absorb a significant part of the solar spectrum and thus the light absorption in the solution can be ruled out as a negligible factor. Therefore, the differences in degradation of pollutants observed in Figure 5.11c) would mainly be caused due to enhanced adsorption of the smaller clorophorm molecules, and the reaction rates on the photoanode surface for chloroform removal. In particular, literature reports that OH radical addition can more easily target C-Cl bonds rather than C-H bonds. [178] Phenol was the used contaminant for further investigation as the "worst case" scenario in this study.

5.3.2 Counter electrode characterization

The cathode material is where the hydrogen evolution reaction occurs, completing the circuit and the redox reaction. It can affect the overall degradation reaction by electro-reduction

of the dissolved oxygen into H₂O₂, electro-reduction of the organic pollutants or direct adsorption of these contaminants in porous cathodes. [179] In order to study the interaction between the electrochemical oxidation and reduction reactions, and to minimize the overpotential related to the counter electrode, different materials and configurations were tested. Ag, Al, Au, Cu, Ni, Pb, Pd, Pt, Ti, Zn, graphite, glassy carbon and activated carbon fiber (ACF) have been proposed in literature as cathode materials in the electrochemical treatment of water containing different organics pollutants. [180, 181] In this work, Cu and graphite were studied due to their relative low cost with respect to other more precious metals, and high removal efficiency. [124, 182] The results are presented in Figure 5.12.

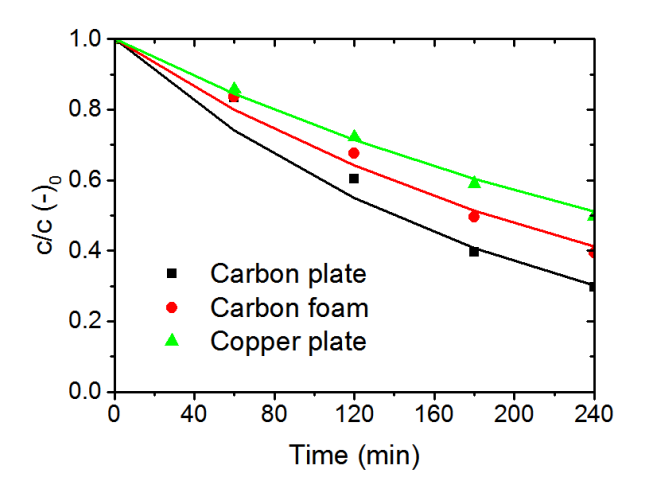


Figure 5.12: Phenol degradation related to the used counter electrode and corresponding fitting considering first order kinetics.

The reaction rate constants obtained by fitting to a first order reaction are 0.0053 min^{-1} for the carbon plate counter electrode, 0.0040 min^{-1} for the carbon foam and 0.0029 min^{-1} for the copper plate. Therefore, carbon seems to be the best material to use as counter electrode. This agrees with literature, in which carbon nanostructures have been widely used to enhance the hydrogen evolution reaction (HER). [183] There are several factors that can play a role on these results. First, the generation of H_2O_2 on carbon electrodes may help the reaction by adding the possibility of homogeneous catalysis. [184] Second, copper electrodes have a tendency to reduce the dissolved oxygen present in the aqueous phenol solution, negatively influencing phenol degradation. [185] Dissolved oxygen acts as an effective electron acceptor to extend the hole's lifetime and to form the oxidizing species of hydroxyl radicals, affecting

the photoactivity of the BiVO₄ film. [186] Finally, despite the fact that carbon foam has a higher surface area, the carbon plate performs better, probably due to the easier mass transport to the surface.

5.3.3 Solar cell and device characterization

BiVO₄ needs a potential applied in order to work at its optimum, since the electrochemical potential of the reaction is higher than the one produced by the BiVO₄ photoanode alone. Previous studies determined that the optimum external applied bias for phenol degradation was 1 V vs. Ag/AgCl. In order to apply the needed potential, an additional solar cell can be added to the system. In this paper, thin-film silicon solar cells were used in combination with the BiVO₄ photoanode due to its flexibility of design regarding the output voltage and current. Using this material, a multijuntion approach can be used, allowing for higher operational voltages than single junctions and better spectral utilization. Using this approach, it is possible to have the Si solar cells produce the applied potential of 1 V at operational conditions, making the system autonomous and removed from an external power supply.

Three main options were explored to use as solar cell: an a-Si:H single junction, an a-Si:H/a-Si:H double junction and an a-Si:H/nc-Si:H double junction. Since the spectrum reaching the solar cells is not AM1.5 but the spectrum transmitted by the BiVO₄ (Figure 5.1b), the absorber thicknesses were adjusted to optimize the output parameters, setting as boundary condition that the a-Si:H top absorber layers would not increase further than 300 nm to avoid strong light-induced degradation. [14] For the a-Si:H/a-Si:H solar cell, the used top and bottom absorber thickness were 150 nm and 400 nm, respectively. The open-circuit voltage achieved with these cells was 1.59 V and the short circuit current under the transmitted spectrum was 2.27 mA/cm². Regarding the a-Si:H/nc-Si:H cell, the bottom cell absorber thickness was fixed at 2000 nm, and the top cell absorber thickness was optimized at 300 nm. The short circuit current under the transmitted spectrum in that case was 3.40 mA/cm² and the open circuit voltage was 1.27 V. Finally, the single junction a-Si:H cell of 300 nm was chosen, which had a short circuit current under transmitted spectrum of 4.85 mA/cm² and an open circuit voltage of 0.83 V. Figure 5.13a) shows the different JV characteristics of the solar cells with optimum thicknesses, and Figure 5.13b) shows the EQE measurements. It can be noticed from the EQE measurements that, even there is still room for improvement,

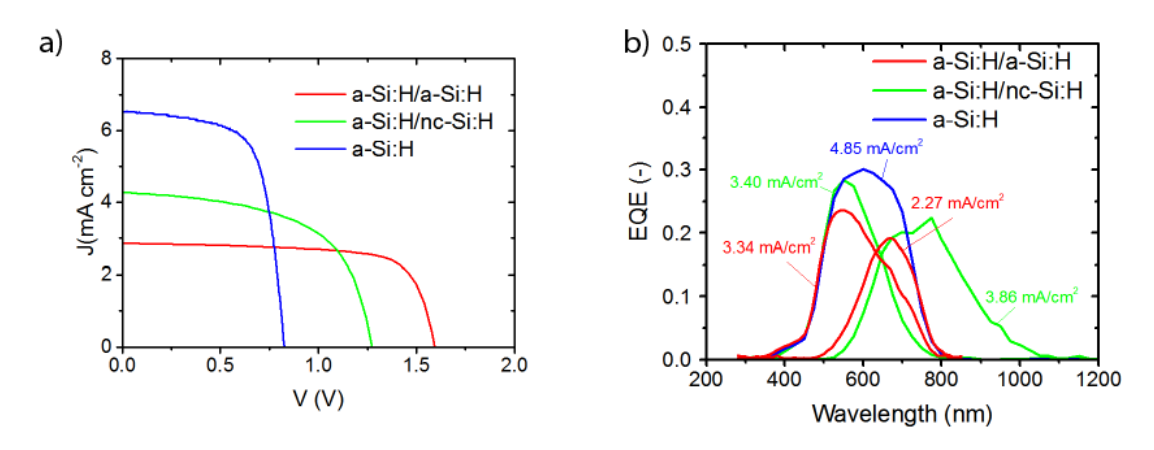


Figure 5.13: a) JV characteristics and b) EQE measured with the $BiVO_4$ transmitted spectrum of the different cells. The corresponding short circuit currents extracted from the EQE are shown in the graph in the corresponding color.

there is good current matching of the tandem junction cells.

The BiVO₄ photoanode was combined with the optimized solar cells of each technology presented, obtaining the phenol degradation curves displayed in Figure 5.14. All the curves were measured including an Ag/AgCl KCl saturated reference electrode for better comparison with the case at bias voltage of 1V vs. Ag/AgCl. Note that the cell area used was 1 cm², maintaining the solution volume constant. The smaller area was chosen to avoid the conductivity limitations of the front TCO layer of the solar cells. The BiVO₄ active area was also 1 cm² to match that of the solar cell. However, it must be noted that because of the difference in volume to area ratio, the final degradation will be smaller.

These degradation characteristics could not be satisfactorily fitted to an order zero, first order or second order kinetics, suggesting that the interaction of all parameters is more complex than these relatively simple kinetics models. However, the general trends of degradation can be analyzed. It can be seen that with an a-Si:H single junction and a-Si:H/nc-Si:H double junction solar cells, combined with the BiVO₄ and no extra voltage applied, a better degradation was reached in comparison to the case of a BiVO₄ photoanode by itself with an applied bias voltage of 1 V vs. Ag/AgCl. The best cell, the a-Si:H/nc-Si:H double junction, which was able to degrade 15 % of the phenol present after 4 hours of degradation. Opposed to it, the BiVO₄ photoanode with 1 V vs. Ag/AgCl applied was only able to degrade 10 % of the

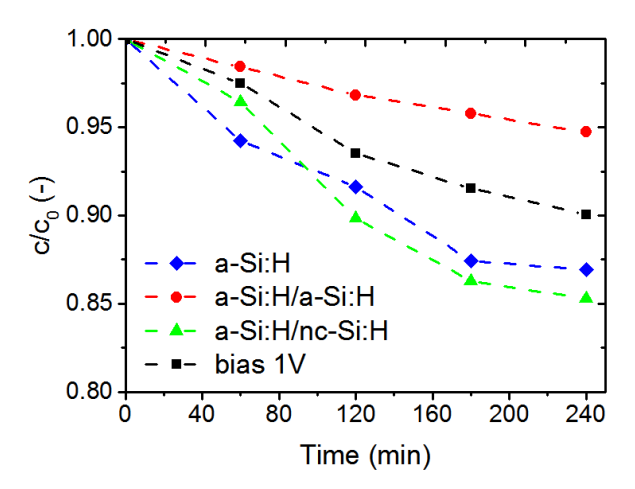


Figure 5.14: Phenol degradation of the BiVO₄ photoanode with time when the optimum 1 V (vs. Ag/AgCl, KCl saturated) potential is applied (black curve), and when it is combined with the different solar cells. The low absolute phenol removal of this case is caused by the big difference between photoanode area and solution volume

phenol present. The improvement given by the solar cell could be because the solar cell acts a current source rather than a voltage source, providing more charge carriers to the solution, positively influencing phenol removal. [187] The current will be adapted to the optimum current case, partly removing the limitation of charge carrier supply to the active surface and increasing the phenol degradation. The lower performance observed for the combination with an a-Si:H/a-Si:H double junction cell can be due to the fact that this cell provides a higher voltage, favoring the water splitting reaction and therefore lowering the performance regarding phenol degradation.

Once the best design for the device has been analyzed, an energy balance was performed to be able to compare it to different systems currently used or studied. [188] This analysis takes into account all the energy inputs to the system, including light and electrical power. The energy necessary to remove 1 mg of phenol E is defined as

$$E = (P_{in} + V_{bias}J_{photo})A/m_{removed}$$
(5.2)

where P_{in} is the light power input in W/m², V_{bias} is the applied bias voltage in V, J_{photo} is the photocurrent density produced in the material in A/m², A is the active area of the system in m², and $m_{removed}$ is the total phenol mass removed from the solution in mg.

The conditions of each analyzed system, together with the energy needed per mg removed calculated using Equation 5.2, are displayed in Table 5.1. The systems compared are the $BiVO_4$ photoanode with and without the solar cell, a TiO_2/Ti composite illuminated by the solar spectrum, and a TiO_2 based photoanode illuminated by UV light. [188]

Table 5.1: Energy balance results for different configurations

Material	Light	Bias voltage (V)	$E \text{ (Wh mg}^{-1})$
TiO_2 [188]	$UV(125 \text{ W/m}^2)$	0	1.83
${ m TiO_2}$	$AM1.5(1000 \text{ W/m}^2)$	1	4.21
${ m BiVO_4}$	$AM1.5(1000 \text{ W/m}^2)$	1	1.15
${ m BiVO_4}$	$AM1.5(1000 \text{ W/m}^2)$	Solar cell (0 V)	0.79

The differences between the UV/TiO_2 system [182] and the TiO_2/Ti plate system are mainly due to the different energies of the light sources, stressing the fact that if UV light is used, the TiO_2 photoelectrode performance is better than with AM1.5.

The BiVO₄ photoanode performed better than TiO_2 in all cases, due to the improved phenol degradation characteristic. The use of BiVO₄ alone instead of TiO_2 with AM1.5 reduced the energy input needed per mg treated by more than 70 %. When the solar cell was introduced, the situation was further improved by reducing the energy needed to 0.79 Wh per mg of degraded phenol. It is important to note that most of the input energy in the AM1.5 cases would be coming directly from the sun and not from an external source of energy, like in the case of the TiO_2 with UV light.

The reduction of the energy needed with the designed device would translate in a smaller, more compact equipment in a practical device, potentially reducing the costs of materials and installation. That would make the system more cost-effective. In addition, an autonomous system from external power sources would allow installation not only in main urban areas but also in remote rural places with no access to electricity.

5.4 Conclusions

BiVO₄ has been proposed as a viable option for photocatalytic oxidation using solar light, as opposed to the commonly used TiO₂. The material studies have shown that BiVO₄, with a band gap of 2.5 eV, is a good absorber for solar light compared to TiO₂. The BiVO₄ thickness had an effect on the optical properties due to enhanced absorption, but also suggested a phase change between 250 and 300 nm thick films. This change in phase and surface structure was confirmed by AFM and XRD measurements. BiVO₄ also showed a better phenol degradation performance compared to TiO₂, confirming that the enhanced light absorption, surface properties and electrical properties translates in an increase in phenol degradation. Doping of the BiVO₄ with tungsten; however, did not improve the phenol degradation performance, suggesting that charge carrier separation is not a limiting factor in this system. The best performance was achieved by an undoped BiVO₄ film of 300 nm, reducing the phenol concentration in solution to 30.0 % of the initial concentration in four hours.

A photo-oxidation device based on earth-abundant materials and solar illumination was also successfully demonstrated based on BiVO₄. It consists of a BiVO₄ photoanode connected to a solar cell and a counter electrode to complete the reaction. BiVO₄ was chosen as a suitable and stable material to use as a photoanode for photochemical degradation not only for phenol but also chloroform. The best material for the counter electrode was a flat carbon plate. A thin-film silicon solar cell was designed to operate under the transmitted spectrum of the photoanode, and to produce the best current and voltage at the operational point for water treatment, finding the a-Si:H/nc-Si:H tandem solar cell to give the best results. This bias-free device can provide an efficient way to remove organic pollutants from water, reducing the costs and the greenhouse gas emissions. In addition, it could be applied as a stand-alone device, which could be independently installed even in remote areas without a stable electricity supply.

6

Photo-oxidation of organic pollutants using a photovoltaic device

This chapter is based on the following publication:

P. Perez-Rodriguez, C. Maqueira Gonzalez, Y. Benanni, L.C. Rietveld, M. Zeman, A.H.M. Smets. Photo-oxidation of organic pollutants usng a silicon-based photovoltaic device. *Under review*.

6.1 Introduction

Clean water scarcity is expected to be one of the main challenges for society in the near future [189], with about a billion people with limited access to clean water [123]. The heavy industrialization and urbanization currently taking place are expected to increase the problem, polluting main water sources with hazardous effluents [190]. Some of the most common contaminants are organic pollutants such as pesticides, pharmaceuticals, phenol compounds, chloroform or dyes [124, 125]. Several methods to remove organic contaminants include biological, physical and chemical treatments. However, these methods hardly remove the pollutants to the low concentrations needed [126, 127]. Many advanced water treatment processes such as advanced oxidation processes (AOPs) are able to achieve low concentrations of contaminants, but generally consume high amounts of energy [126, 191]. Thus, the solution to tackle the polluted water problem should also take into account the device energy needs.

Electrochemical oxidation is a method with the potential to remove toxic organic compounds, ecologically hazardous cyanides and other residual compounds even at low concentrations [51]. This method uses an electrical current provided by an external source to degrade the pollutants into less complex compounds such as CO_2 , which are easier to remove by a post-treatment step [192]. Moreover, it can be coupled with devices based on earth-abundant materials that can cheaply provide the needed electrical energy to drive the process, eliminating the energy consumption impact of the whole device. [193], combining the advantages of low pollutant concentrations and low energy costs.

Previous work has demonstrated devices that can successfully degrade several organic contaminants using solar energy and earth abundant materials using compounds such as bismuth based compounds [64, 65], SnO_2 [61], WO_3 [63] and TiO_2 [59]. However, these materials are not able to effectively degrade organic pollutants using only solar energy. To tackle this challenge, previous research combined a $BiVO_4$ photoelectrode with a thin film (TF) silicon solar cell and a graphite counter electrode [193]. The demonstrator device was able to effectively degrade phenol and clorophorm, reducing the energy use from 4.21 Wh/mg for the traditional TiO_2 to 0.79 Wh/mg for the bias-free device. Nevertheless, this device is constrained by the interaction between the $BiVO_4$ and solar cell, since the solar spectrum needs to be distributed among the different junctions, and the produced current density would be limited by the photoanode. This paper aims at further decoupling these two subsystems by designing

a solar cell based on earth abundant materials that can provide the necessary energy for a fully electrochemical system, without the inclusion of a photoelectrode. This configuration relaxes the requirements for the solar device, allowing for more flexibility of design. Moreover, by designing a direct solar water treatment system, no converter or inverter is needed, reducing the complexity of the system and the potential costs.

The materials available regarding the photovoltaic (PV) cell implementation include III-V technologies, perovskites, organics, crystalline silicon (c-Si), TF amorphous and nanocrystalline silicon (a-Si:H and nc-Si:H), and copper indium gallium selenide (CIGS) [7, 8]. The technological choice depends on the design requirements of the electrochemical components. The voltage characteristics of the used electrodes must be taken into account as one of the main variables affecting the solar cell choice. However, unlike other configurations such as that of an external power source, solar cells are also current sources, and thus the current-voltage interaction would play an important role on the final performance. Thin film silicon and crystalline silicon technologies have been chosen as the preferred PV technologies due to their relatively low cost, availability and design flexibility. Here, several different PV technologies and configurations have been studied, including a-Si:H, nc-Si:H, and silicon heterojunction (SHJ) solar cells. In addition, either monolithic multijunction solar cells (Figure 6.1a), or wired series-connected solar cells (Figure 6.1b) may be required to fulfill the voltage requirements of the oxidation process [146–148].

By decoupling the two elements of charge carrier generation and collection, and the redox reactions, each element can be better optimized. Thus, the resulting device would have the potential to reduce the costs of advanced water treatment processes by using free solar energy and earth-abundant materials, and to have the additional advantage of being electrically autonomous from any external power source. However, to achieve such efficient devices, the interaction between the current and voltage produced by the solar cell and the electrochemical system must be better understood and compared with the more common case of an independent power source.

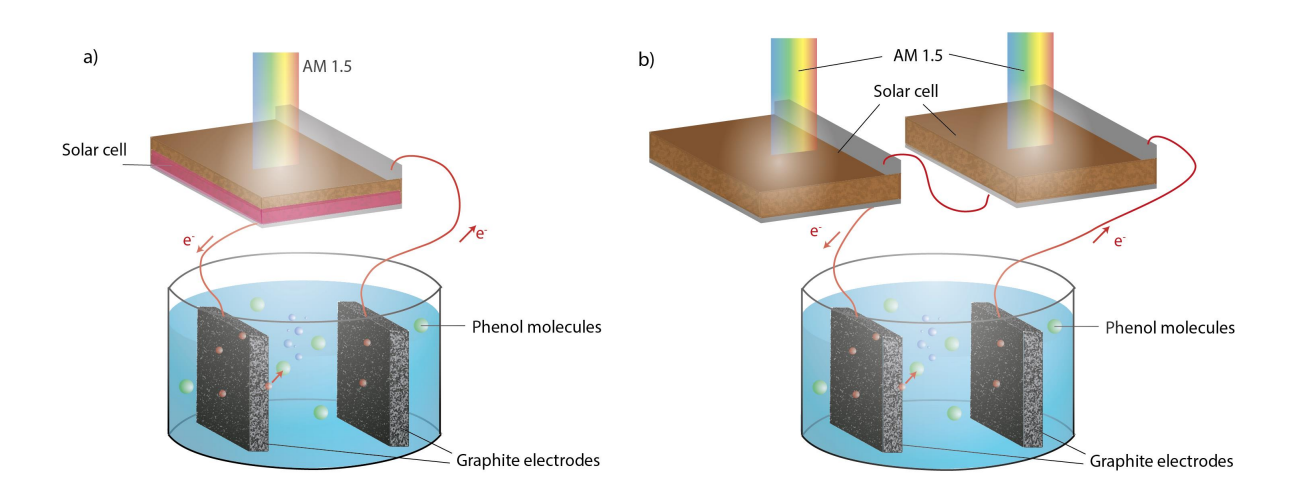


Figure 6.1: Schematic of a stand-alone device configuration combining an electrochemical system and a) an individual solar cell, possibly multijunction, or b) several solar cells connected in series, which can be either single or multijunction.

6.2 Materials and methods

Solar cell fabrication. Both TF solar cells were deposited by radio frequency plasma enhanced chemical vapour deposition (RF-PECVD) using a cluster tool from Elettrorava. The a-Si:H and a-Si:H/a-Si:H solar cells were deposited on textured Asahi UV substrates, which use Fluor doped tin oxide (FTO) as transparent conductive oxide (TCO). The a-Si:H/nc-Si:H solar cells were deposited in wet etched textured corning glass with aluminium-doped zinc oxide (AZO) as TCO. The texturing of the glass used for the a-Si:H/nc-Si:H cell is described elsewhere [144]. Nanocrystalline silicon oxide (nc-SiO_x:H) has been used as p-layer (boron doped) and n-layer (phosphorous doped). The deposition rates of a-Si:H and nc-Si:H were 0.16 and 0.71 nm/s, respectively. The SHJ solar cells were deposited on a flat n<111> float zone (FZ) wafer from University Wafers cleaned by subsequent steps of HNO₃ and HF baths. Then, 7 nm of intrinsic a-Si:H were deposited in each side of the wafer, and 7 nm of p-type a-Si:H and 9 nm of n-type a-Si:H were fabricated to complete the structure. Finally, a 100 nm layer of low power and temperature indium doped tin oxide (ITO) was deposited on top of the p-type emitter layer as the front TCO.

The contacts for all the cells have been deposited using electron beam physical vapor deposition (EB-PVD). A 300 nm Al stripe in contact with the TCO has been used as front contact. A stack of 200 nm Ag, 30 nm Cr and 500 nm Al has been used as back reflector and back

contact. The solar cell area for all configurations was 1 cm². Interconnections have been performed by soldering Ag cables to the solar cell contacts.

Solar cell characterization. The external quantum efficiency (EQE) was measured in an in-house setup in TU Delft, the Netherlands, to obtain the amount of charge carriers generated per photon at a given wavelength. The current density – voltage (JV) characteristics of the solar cells have been measured using a Wacom AAA solar simulator using two lamps (Xe and halogen), and an AM 1.5 filter. The short-circuit current density has been corrected with the obtained value from the integration of the EQE weighted with the AM1.5 spectrum.

Photoelectrochemical measurements and sampling. Photoelectrochemical experiments for phenol and dye degradation were carried out on a setup consisting of a cylindrical quartz glass reactor with an effective vessel volume of 200 mL, an Atlas solar simulator (SUNTEST XXL+) and two graphite electrodes. The electrodes were graphite plates with an area of 16 cm². The initial volume of the working solution was 150 mL of either a phenol solution with initial concentration of 20 mg/L (>99 %, Sigma Aldrich), or a 25 mg/L methylene blue solution (≥99 %, Sigma Aldrich). To eliminate the influence of solution resistance, 0.1 M Na₂SO₄ (>99 %, Merck) was chosen as supporting electrolyte. Demineralized water (RiOs 5 Reverse Osmosis System) was used throughout the experiments for dilution. At the start of each experiment, the graphite electrodes were kept in the stirred solution in the dark for one hour for the adsorption at the electrode surface to reach equilibrium [168]. The pH of the solution was kept constant at 7.2 and was measured before the experiment, using a Sentix 81 pH meter. The temperature was controlled at 25 ± 1 °C by recirculating cooling water in a water bath equipped with cooler Julabo, FL300. During the experiments, the reactor was closed by a UV permeable quartz lid to prevent evaporation of phenol. The electrode potential and working current were controlled with a potentiostat-galvanostat system (Autolab PGSTAT128N with a BOOSTER10A) controlled by Nova Software.

Samples of 2 mL of either phenol solution or dye solution were collected every hour for further characterization. Phenol reacts with 4-nitroaniline to form a yellow-coloured complex, which is then measured using a UV/Vis spectrophotometer (Hach Lange DR 3900, cuvette tests LCK 345 with a measuring range of 0.05-5.00 mg/L, 5-50 mg/L and 20-200 mg/L). The possible measurement error of the Spectophotometer is \pm 5% [174]. The methylene blue absorption characteristic were also measured using the UV/Vis spectrophotometer, and the

characteristic peak at a wavelength of 650 nm was taken as an indication of the methylene blue concentration [194].

The chemical oxygen demand (COD) describes the oxygen required to oxidize all soluble and particle organics. It was measured to determine how much of the pollutants was completely removed and how much remained in the solution as derivatives of the original molecules. The COD measurements were performed by using a mix containing a strong oxidizing agent (Cr₂O₇²⁻), a small amount of silver for the more resilient organics, and mercury to avoid possible interaction with chloride ions. After adding the oxidizing agent, the samples were digested for 2 h and 148 °C, after which the amount of consumed oxidizing agent was determined. By subtracting the initial and final concentrations of oxidizing agent present, the consumed oxidizing agent was determined.

6.3 Results and Discussion

A device consisting of a solar cell and an electrochemical system for the degradation of organic pollutants in water was studied. In order to understand and improve the performance of the proposed system, the electrochemistry of the graphite plate system was analyzed first. Then, different solar cell configurations were designed based on the identified electrochemical characteristics. The solar cells were separately characterized and then combined with the electrochemical system. The potential of this stand-alone device to effectively remove organic contaminants was then determined.

The electrochemical system, in this context, refers to the part of the system comprised by the two electrodes and the electrolyte. The interaction between the electrochemical oxidation and reduction reactions is crucial to characterize the system, and it can help to minimize the overpotential related to the electrodes. Different materials such as Ag, Al, Au, Cu, Ni, Pb, Pd, Pt, Ti, Zn, graphite, glassy carbon and activated carbon fiber (ACF) have been proposed in literature as cathode materials in the electrochemical treatment of water containing different organics pollutants [180, 181]. In this work, two graphite plates were studied due to their relative low cost with respect to other more precious metals, and high removal efficiency [124, 182]. Figure 6.2a) shows the JV characteristic of the graphite-graphite electrochemical system. The system shows a rather high hysteresis loop between -1 and 2.5 V. This effect could

be related to the capacitance created between the two electrodes due to the charge transfer barriers between the electrodes and the electrolyte. In addition, no characteristic peak could be observed for the formation of any intermediate compound. Previous research also has related the absence of this peak in graphite electrodes to the fouling effect of phenol, which passivates the electrode [195, 196]. Thus, to determine if the phenol reaction occurs, Figure 6.2a) also compares the JV characteristic of the system with and without phenol present in the solution. When phenol was introduced, the current at positive voltages increased, which confirms the phenol degradation at voltage ranges between 1 and 2.5 V. Moreover, a lower hysteresis can be observed when phenol was present, indicating that the charges can be more easily transferred to the electrolyte. To further optimize the voltage response of the

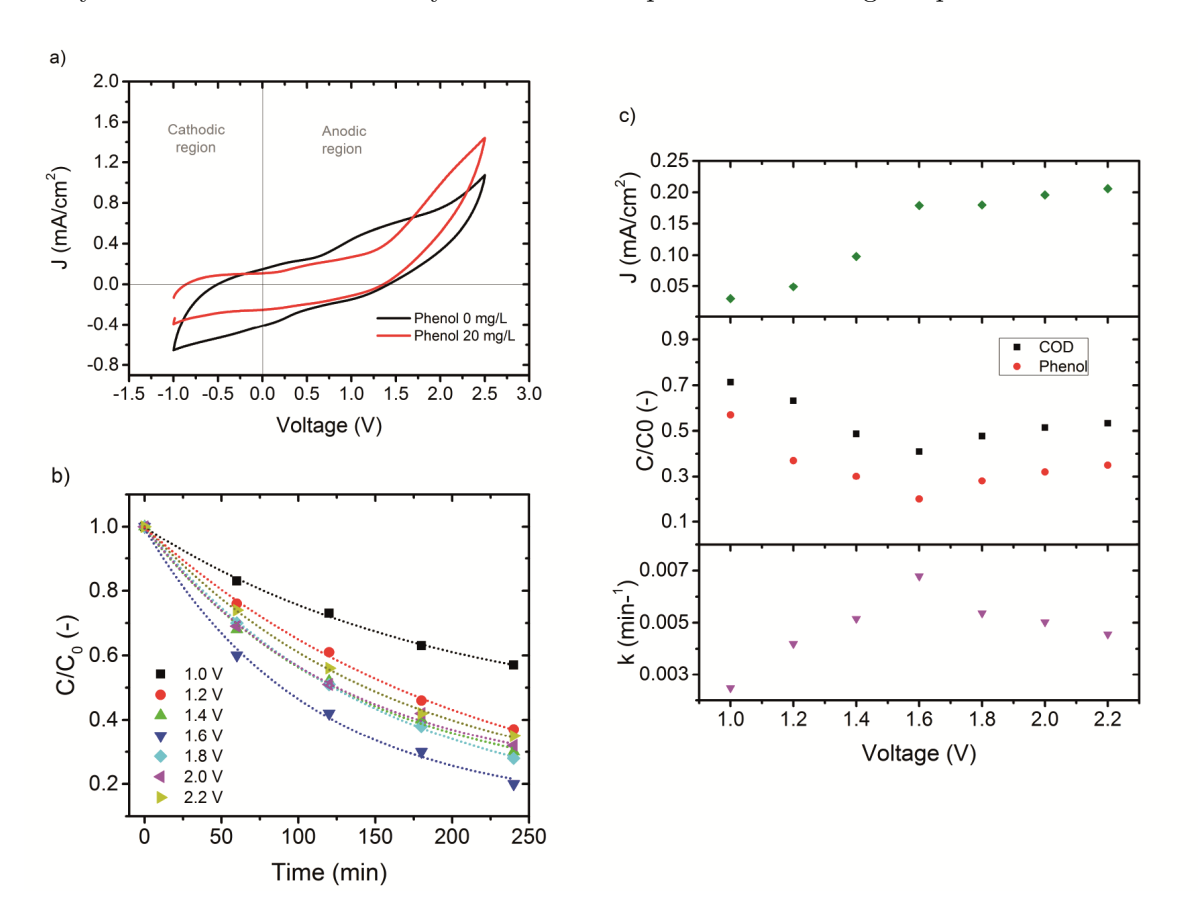


Figure 6.2: Characteristics of a graphene/graphene electrochemical system a) JV characteristics, a) phenol degradation at different applied potentials, and c) the corresponding first order reaction constant; the current density measured flowing through the system at each voltage and the final concentration and COD in the sample after four hours of degradation at different voltages

system, degradation experiments were conducted using different potentiostat applied voltages

ranging from 1 to 2.2 V. The results are shown in Figure 6.2b). The concentration profiles observed correspond to a first order reaction, allowing to calculate the reaction rate constant, as plotted in Figure 6.2c). The reaction rate constant shows a clear maximum at 1.6 V, which also coincides with the minimum concentration and COD in the solution after 4 h treatment. When operating below this voltage of 1.6 V, the charge carrier density was not enough to produce many radicals and degrade the phenol molecules. This is indicated by the trends in the current density, which steadily increased with voltage up to 1.6 V. After this voltage, the current density stabilized, indicating that the charge carrier generation and separation inside the graphite were not the limiting factors anymore. The degradation efficiency decreased after this point due to other competing reactions such as water splitting. Compared to other similar systems such as TiO_2 based systems, the voltage needed is higher for achieving similar currents due to the photoactivity of TiO_2 . [23] However, in the proposed system, that photoactivity is transferred to the solar cell, avoiding issues associated to light absorption in the solution.

The solar cell designed to be integrated in this device should have an operational voltage around 1.6 V to assure charge carrier separation inside the semiconductor, and at the same time to not surpass the water splitting reaction potential, which would reduce the availability of charges for the phenol degradation reaction. To confirm the suitability of this electrochemical system for other contaminants, the degradation of methylene blue was also tested. Qualitatively, a clear change in the color of the solution can be seen in Figure 6.3a). Quantitatively, the absorbance of the solution was measured to evaluate the methylene blue removal. In particular, the peak at a wavelength of 650 nm was used to evaluate the dye removal due to its more persistent nature. [197] A reduction of the methylene blue concentration similar to previous works was achieved [198], achieving almost complete removal after 4 h of degradation, was observed, confirming the suitability of these systems for a variety of organic contaminants. Moreover, this system would be able to outperform the traditional TiO₂ photoelectrodes [199], since the light absorption in the methylene blue does not affect the graphite/graphite performance, unlike for TiO₂.

In order to achieve the desired potential of 1.6 V, a solar device was coupled to the electrochemical system. TF silicon solar cells and silicon heterojunction (SHJ) cells were used due to their flexibility of design, their low costs and their high performance. When using TF silicon, a multijunction approach can be used, allowing for higher operational voltages than

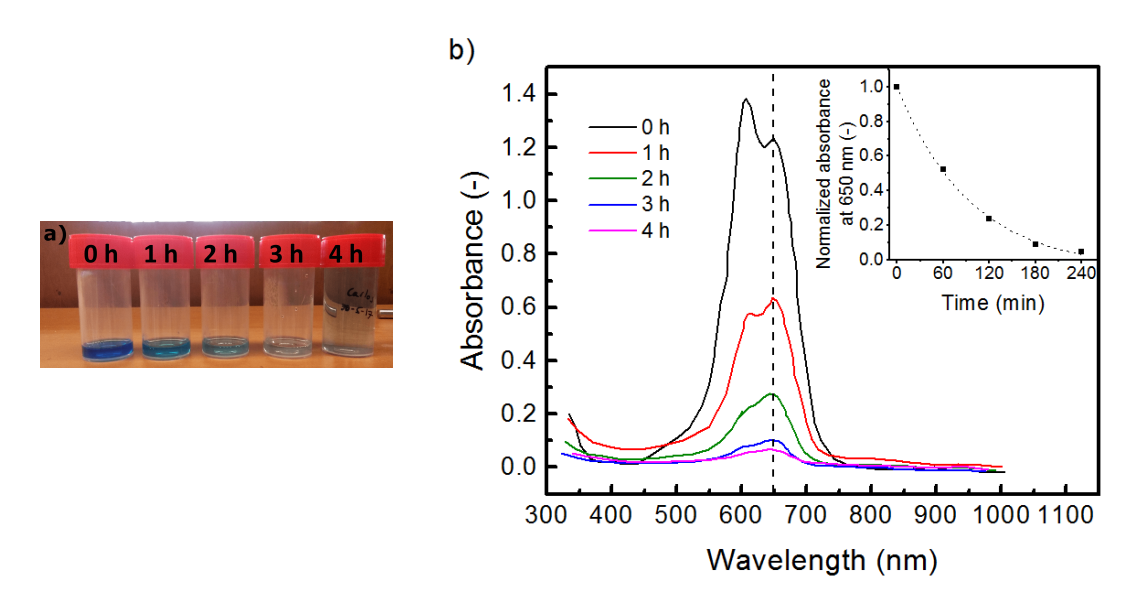


Figure 6.3: Degradation of methylene blue with an applied voltage of 1.6 V. a) Qualitative visual change in the solution color and b) absorbance peak change with time

single junctions and better spectral utilization. The absorber thicknesses were adjusted to optimize the output parameters, setting as boundary condition that the a-Si:H top absorber layers would not increase further than 300 nm to avoid strong light-induced degradation [14]. In addition, flat silicon heterojunction (SHJ) solar cells are also available. The main external parameters obtained for each of the available cells are summarized in Table 6.1.

Some of these cells produced a voltage close to the optimum operational voltage previously determined, namely a-Si:H/nc-Si:H and a-Si:H/a-Si:H cells. Thus, these cells could be tested as a single multijunction device. However, since most of the used solar cells have operational

Table 6.1: External parameters of the selected thin film solar cells at standard test conditions (STC) conditions

Solar cell type	$V_{OC}(V)$	$J_{SC} (mA/cm^2)$	FF (-)	Eff (%).
a-Si:H	0.85	18.7	0.62	9.9
$a ext{-}Si:H/nc ext{-}Si:H$	1.36	12.9	0.60	10.5
a-Si: H/a -Si: H	1.67	8.88	0.61	9.04
SHJ	0.68	35.00	0.54	12.8

voltages lower than the optimum 1.6 V, several cells must be connected in series. Here, two a-Si:H, two SHJ, two a-Si:H/nc-Si:H and two a-Si:H/a-Si:H were connected in series to achieve higher voltages. Note that, even though the performance of these cells might be superior, the solar cell area is doubled related to the individual cells. Thus, a direct cost-performance comparison between the two configurations is not possible.

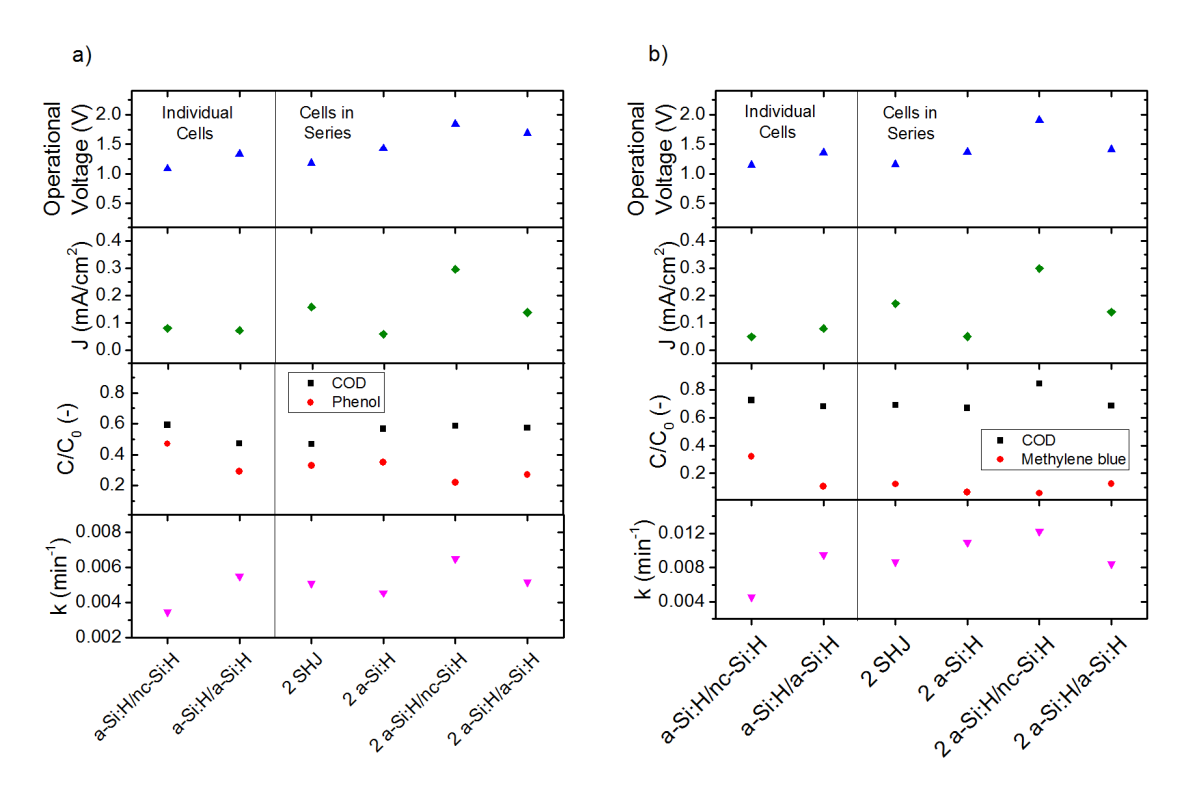


Figure 6.4: a) Phenol and b) methylene blue degradation characteristics when using different solar cells. The current densities reported are based on the electrode area of 16 cm²

To determine the suitability of these strategies for water treatment, the solar cells were coupled to the electrochemical system previously described, resulting in the phenol and methylene blue degradation characteristics shown in Figure 6.4. Looking at the individual cells, it can be seen that with an a-Si:H/a-Si:H double junction solar cell, a better degradation was reached in comparison to the case of a-Si:H/nc-Si:H. The a-Si:H/a-Si:H cells were able to produce a higher operational voltage, injecting charge carriers more efficiently into the solution to drive the phenol degradation reaction [187]. The produced current density remained within the same order of magnitude for the two cells. When adding several of these cells in series, higher operational voltages were achieved, closer to the desired value of 1.6 V. This resulted

in a higher phenol degradation for the case of two a-Si:H/nc-Si:H in series, reducing the phenol concentration by 80 % after 4 hours. In the case of methylene blue, all cells in series achieved similar values to the ones for the individual a-Si:H/a-Si:H cells, reaching low dye concentrations. Overall, connecting several cells in series did not significantly improve the performance, since in most cases the voltage obtained was too high for optimum operation, and the possible mismatches between cells can further lower the performance.

Moreover, even though the system with the two a-Si:H/nc-Si:H cells connected in series showed the best pollutant degradation, it resulted in the highest remaining COD values after 4 h of degradation. The lowest final COD values for phenol correspond to the individual a-Si:H/a-Si:H cell and the two SHJ cells in series. For methylene blue the lowest values were achieved with the individual a-Si:H/a-Si:H cell and the two a-Si:H cells in series. Thus, it seems that after a certain voltage threshold, higher operational voltages can lead to lower COD removal. Overall, considering the achieved pollutant degradation and COD removal, as well as the needed PV area, an a-Si:H/a-Si:H tandem solar cell appeared to be the most viable option, achieving a phenol removal of 70 % (energy use of 0.19 Wh/mg phenol), a methylene blue removal of 90 % (energy use of 0.12 Wh/mg methylene blue), and COD removals of these two pollutants of 55 % and 30 %, respectively. Moreover, compared to the energy use of 0.79 Wh/mg phenol for a BiVO4 photoanode connected to a solar cell [193], decoupling the PV and electrochemical elements seems to result in a more energy efficient system.

When comparing the results of the solar cells (Figure 6.4) to the ones performed by a voltage source (Figure 6.2), some differences can be observed. In the case of solar cells, higher current densities can lead to lower COD, like for the two a-Si:H/nc-Si:H cells connected in series. This suggests that, since solar cells are not only voltage sources but also current sources, the current density must also be taken into account. To better understand this process, the COD concentrations and the final concentration of phenol and methylene blue are plotted as a function of the total power density provided by the solar cell, as depicted in Figure 6.5, calculated as the voltage times the current density of the solar cell under operation. This analysis shows that higher power densities resulted in a higher degradation of the organic molecules but a constant or slight increase in final COD, both for phenol and methylene blue. When the power density is high, the current densities are high at the surface of the electrode, and more contaminant molecules (phenol and methylene blue) are decomposed.

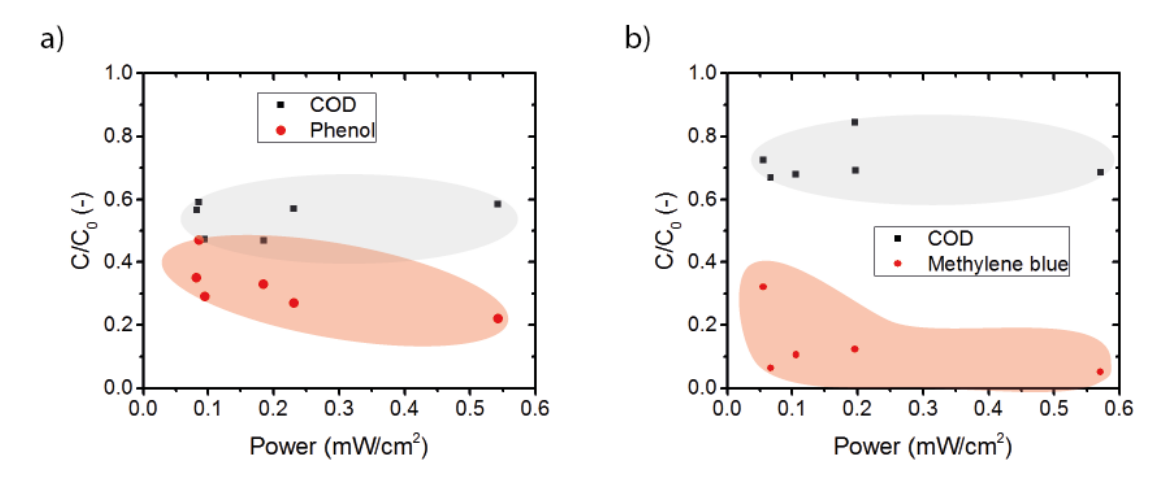


Figure 6.5: Concentration of a) phenol and b) methylene blue, and their respective CODs after 4 h of degradation with respect to the power provided by the different solar cell configurations. The power densities refer to the areas of the electrodes, which are 16 cm² per electrode.

However, the COD does not necessarily follow the same trend because it might need different voltage, current levels, or surface treatments, which would transfer these additional charge carriers to other side reactions such as the creation of polymers that might cause fouling. [200]

6.4 Conclusions

A photo-oxidation device based on earth abundant materials and solar illumination was successfully demonstrated. It consists of a graphite/graphite electrochemical system connected to a solar cell that provides the necessary electrical power. The optimum voltage for the graphite/graphite system was determined to be 1.6 V, at which it can efficiently degrade both phenol and methylene blue. A thin-film silicon solar cell was designed to operate at a voltage as close to this value as possible. An a-Si:H/a-Si:H tandem solar cell was found to give the best results, with a phenol removal of 70 % of the original concentration after four hours of treatment. Connecting several of these cells in series did not significantly improve the performance, since the voltage obtained was too high for optimum operation and the mismatches between cells further lowered the performance. Moreover, normalizing if the results by the active PV area, using a single multijunction of a-Si:H/a-Si:H was the most suitable solution. In conclusion, an autonomous device consisting of an a-Si:H/a-Si:H solar cell combined to a graphite/graphite electrochemical system can provide an efficient way to

remove organic pollutants from water, potentially reducing the costs and the greenhouse gas emissions of a water treatment facility.

6 Photo-oxidation of organic pollutants using a photovoltaic device

7

Conclusions and Outlook

In this thesis, it is studied how PV and PEC devices interact with an electrolyte for both solar water splitting and solar water treatment of organic pollutants. In particular, it focuses on the semiconductor/electrolyte interface and the semiconductor device design. From this research, some solutions to tackle the challenges encountered when designing a PEC device can be outlined. Based on the developed designs, the feasibility of PEC devices for water splitting and water treatment can be evaluated in a broader context.

7.1 Conclusions

The main areas of interest addressed in this thesis were already outlined in Figure 1.13. Accordingly, the design challenges in these areas of interest were phrased into the research questions stated in Section 1.4 as follows:

Solar water splitting

• What is the role of the semiconductor/electrolyte interface in terms of charge carrier separation and collection, and band alignment? (Design challenges: charge carrier collection and utilization)

- What are the design parameters of a PV or PEC device that facilitate the necessary voltage at the operational point for water splitting? (Design challenges: charge carrier separation and collection, spectral utilization, enthalpy of the reaction)
- What strategies can be considered in terms of light management and optimum device architecture to achieve highly efficient solar water splitting? (Design challenges: spectral utilization, enthalpy of the reaction light management)

Solar water treatment

- What is the role of the semiconductor/electrolyte interface in terms of charge carrier separation and catalytic activity? (Design challenges: charge carrier collection and utilization, spectral utilization)
- What is the interplay between operational voltage and current applied to the (P)EC device? (Design challenges: charge carrier collection and utilization, spectral utilization, enthalpy of the reaction)
- What is the optimum device architecture to achieve efficient solar water treatment? (Design challenges: charge carrier collection and utilization, spectral utilization, enthalpy of the reaction)

Based on the presented research, these questions are answered in the following sections.

7.1.1 Solar water splitting

Regarding the solar water splitting reaction, the conclusions reached are as follows:

• The semiconductor/electrolyte interface is crucial for charge carrier separation and collection. Therefore, this interface in PEC devices has been systematically studied during this thesis. According to the results of this research, the most important design parameters of PEC devices are the electric field and selective contacts, and the band alignment of the semiconductor with the hydrogen evolution reaction. In particular, for the a-SiC:H photocathode presented, including a n-type nc-SiO_x:H between the intrinsic a-SiC:H and the electrolyte improves the electric field, and thus the charge carrier separation. This improvement is related to the low activation energy of the n-type nc-SiO_x:H; and the decoupling of the quasi-Fermi level splitting and the energy

level of the reaction in the electrolyte. However, a TiO₂ layer is also necessary at te semiconductor/electrolyte interface to achieve a good band alignment between the semiconductor and electrolyte, facilitating charge carrier injection from the semiconductor to the electrolyte. Therefore, both the PEC and PV expertise are necessary to fabricate a successful solar water splitting device.

- Since an effective electric field seems crucial to solar water splitting devices, a PV+EC approach was taken during this research in order to enhance the charge carrier separation and collection in the semiconductor device. In addition, multijunctions are needed to achieve the water splitting voltages if a direct monolithic PV+EC approach is desired. This thesis proposes a hybrid approach combining thin film silicon and crystalline silicon absorber materials, forming an a-Si:H/nc-Si:H/c-Si triple junction solar cell. This multijunciton cell acomplishes good spectral utilization, good charge carrier separation and high voltage, which can independently drive the water splitting reaction. Moreover, the good fill factor achieved during this thesis ensures high solar-to-hydrogen efficiencies at the operational point. This was achieved by focusing on the TRJ junction design. A good TRJ ensures that there is no energy barrier, achieving a high voltage and fill factor. In this case, the best top TRJ was a bi-layer consisting of n-type a-Si:H and n-type a-SiO_x, which increases the defect density at the interface, enhancing charge carrier recombination. In addition, it also improved intermediate reflection. For the bottom TRJ, a highly doped n-type a-Si:H layer was used as the middle subcell n-layer, achieving better band alignment for charge carrier tunneling and recombination at the interface between the two subcells. The final cell achieved a V_{OC} of 2.03 V, a FF of 0.64 and an efficiency of 10.42 %.
- To further enhance the conversion efficiency of the previously mentioned multijunction solar cell, the next step is to improve the current density of the cell by applying light management techniques. During this thesis, the substrate texture and the thin film absorber materials were modified. However, these steps, especially texturing, can also affect the electrical properties of the cell. In particular, this work showed how the traditional crystalline silicon pyramid textures are too sharp for nc-Si:H growth, creating short-circuits and degrading the electrical performance. On the other hand, absorber tunning can improve the current matching. Using this approach, a solar cell with an efficiency of 10.57 % as PV was achieved. Moreover, the maximum power point closely matches the operational point of this solar cell when connected to a traditional

electrolyzer, achieving a stable STH conversion efficiency of 8.3 %. For further improvements, softer texturing for crystalline silicon must be developed to achieve efficient light management.

7.1.2 Solar water treatment

Regarding the water treatment reaction, the following conclusions were drawn:

- In the case of PEC water treatment devices, this research identified the semiconductor material as the key design parameter for efficient PEC water treatment. By using a BiVO₄ photoanode, this thesis shows that the crystal structure and material properties of the semiconductor affect the catalytic effect for organic pollutant degradation at the semiconductor/electrolyte interface. This would affect the bandgap energy utilization, ensuring that the energy generated at the semiconductor device is used on the target reactions. In particular, for BiVO₄ the monoclinic scheelite is the more favorable crystalline structure for treatment of organic pollutants. Including an internal electric field does not show significant improvement, suggesting that there are other factors limiting the performance, such as the catalytic effect or the charge carrier injection at the semiconductor/electrolyte interface.
- Alternatively to PEC devices, this thesis proposes to apply a PV-EC architecture for water treatment. However, this research shows that, when considering a stand-alone solar system for water treatment, there is no direct translation between current density or voltage, and pollutant degradation and mineralization. The results obtained with a potentiostat as a power source are different from those using a solar cell, especially regarding the level of mineralization of the organic pollutants. The results suggest that these discrepancies are due to the fact that solar cells are current sources as well as voltage sources. Thus, the total power provided to the solution also affects the degradation mechanisms. In particular, the COD degradation tends to be lower at higher powers.
- Since the PV-EC configuration showed promising results regarding organic pollutant degradation, this thesis studies the optimum PV-EC configuration for a stand-alone water treatment device. When using one or two solar cells connected to a graphite/graphite electrolyzer for phenol and methylene blue degradation, the best cell is an a-Si:H/a-Si:H tandem cell. This configuration achieves a phenol removal of 70 % and a methylene blue

removal of 90 % after 4h with respect to the initial pollutant concentration. Moreover, the respective CODs are 55 % and 30 % lower than the initial CODs of the respective solutions. Finally, the energy use was 0.19 Wh/mg of phenol and 0.12 Wh/mg of methylene blue, much lower than the 1.83 Wh/mg of phenol for the traditional TiO_2/UV systems. [188]

7.2 Outlook

This research shows both similarities and differences between solar water splitting and solar water treatment. The results obtained suggest that the limiting factors in solar water splitting devices are the charge carrier generation, separation, collection and injection into the electrolyte. In the case of solar water treatment, catalytic effects at the semiconductor/electrolyte interface seem to be more important, resulting in a more complex relation between power applied to the (photo)electrochemcial device and the reaction rates of organic pollutant oxidation and mineralization. This might be due to the different complex reactions involved, and the competition established between them (pollutant degradation, complete mineralization, reaction selectivity). Further research could clarify the mechanisms involved in these reactions and how they are affected by the power provided by a PV cell. Nevertheless, some common design rules can be established. For both of the two PEC reactions studied, the maximum efficiencies were obtained when the photoactive and the electrocatalytic elements were decoupled. Regarding the device design, several possible architectures have been briefly discussed for water splitting, from a purely PEC device to a PV + DC/DC+ EC devices. Based on the research presented, it becomes clear that some type of PV+EC configuration is needed to achieve good stand-alone conversion efficiencies. If a monolithic approach is taken, then multijunctions are needed. However, other researchers have shown that higher efficiencies may be achieved by using electrically connected single junction solar cells [48] or a PV+DC/DC+EC configuration. [49] A systematic study to compare these different approaches might clarify the most adequate approach for solar water splitting and solar water treatment.

Finally, if both solar water splitting and solar water treatment devices are to be used in a practical setting, upscaling is necessary. [102] Several technical challenges appear when upscaling these devices, including the electrode distance, the electrolyte conductivity, the flow rate of the solution, and the ratios between PV area and electrode area. Additional challenges

7 Conclusions and Outlook

may appear specifically for a certain reaction, such as gas separation and collection for the water splitting case, or the removal of other contaminants such as bacteria or solid particles in the water treatment case. However, technical issues are not the only ones that need to be addressed for practical application of water splitting and water treatment devices. Another element to consider when upscaling is the price of the devices. To be feasible, these devices must consist of earth-abundant materials that can be easily processed. Although this work aimed at using only earth-abundant materials, Pt and IrO_x were still applied as catalysts for the water splitting reaction due to their maturity and stability. Further research must address the challenges posed by these devices aiming at only using earth-abundant materials. Moreover, the fabrication techniques must also be considered. For example, although SHJ solar cells can achieve high conversion efficiencies for some of these applications and are based on the abundant silicon, processing them can be challenging and expensive. Therefore, other less complex fabrication methods that require less pure materials must be applied.

Bibliography

- [1] International Energy Agency. "World Energy Outlook 2017". In: (Nov. 14, 2017).
- [2] International Energy Agency. "CO₂ emissions from fuel combustion". In: (2017).
- [3] M. Perez and R. Perez. "Update 2015 A fundamental look at supply side energy reserves for the planet". In: *IEA-SHCP-Newsletter* 62 (2015).
- [4] C.A. Gueymard, D. Myers, and K. Emery. "Proposed reference irradiance spectra for solar energy systems testing". In: *Solar Energy* 73.6 (2002), pp. 443 –467. ISSN: 0038-092X. DOI: 10.1016/S0038-092X(03)00005-7.
- [5] O. Isabella et al. Solar Energy: The Physics and Engineering of Photovoltaic Conversion, Technologies and Systems. UIT Cambridge Ltd., 2016. ISBN: 1906860327.
- [6] M. Green. Solar Cells: Operating Principles, Technology and System Applications. Prentice-Hall Inc., 1982.
- [7] J. Huang, Y. Shao, and Q. Dong. "Organometal Trihalide Perovskite Single Crystals: A Next Wave of Materials for 25% Efficiency Photovoltaics and Applications Beyond?" In: *The Journal of Physical Chemistry Letters* 6.16 (2015), pp. 3218–3227. DOI: 10.1021/acs.jpclett.5b01419.
- [8] V.V. Tyagi et al. "Progress in solar PV technology: Research and achievement". In: Renewable and Sustainable Energy Reviews 20 (2013), pp. 443 –461. ISSN: 1364-0321.
- [9] K. Yoshikawa et al. "Silicon heterojunction solar cell with interdigitated back contacts for a photoconversion efficiency over 26%". In: *Nature Energy* 2.5 (2017), p. 17032. DOI: 10.1038/nenergy.2017.32.
- [10] A. Blakers et al. "High Efficiency Silicon Solar Cells". In: *Energy Procedia* 33 (2013), pp. 1–10. ISSN: 1876-6102. DOI: 10.1016/j.egypro.2013.05.033.
- [11] A. Descoeudres et al. ">21% Efficient silicon heterojunction solar cells on n- and p-type wafers compared". In: *IEE Journal of Photovoltaics* 3.1 (2013), pp. 83–90.

BIBLIOGRAPHY

- [12] A.H.M. Smets et al. "The Relation Between the Bandgap and the Anisotropic Nature of Hydrogenated Amorphous Silicon". In: *IEEE Journal of Photovoltaics* 2.2 (2012), 94–98. DOI: 10.1109/jphotov.2011.2180701.
- [13] T. Matsui et al. "Development of Highly Stable and Efficient Amorphous Silicon Based Solar Cells". In: 28th European Photovoltaic Solar Energy Conference and Exhibition (2013), pp. 2213–2217. DOI: 10.4229/28theupvsec2013-3do.7.2.
- [14] D.L. Staebler and C.R. Wronski. "Reversible conductivity changes in discharge-produced amorphous Si". In: *Applied Physics Letters* 31.4 (1977), 292–294. DOI: 10.1063/1.89674.
- [15] J. Melskens et al. "The Nature and the Kinetics of Light-Induced Defect Creation in Hydrogenated Amorphous Silicon Films and Solar Cells". In: *IEEE Journal of Photovoltaics* 4.6 (2014), pp. 1331–1336. ISSN: 2156-3381. DOI: 10.1109/JPHOTOV. 2014.2349655.
- [16] H. Sai et al. "High-efficiency microcrystalline silicon solar cells on honeycomb textured substrates grown with high-rate VHF plasma-enhanced chemical vapor deposition". In: Japanese Journal of Applied Physics 54.8S1 (2015).
- [17] A.V. Shah et al. "Thin-film silicon solar cell technology". In: *Progress in Photovoltaics:* Research and Applications 12.2-3 (2004), pp. 113–142. DOI: 10.1002/pip.533.
- [18] Y. Ichikawa et al. "A stable 10% solar cell with aSi/aSi double junction structure". In: Conference Record of the IEEE Photovoltaic Specialists Conference 2 (1990).
- [19] F.T. Si, O. Isabella, and M. Zeman. "Too Many Junctions? A Case Study of Multijunction Thin-Film Silicon Solar Cells". In: Advanced Sustainable Systems 1.10 (2017), p. 1700077. DOI: 10.1002/adsu.201700077.
- [20] B. Yan et al. "Innovative dual function nc-SiO_x:H layer leading to a >16% efficient multi-junction thin-film silicon solar cell". In: Applied Physics Letters 99.11 (2011), p. 113512.
- [21] H. Sai, T. Matsui, and K. Matsubara. "Stabilized 14.0%-efficient triple-junction thinfilm silicon solar cell". In: Applied Physics Letters 109.18 (2016), p. 183506. DOI: 10.1063/1.4966996.
- [22] J. Fang et al. "High-efficiency micromorph solar cell with light management in tunnel recombination junction". In: Solar Energy Materials and Solar Cells 155. Supplement C (2016), pp. 469 –473.
- [23] F.-J. Haug and C. Ballif. "Light management in thin film silicon solar cells". In: *Energy and Environmental Science* 8 (3 2015), pp. 824–837. DOI: 10.1039/C4EE03346A.

- [24] H. Ibrahim, A. Ilinca, and J. Perron. "Energy storage systems—Characteristics and comparisons". In: *Renewable and Sustainable Energy Reviews* 12.5 (2008), pp. 1221 –1250. ISSN: 1364-0321. DOI: 10.1016/j.rser.2007.01.023.
- [25] A.J. Bard and M.A. Fox. "Artificial Photosynthesis: Solar Splitting of Water to Hydrogen and Oxygen". In: *Accounts of Chemical Research* 28.3 (1995), pp. 141–145.
- [26] J.M. Ogden. "Hydrogen: The Fuel of the Future?" In: *Physics Today* 55.4 (2002), 69–75. DOI: 10.1063/1.1480785.
- [27] G. Nicoletti et al. "A technical and environmental comparison between hydrogen and some fossil fuels". In: *Energy Conversion and Management* 89 (2015), 205–213.
- [28] A. Fujishima, K. Honda, and S. Kikuchi. "Photosensitized electrolytic oxidation on semiconduction n-type TiO₂ electrode". In: *Journal of the Society of Chemical Industry Japan* 72 (1969), pp. 108–113.
- [29] A. Fujishima and K. Honda. "Electrochemical Photolysis of Water at a Semiconductor Electrode". In: *Nature* 238 (1972), pp. 37–8.
- [30] G. Wang et al. "Chemically modified nanostructures for photoelectrochemical water splitting". In: Journal of Photochemistry and Photobiology C 19 (2014), pp. 35–51.
- [31] O.K. Varghese and C.A. Grimes. "Appropriate atrategies for determining the photoconversion efficiency of water photoelectrolysis cells: A review with examples using titania nanotube array photoanodes". In: Solar Energy Materials and Solar Cells 92 (2008), pp. 374–384.
- [32] M.G. Walter et al. "Correction to Solar Water Splitting Cells". In: *Chemical Reviews* 111.9 (2011), pp. 5815–5815.
- [33] A.J. Bard et al. "The concept of Fermi level pinning at semiconductor/liquid junctions. Consequences for energy conversion efficiency and selection of useful solution redox couples in solar devices". In: *Journal of the American Chemical Society* 102.11 (1980), pp. 3671–3677. DOI: 10.1021/ja00531a001.
- [34] G.K. Mor et al. "Enhanced Photocleavage of Water Using Titania Nanotube Arrays". In: *Nano Letters* 5.1 (2005), pp. 191–195. DOI: 10.1021/nl048301k.
- [35] Y.J. Hwang et al. "Photoelectrochemical Properties of TiO₂ Nanowire Arrays: A Study of the Dependence on Length and Atomic Layer Deposition Coating". In: *ACS Nano* 6.6 (2012), pp. 5060–5069. DOI: 10.1021/nn300679d.
- [36] P. Saurabh et al. "Iron based photoanodes for solar fuel production". In: *Physical Chemistry Chemical Physics* 16 (2014).

- [37] H. Dotan et al. "Probing the photoelectrochemical properties of hematite α -Fe₂O₃) electrodes using hydrogen peroxide as a hole scavenger". In: *Energy and Environmental Science* 4 (3 2011), pp. 958–964. DOI: 10.1039/C0EE00570C.
- [38] M. Malizia et al. "Formation of a p-n heterojunction on GaP photocathodes for H₂ production providing an open-circuit voltage of 710 mV". In: Journal of Materials Chemistry A 2 (2014), pp. 6847–6853.
- [39] F.F. Abdi, N. Firet, and R. van de Krol. "Efficient BiVO₄ Thin Film Photoanodes Modified with Cobalt Phosphate Catalyst and W-doping". In: ChemCatChem 5.2 (2013), pp. 490–496. DOI: 10.1002/cctc.201200472.
- [40] D. Jing et al. "Efficient solar hydrogen production by photocatalytic water splitting: From fundamental study to pilot demonstration". In: *International Journal of Hydrogen Energy* 35.13 (2010), pp. 7087 –7097. ISSN: 0360-3199. DOI: 10.1016/j.ijhydene. 2010.01.030.
- [41] L. Han et al. "A 5.2% Efficient Water Splitting Device Based on Bismuth Vanadate Photoanode and THin Film Silicon Solar Cells". In: ChemSusChem 7 (2014), p. 2832.
- [42] B. Seger et al. "Using TiO₂ as a Conductive Protective Layer for Photocathodic H₂ Evolution". In: *Journal of the American Chemical Society* 135 (2013), pp. 1057–1064.
- [43] C.R. Cox et al. "Interfaces between water splitting catalysts and buried silicon junctions". In: *Energy and Environmental Science* 6.2 (2013), pp. 532–538. ISSN: 1754-5692. DOI: 10.1039/c2ee23932a.
- [44] R. van de Krol and M. Greatzel. *Photoelectrochemical hydrogen production*. Springer, 2012.
- [45] S. Hu et al. "An analysis of the optimal band gaps of light absorbers in integrated tandem photoelectrochemical water-splitting systems". In: *Energy and Environmental Science* 6 (10 2013), pp. 2984–2993. DOI: 10.1039/C3EE40453F.
- [46] W.-H. Cheng et al. "Monolithic Photoelectrochemical Device for 19% Direct Water Splitting". In: *Condensed Matter* (2017).
- [47] J.W. Ager et al. "Experimental demonstrations of spontaneous solar-driven photoelectrochemical water splitting". In: Energy and Environmental Science 8 (10 2015), pp. 2811–2824. DOI: 10.1039/C5EE00457H.
- [48] J.W. Schuttauf, M.A. Molestino, and E. Chinello. "Solar-to-hydrogen production at 14.2% efficiency with silicon photovoltaics and earth-abundant electrocatalysts". In: *Journal of Electrochemical Society* 163 (10 2016), F1177–F1181.

- [49] W.J. Chang et al. "Design Principle and Loss Engineering for Photovoltaic/Electrolysis Cell System". In: ACS Omega 2.3 (2017), 1009–1018. DOI: 10.1021/acsomega. 7b00012.
- [50] I. Sires et al. "Electrochemical advanced oxidation processes: today and tomorrow. A review". In: *Environmental Science and Pollution Research* 21.14 (2014), 8336–8367. DOI: 10.1007/s11356-014-2783-1.
- [51] S. Pasternak and Y. Paz. "On the similarity and dissimilarity between photocatalytic water splitting and photocatalytic degradation of pollutants". In: *ChemPhysChem* 14.10 (2013), pp. 2059–2070.
- [52] J.M. Kesselman et al. "Electrochemical Production of Hydroxyl Radical at Polycrystalline Nb-Doped TiO₂ Electrodes and Estimation of the Partitioning between Hydroxyl Radical and Direct Hole Oxidation Pathways". In: *The Journal of Physical Chemistry B* 101.14 (1997), pp. 2637–2643. DOI: 10.1021/jp962669r.
- [53] E. Grabowska, J. Reszczyńska, and A. Zaleska. "Mechanism of phenol photodegradation in the presence of pure and modified-TiO₂: A review". In: *Water Research* 46.17 (2012), pp. 5453 –5471. ISSN: 0043-1354.
- [54] Y. Bennani, A. El-Kalliny, and P. Appel. "Enhanced Solar Light Photoelectrocatalytic Activity in Water by Anatase-to-rutile TiO₂ Transformation". In: *Journal of Advanced Oxidation Technologies* 17.2 (2016), pp. 285–296. DOI: 10.1515/jaots-2014-0214.
- [55] L. Liu and X. Chen. "Titanium Dioxide Nanomaterials: Self-Structural Modifications". In: Chemical Reviews 114.19 (2014), pp. 9890–9918. DOI: 10.1021/cr400624r.
- [56] J.H.I. Carey, J. Lawrence, and H.M. Tosine. "Photodechlorination of PCBs in the presence of titanium dioxide in aqueous suspensions". In: *Bulletin of Environmental Contamination and Toxicology* 16.6 (1976), pp. 697–701.
- [57] J. Wen et al. "Photocatalysis fundamentals and surface modification of TiO₂ nanomaterials". In: *Chinese Journal of Catalysis* 36.12 (2015), pp. 2049 –2070. ISSN: 1872-2067.
- [58] W. Smith, W. Ingram, and Y. Zhao. "The scaling of the photocatalytic decay rate with the length of aligned TiO₂ nanorod arrays". In: *Chemical Physics Letters* 479.4–6 (2009), pp. 270 –273. ISSN: 0009-2614.
- [59] M.Y. Ghaly et al. "Treatment of highly polluted paper mill wastewater by solar photocatalytic oxidation with synthesized nano TiO₂". In: *Chemical Engineering Journal* 168.1 (2011), pp. 446 –454. ISSN: 1385-8947.
- [60] A.N. Rao and V.T. Venkatarangaiah. "Metal oxide-coated anodes in wastewater treatment". In: *Environmental Science and Pollution Research* 21.5 (2014), pp. 3197–3217.

- [61] A.M. Al-Hamdi et al. "Efficient photocatalytic degradation of phenol in aqueous solution by SnO₂:Sb nanoparticles". In: *Applied Surface Science* 370 (2016), pp. 229 –236. ISSN: 0169-4332.
- [62] W. Smith and Y. Zhao. "Enhanced Photocatalytic Activity by Aligned WO₃/TiO₂ Two-Layer Nanorod Arrays". In: The Journal of Physical Chemistry C 112.49 (2008), pp. 19635–19641. DOI: 10.1021/jp807703d.
- [63] W. Smith and Y.-P. Zhao. "Superior photocatalytic performance by vertically aligned core–shell TiO₂/WO₃ nanorod arrays". In: *Catalysis Communications* 10.7 (2009), pp. 1117 –1121. ISSN: 1566-7367.
- [64] S. Sun and W. Wang. "Advanced chemical compositions and nanoarchitectures of bismuth based complex oxides for solar photocatalytic application". In: RSC Advances 4 (88 2014), pp. 47136–47152. DOI: 10.1039/C4RA06419D.
- [65] L.-W. Zhang et al. "Synthesis of Porous Bi₂WO₆ Thin Films as Efficient Visible-Light-Active Photocatalysts". In: Advanced Materials 21.12 (2009), pp. 1286–1290. ISSN: 1521-4095. DOI: 10.1002/adma.200801354.
- [66] M.N. Chong et al. "Recent developments in photocatalytic water treatment technology: A review". In: Water Research 44.10 (2010), pp. 2997 –3027. ISSN: 0043-1354.
- [67] T. Egerton et al. "Photoelectrocatalysis by titanium dioxide for water treatment". In: International Journal of Environment and Pollution 27 (2006), pp. 2–19.
- [68] C. Dette et al. "TiO₂ Anatase with a Bandgap in the Visible Region". In: *Nano Letters* 14.11 (2014), pp. 6533–6538. DOI: 10.1021/nl503131s.
- [69] F. Zhu et al. "Amorphous silicon carbide photoelectrode for hydrogen production directly from water using sunlight". In: *Philosophical Magazine* 89.28-30 (2009), pp. 1– 21.
- [70] F.F. Abdi et al. "Efficient solar water splitting by enhanced charge separation in a bismuth vanadate-silicon tandem photoelectrode". In: *Nature Communications* 4.2195 (2013).
- [71] Z. Li et al. "Photoelectrochemical cells for solar hydrogen production: current state of promising photoelectrodes, methods to improve their properties, and outlook". In: *Energy and Environmental Science* 6 (2 2013), pp. 347–370. DOI: 10.1039/C2EE22618A.
- [72] B.A. Pinaud et al. "Technical and economic feasibility of centralized facilities for solar hydrogen production via photocatalysis and photoelectrochemistry". In: *Energy and Environmental Science* 6.7 (2013), p. 1983. DOI: 10.1039/c3ee40831k.

- [73] F. Urbain et al. "Light-induced degradation of adapted quadruple junction thin film silicon solar cells for photoelectrochemical water splitting". In: Solar Energy Materials and Solar Cells 145.Part 2 (2016), pp. 142 –147. ISSN: 0927-0248. DOI: 10.1016/j.solmat.2015.07.033.
- [74] M.G. Walter et al. "Solar Water Splitting Cells". In: *Chemical Reviews* 110.11 (2010), pp. 6446–6473.
- [75] P.S. Bassi et al. "Iron based photoanodes for solar fuel production". In: *Physical Chemistry Chemical Physics* 16 (24 2014), pp. 11834–11842. DOI: 10.1039/C3CP55174A.
- [76] J. Oh et al. "Nanoporous black silicon photocathode for H₂ production by photoelectrochemical water splitting". In: Energy and Environmental Scence. 4 (5 2011), pp. 1690–1694. DOI: 10.1039/C1EE01124C.
- [77] L. Shen et al. "Nanostructured Silicon Photocathodes for Solar Water Splitting Patterned by the Self-Assembly of Lamellar Block Copolymers". In: ACS Applied Materials & Interfaces 7.47 (2015), pp. 26043–26049. DOI: 10.1021/acsami.5b08661.
- [78] J.-W. Jang et al. "Enabling unassisted solar water splitting by iron oxide and silicon". In: *Nature Communications* 6 (2015), p. 7447. DOI: 10.1038/ncomms8447.
- [79] L. Han et al. "Gradient dopant profiling and spectral utilization of monolithic thinfilm silicon photoelectrochemical tandem devices for solar water splitting". In: *Journal* of Materials Chemistry A 3 (8 2015), pp. 4155–4162. DOI: 10.1039/C4TA05523C.
- [80] R. Marshall. "Semiconductor Composites: Strategies for Enhancing Charge Carrier Separation to Improve Photocatalytic Activity". In: *Advanced Functional Materials* 24 (2014), pp. 2421–2440.
- [81] I.A. Digdaya et al. "Extracting large photovoltages from a-SiC photocathodes with an amorphous TiO₂ front surface field layer for solar hydrogen evolution". In: *Energy and Environmental Science* 8 (5 2015), pp. 1585–1593. DOI: 10.1039/C5EE00769K.
- [82] I.A. Digdaya et al. "Engineering the kinetics and interfacial energetics of Ni/Ni-Mo catalyzed amorphous silicon carbide photocathodes in alkaline media". In: *J. Mater. Chem. A* 4 (18 2016), pp. 6842–6852. DOI: 10.1039/C5TA09435F.
- [83] I.A. Digdaya. et al. "Interfacial engineering of metal-insulator-semiconductor junctions for efficient and stable photoelectrochemical water oxidation". In: *Nature Communications* 8 (2017), p. 15968. DOI: 10.1038/ncomms15968.
- [84] J. Mandelkorn and J.H. Lamneck. "Simplified fabrication of back surface electric field silicon cells and novel characteristics of such cells". In: *Solar Cells* 29.2 (1990), pp. 121 –130. ISSN: 0379-6787. DOI: 10.1016/0379-6787(90)90021-V.

- [85] Michael Gratzel. "Solar Energy Conversion by Dye-Sensitized Photovoltaic Cells". In: *Inorganic Chemistry* 44.20 (2005), pp. 6841–6851. DOI: 10.1021/ic0508371.
- [86] V. Smirnov et al. "Microcrystalline silicon oxide (μc-SiO_x:H) alloys: A versatile material for application in thin film silicon single and tandem junction solar cells". In: Journal of Non-Crystalline Solids 358.17 (2012), pp. 1954 –1957. ISSN: 0022-3093. DOI: 10.1016/j.jnoncrysol.2011.12.019.
- [87] H.H. Pham and L.-W. Wang. "Oxygen vacancy and hole conduction in amorphous TiO₂". In: *Physical Chemistry Chemical Physics* 17.1 (2015), 541–550. DOI: 10.1039/c4cp04209c.
- [88] A.G. Scheuermann K.W. Kemp et al. "Conductance and capacitance of bilayer protective oxides for silicon water splitting anodes". In: *Energy Environ. Sci.* 9 (2 2016), pp. 504–516.
- [89] E. Slavcheva et al. "Sputtered electrocatalysts for PEM electrochemical energy converters". In: *Electrochimica Acta* 53 (2007), pp. 362–368.
- [90] S.-T. Hwang et al. "Large area Si thin film solar module applying n-μc-SiO_x:H intermediate layer with low refractive index". In: Solar Energy Materials and Solar Cells 113 (2013), 79–84. DOI: 10.1016/j.solmat.2013.01.042.
- [91] K. Gelderman, L. Lee, and S.W. Donne. "Flat-Band Potential of a Semiconductor: Using the Mott-Schottky Equation". In: Journal of Chemical Education 84.4 (2007), p. 685. DOI: 10.1021/ed084p685.
- [92] V. Demontis et al. "The role of oxide interlayers in back reflector configurations for amorphous silicon solar cells". In: *Journal of Applied Physics* 113.6 (2013), p. 64508. DOI: 10.1063/1.4790875.
- [93] W. Calvet et al. "Silicon based tandem cells: novel photocathodes for hydrogen production". In: *Physical Chemistry Chemical Physics* 16 (24 2014), pp. 12043–12050. DOI: 10.1039/C3CP55198A.
- [94] S. Licht et al. "Efficient Solar Water Splitting, Exemplified by RuO₂-Catalyzed Al-GaAs/Si Photoelectrolysis". In: The Journal of Physical Chemistry B 104.38 (2000), pp. 8920–8924. DOI: 10.1021/jp002083b.
- [95] O. Khaselev, A. Bansal, and J.A. Turner. "High-efficiency integrated multijunction photovoltaic/electrolysis systems for hydrogen production". In: *International Journal of Hydrogen Energy* 26 (2001), pp. 127–132.
- [96] A. Terakawa. "Review of thin-film silicon deposition techniques for high-efficiency solar cells developed at Panasonic/Sanyo". In: Solar Energy Materials and Solar Cells 119.Supplement C (2013), pp. 204 –208. ISSN: 0927-0248.

- [97] N.J. Mohr et al. "Environmental life cycle assessment of roof-integrated flexible amorphous silicon/nanocrystalline silicon solar cell laminate". In: *Progress in Photovoltaics:* Research and Applications 21.4 (2013), pp. 802–815. ISSN: 1099-159X. DOI: 10.1002/pip.2157.
- [98] R.E. Rocheleau, E.L. Miller, and A. Misra. "High-Efficiency Photoelectrochemical Hydrogen Production Using Multijunction Amorphous Silicon Photoelectrodes". In: Energy & Fuels 12.1 (1998), pp. 3–10. DOI: 10.1021/ef9701347.
- [99] F. Urbain et al. "Multijunction Si photocathodes with tunable photovoltages from 2.0 V to 2.8 V for light induced water splitting". In: *Energy and Environmental Science* 9 (1 2016), pp. 145–154. DOI: 10.1039/C5EE02393A.
- [100] K.A. Bush et al. "23.6%-efficient monolithic perovskite/silicon tandem solar cells with improved stability". English. In: *Nature Energy* 2.4 (2017).
- [101] S. Essig et al. "Raising the one-sun conversion efficiency of III–V/Si solar cells to 32.8% for two junctions and 35.9% for three junctions". In: *Nature Energy* 2 (2017), p. 17144.
- [102] S. Kirner et al. "Architectures for scalable integrated photo driven catalytic devices A concept study". In: *International Journal of Hydrogen Energy* 41.45 (2016), 20823–20831. DOI: 10.1016/j.ijhydene.2016.05.088.
- [103] T. Roschek et al. "Microcrystalline silicon solar cells prepared by 13.56 MHz PECVD at high growth rates: Solar cell and material properties". In: MRS Proceedings 664 (2001).
- [104] S.N. Agbo. "Growth and Characterization of Thin Film Nanocrystalline Silicon Materials and Solar Cells". PhD thesis. Delft University of Technology, 2012.
- [105] B. Bills et al. "Effect of Tunnel Recombination Junction on Crossover Between the Dark and Illuminated Current-Voltage Curves of Tandem Solar Cells". In: *IEEE Transactions on Electron Devices* 59.9 (2012), pp. 2327–2330. ISSN: 0018-9383.
- [106] P.-K. Chang et al. "High efficiency a-Si:H/a-Si:H solar cell with a tunnel recombination junction and a n-type μ c-Si:H layer". In: *Thin Solid Films* 520.9 (2012), pp. 3684 3687. ISSN: 0040-6090.
- [107] F.T. Si et al. "Quadruple-Junction Thin-Film Silicon Solar Cells Using Four Different Absorber Materials". In: *Solar RRL* 1 (2017), p. 1700036.
- [108] Y. Lee et al. "Current transport studies of amorphous n/p junctions and its application in a-Si:H/HIT-type tandem cells". In: *Progress in Photovoltaics: Research and Applications* 24.1 (2016), pp. 52–58. ISSN: 1099-159X. DOI: 10.1002/pip.2644.

- [109] R. Vasudevan et al. "A thin-film silicon/silicon hetero-junction hybrid solar cell for photoelectrochemical water-reduction applications". In: Solar Energy Materials and Solar Cells 150.Supplement C (2016), pp. 82 –87. ISSN: 0927-0248.
- [110] P. Buehlmann et al. "In situ silicon oxide based intermediate reflector for thin-film silicon micromorph solar cells". In: *Applied Physics Letters* 91.14 (2007), p. 143505.
- [111] T. Soderstroim et al. "Asymmetric intermediate reflector for tandem micromorph thin film silicon solar cells". In: *Applied Physics Letters* 94.6 (2009), p. 063501. DOI: 10.1063/1.3079414.
- [112] A. Bielawny et al. "3D photonic crystal intermediate reflector for micromorph thin-film tandem solar cell". In: *Physica Status Solidi A* 205.12 (2008), pp. 2796–2810. ISSN: 1862-6319. DOI: 10.1002/pssa.200880455.
- [113] I. D. Parker. "Carrier tunneling and device characteristics in polymer light-emitting diodes". In: *Journal of Applied Physics* 75.3 (1994), pp. 1656–1666. DOI: 10.1063/1. 356350.
- [114] P. Mondal and D. Das. "Development of optimum p-nc-Si window layers for nc-Si solar cells". In: *Physical Chemistry Chemical Physics* 19 (32 2017), pp. 21357–21363. DOI: 10.1039/C7CP02788E.
- [115] S. Licht et al. "Over 18% solar energy conversion to generation of hydrogen fuel; theory and experiment for efficient solar water splitting". In: *International Journal of Hydrogen Energy* 26.7 (2001), pp. 653–659. ISSN: 0360-3199. DOI: 10.1016/S0360-3199(00)00133-6.
- [116] C. Smit et al. "Determining the material structure of microcrystalline silicon from Raman spectra". In: *Journal of Applied Physics* 94.5 (2003), 3582–3588. DOI: 10.1063/1.1596364.
- [117] E. Monaghan, G.Y. Yeom, and A.R. Ellingboe. "Measurement of nc-Si:H film uniformity and diagnosis of plasma spatial structure produced by a very high frequency, differentially powered, multi-tile plasma source". In: *Vacuum* 119 (2015), pp. 34–46. ISSN: 0042-207X. DOI: 10.1016/j.vacuum.2015.03.019.
- [118] A. Smets, T. Matsui, and M. Kondo. "High-rate deposition of microcrystalline silicon p-i-n solar cells in the high pressure depletion regime". In: *Journal of Applied Physics* 104.034508 (2008).
- [119] J.Y.W. Seto. "The electrical properties of polycrystalline silicon films". In: *Journal of Applied Physics* 46.12 (1975), 5247–5254. DOI: 10.1063/1.321593.

- [120] R. Raghunathan, E. Johlin, and J.C. Grossman. "Grain Boundary Engineering for Improved Thin Silicon Photovoltaics". In: *Nano Letters* 14.9 (2014), pp. 4943–4950. DOI: 10.1021/nl501020q.
- [121] M. Fischer et al. "High pressure processing of hydrogenated amorphous silicon solar cells: Relation between nanostructure and high open-circuit voltage". In: *Applied Physics Letters* 106.4 (2015), p. 43905. DOI: 10.1063/1.4907316.
- [122] The World Bank. Improved water source (population with access). Tech. rep. The World Bank, 2015.
- [123] The World Bank. Access to electricity (population). Tech. rep. The World Bank, 2015.
- [124] C.A. Martínez-Huitle and E. Brillas. "Decontamination of wastewaters containing synthetic organic dyes by electrochemical methods: A general review". In: *Applied Catalysis B: Environmental* 87.3–4 (2009), pp. 105–145. ISSN: 0926-3373.
- [125] A.R. Ribeiro et al. "An overview on the advanced oxidation processes applied for the treatment of water pollutants defined in the recently launched Directive 2013/39/EU". In: *Environment International* 75 (2015), pp. 33 –51. ISSN: 0160-4120.
- [126] H. Sarkka, A. Bhatnagar, and M. Sillanpaa. "Recent developments of electro-oxidation in water treatment — A review". In: *Journal of Electroanalytical Chemistry* 754 (2015), pp. 46 –56. ISSN: 1572-6657.
- [127] S.J. Tesh and T.B. Scott. "Nano-Composites for Water Remediation: A Review". In: Advanced Materials 26.35 (2014), pp. 6056–6068. ISSN: 1521-4095. DOI: 10.1002/adma.201401376.
- [128] V.V. Ranade and V.M. Bhandari. *Industrial wastewater treatment recycling and reuse*. Oxford: Elsevier, 2014.
- [129] A. Mixa and C. Staudt. "Membrane-based separation of phenol/water mixtures using ionically and covalently cross-linked ethylene—methacrylic acid copolymers". In: *International Journal of Chemical Engineering* 2008 (2008), p. 12.
- [130] B.H. Hameed and A.A. Rahman. "Removal of phenol from aqueous solutions by adsorption onto activated carbon prepared from biomass material". In: *Journal of Hazardous Materials* 160.2–3 (2008), pp. 576 –581. ISSN: 0304-3894.
- [131] R. Daghrir, P. Drogui, and D. Robert. "Photoelectrocatalytic technologies for environmental applications". In: *Journal of Photochemistry and Photobiology A: Chemistry* 238 (2012), pp. 41–52. ISSN: 1010-6030.

- [132] S. Pulkka et al. "Electrochemical methods for the removal of anionic contaminants from water A review". In: Separation and Purification Technology 132 (2014), pp. 252 –271. ISSN: 1383-5866.
- [133] M.A. Lazar, S. Varghese, and S.S. Nair. "Photocatalytic Water Treatment by Titanium Dioxide: Recent Updates". In: *Catalysts* 2.4 (2012), pp. 572–601. ISSN: 2073-4344. DOI: 10.3390/catal2040572.
- [134] X. Yan, H. Shi, and D. Wang. "Photoelectrocatalytic degradation of phenol using a TiO₂/Ni thin-film electrode". In: Korean Journal of Chemical Engineering 20.4 (2003), pp. 679–684. DOI: 10.1007/BF02706907.
- [135] J. Liao et al. "Photocatalytic Degradation of Methyl Orange Using a TiO₂/Ti Mesh Electrode with 3D Nanotube Arrays". In: ACS Applied Materials and Interfaces 4.1 (2012), pp. 171–177. DOI: 10.1021/am201220e.
- [136] F. Liang and Y. Zhu. "Enhancement of mineralization ability for phenol via synergetic effect of photoelectrocatalysis of g-C₃N₄ film". English. In: *Applied Catalysis B: Environmental* 180 (2016), pp. 324–329. DOI: 10.1016/j.apcatb.2015.05.009.
- [137] H. Selcuk, J.J. Sene, and M.A. Anderson. "Photoelectrocatalytic humic acid degradation kinetics and effect of pH, applied potential and inorganic ions". In: *Journal of Chemical Technology and Biotechnology* 78.9 (2003), pp. 979–984. ISSN: 1097-4660. DOI: 10.1002/jctb.895.
- [138] R. Qiao et al. "Facile Formation of Mesoporous BiVO₄/Ag/AgCl Heterostructured Microspheres with Enhanced Visible-Light Photoactivity". In: *Inorganic Chemistry* 54.18 (2015), pp. 9033–9039. DOI: 10.1021/acs.inorgchem.5b01303.
- [139] Z. He et al. "BiOCl/BiVO₄ p-n Heterojunction with Enhanced Photocatalytic Activity under Visible-Light Irradiation". In: The Journal of Physical Chemistry C 118.1 (2014), pp. 389–398.
- [140] Z.-F. Huang et al. "Nanostructured bismuth vanadate-based materials for solar-energy-driven water oxidation: a review on recent progress". In: Nanoscale 6 (23 2014), pp. 14044–14063. DOI: 10.1039/C4NR05245E.
- [141] X. Gao et al. "Formation of Mesoporous Heterostructured BiVO₄/Bi₂S₃ Hollow Discoids with Enhanced Photoactivity". In: Angewandte Chemie International Edition 53.23 (2014), pp. 5917–5921. ISSN: 1521-3773. DOI: 10.1002/anie.201403611.
- [142] M. Shang et al. "Efficient Visible Light-Induced Photocatalytic Degradation of Contaminant by Spindle-like PANI/BiVO₄". In: The Journal of Physical Chemistry C 113.47 (2009), pp. 20228–20233. DOI: 10.1021/jp9067729.

- [143] L. Hou et al. "Efficient Sunlight-Induced Methylene Blue Removal over One-Dimensional Mesoporous Monoclinic BiVO₄ Nanorods". In: *Journal of Analytical Methods in Chemistry* 2012 (2012), p. 345247.
- [144] G. Yang et al. "Modulated surface textured glass as substrate for high efficiency microcrystalline silicon solar cells". In: Solar Energy Materials and Solar Cells 133 (2015), pp. 156 –162. ISSN: 0927-0248.
- [145] X. Wua et al. "Enhanced Photoelectrocatalytic Degradation of Methylene Blue on Smooth TiO₂ Nanotube Array and Its Impedance Analysis". In: *Journal of the Electrochemical Society* 164.11 (2009), K65–K71.
- [146] J. Yang, A. Banerjee, and S. Guha. "Amorphous silicon based photovoltaics—from earth to the "final frontier"". In: Solar Energy Materials and Solar Cells 78.1–4 (2003), pp. 597–612. ISSN: 0927-0248.
- [147] M.K. Siddiki et al. "A review of polymer multijunction solar cells". In: *Energy and Environmental Sciences* 3 (7 2010), pp. 867–883. DOI: 10.1039/B926255P.
- [148] H. Cotal et al. "III-V multijunction solar cells for concentrating photovoltaics". In: Energy and Environmental Science 2 (2 2009), pp. 174–192. DOI: 10.1039/B809257E.
- [149] H. Tan et al. "Highly Efficient Hybrid Polymer and Amorphous Silicon Multijunction Solar Cells with Effective Optical Management". In: *Advanced Materials* 28.11 (2016), pp. 2170–2177. ISSN: 1521-4095. DOI: 10.1002/adma.201504483.
- [150] H. Beer. "Improvements in or relating to electrodes for electrolysis". In: Patent GB1,147,442 (1969).
- [151] G. Yang et al. "A novel way of texturing glass for microcrystalline silicon thin film solar cells application". In: *Progress in Photovoltaics: Research and Applications* 23.10 (2015), pp. 1283–1290. ISSN: 1099-159X. DOI: 10.1002/pip.2550.
- [152] A.K. Datye et al. "Microstructural Characterization of a Fumed Titanium Dioxide Photocatalyst". In: *Journal of Solid State Chemistry* 115.1 (1995), pp. 236–239. ISSN: 0022-4596.
- [153] X.Z. Li et al. "Photoelectrocatalytic degradation of humic acid in aqueous solution using a ${\rm Ti/TiO_2}$ mesh photoelectrode". In: Water Research 36.9 (2002), pp. 2215 2224. ISSN: 0043-1354.
- [154] J. Tauc. Optical Properties and Electronic Structure of Amorphous Semiconductors. Boston, MA: Springer US, 1969, pp. 123–136. ISBN: 978-1-4757-1123-3. DOI: 10.1007/978-1-4757-1123-3_5.

- [155] A. Saranya et al. "Influence of annealing temperature and number of layers on the properties on nanocrystalline TiO₂ thin films: Structural and optical investigation". In: International Journal of ChemTech Research 6 (2014), p. 2237.
- [156] K. Balaji et al. "Voltammetric Reduction Behavior and Electrode Kinetics". en. In: Portugaliae Electrochimica Acta 29 (2011), pp. 177 –185. ISSN: 0872-1904.
- [157] C. Dumas, R. Basseguy, and A. Bergel. "Electrochemical activity of Geobacter sulfurreducens biofilms on stainless steel anodes". In: *Electrochimica Acta* 53.16 (2008), pp. 5235 –5241. ISSN: 0013-4686.
- [158] H.S. Park et al. "A Novel Electrochemically Active and Fe(III)-reducing Bacterium Phylogenetically Related to Clostridium butyricum Isolated from a Microbial Fuel Cell". In: *Anaerobe* 7.6 (2001), pp. 297 –306. ISSN: 1075-9964.
- [159] H. Liu et al. "Photoelectrocatalytic degradation of triclosan on TiO₂ nanotube arrays and toxicity change". In: *Chemosphere* 93.1 (2013), pp. 160 –165. ISSN: 0045-6535.
- [160] Y. Qin et al. "Efficiently Visible-Light Driven Photoelectrocatalytic Oxidation of As(III) at Low Positive Biasing Using Pt/TiO₂ Nanotube Electrode". In: Nanoscale Research Letters 11 (2016), p. 32.
- [161] A.E. Segneanu et al. Waste Water Treatment Methods. INTECH, 2013, pp. 123–136.
- [162] X. Zhu, M.A. Nanny, and E.C. Butler. "Effect of inorganic anions on the titanium dioxide-based photocatalytic oxidation of aqueous ammonia and nitrite". In: Journal of Photochemistry and Photobiology A: Chemistry 185.2–3 (2007), pp. 289 –294. ISSN: 1010-6030.
- [163] X. Zhu. "Effects of pH, inorganic anions, and surfactants on the photocatalytic degradation of aqueous ammonia in graywater". PhD thesis. University of Oklahoma, 2007.
- [164] X. Yan et al. "Surface texturing studies of bilayer transparent conductive oxide (TCO) structures as front electrode for thin-film silicon solar cells". In: *Journal of Materials Science Materials in Electronics* 26.9 (2015), pp. 7049–7058.
- [165] S. Tokunaga, H. Kato, and A. Kudo. "Selective Preparation of Monoclinic and Tetragonal BiVO₄ with Scheelite Structure and Their Photocatalytic Properties". In: *Chemistry of Materials* 13.12 (2001), pp. 4624–4628. DOI: 10.1021/cm0103390.
- [166] F.F. Abdi. "Towards highly efficient bias-free solar water splitting". PhD thesis. Delft University of Tehcnology, 2015.
- [167] M.-K. Son et al. "Analysis on the Light-Scattering Effect in Dye-Sensitized Solar Cell according to the TiO₂ Structural Differences". In: *International Journal of Photoen*ergy 2012 (2012), p. 480929.

- [168] Y. Bennani, P. Appel, and L.C. Rietveld. "Optimisation of parameters in a solar light-induced photoelectrocatalytic process with a TiO₂/Ti composite electrode prepared by paint-thermal decomposition". In: *Journal of Photochemistry and Photobiology A:*Chemistry 305 (2015), pp. 83 –92. ISSN: 1010-6030.
- [169] S. Esplugas et al. "Comparison of different advanced oxidation processes for phenol degradation". In: Water Research 36.4 (2002), pp. 1034 –1042. ISSN: 0043-1354.
- [170] K. Rekab et al. "H₂O₂ and/or photocatalysis under UV-C irradiation for the removal of EDTA, a chelating agent present in nuclear waste waters". In: *Applied Catalysis A:* General 488 (2014), pp. 103 –110. ISSN: 0926-860X.
- [171] E. Yanez et al. "Homogeneous and heterogeneous degradation of caffeic acid using photocatalysis driven by UVA and solar light". In: *Journal of Environmental Science and Health A* 51.1 (2016), pp. 78–85.
- [172] F. Akhalghian and S. Sohrabi. "Fe/TiO₂ Catalyst for Photodegradtion of Phenol in Water". In: *International Journal of Engineering* 28.4 (2015), pp. 499–506.
- [173] S. Haji, B. Benstaali, and N. Al-Bastaki. "Degradation of methyl orange by UV/H₂O₂ advanced oxidation process". In: *Chemical Engineering Journal* 168.1 (2011), pp. 134 –139. ISSN: 1385-8947.
- [174] DR5000 Spectrophotometer Procedures Manual. Hach Company. 2005.
- [175] Anachemia. A. Chemicals. 2015. URL: http://www.anachemiachemicals.com/pdfs/split_34.pdf.
- [176] P. Brescia. *BioTek.* BioTek. 2012. URL: http://www.biotek.com/assets/tech_resources/A260A280_Spectral_Scanning_App_Note.pd.
- [177] R.E. Bird, R.L. Hulstrom, and L.J. Lewis. "Terrestrial solar spectral data sets". In: Solar Energy 30.6 (1983), pp. 563 –573. ISSN: 0038-092X.
- [178] K. Demeestere, J. Dewulf, and H. Van Langenhove. "Heterogeneous Photocatalysis as an Advanced Oxidation Process for the Abatement of Chlorinated, Monocyclic Aromatic and Sulfurous Volatile Organic Compounds in Air: State of the Art". In: Critical Reviews in Environmental Science and Technology 37.6 (2007), pp. 489–538. DOI: 10.1080/10643380600966467.
- [179] A.N.S. Rao and V.T. Venkatarangaiah. "The Effect of Cathode Materials on Indirect Electrochemical Oxidation of Methyl Orange, Malachite Green and Methylene Blue". en. In: Portugaliae Electrochimica Acta 32 (2014), pp. 213 –231. ISSN: 0872-1904.
- [180] Z. Shen et al. "Degradation of dye solution by an activated carbon fiber electrode electrolysis system". In: *Journal of Hazardous Materials* 84.1 (2001), pp. 107–116.

- [181] L. Fan et al. "Electrochemical degradation of Amaranth aqueous solution on ACF". In: Journal of Hazardous Materials 137.2 (2006), pp. 1182 –1188. ISSN: 0304-3894.
- [182] X.L. Zeng et al. "Photoelectrocatalytic Degradation of Benzoquinone Using Different Cathode Materials". In: *Advanced Materials Research* 610-613 (2012), pp. 86–89.
- [183] R.K. Das et al. "Extraordinary Hydrogen Evolution and Oxidation Reaction Activity from Carbon Nanotubes and Graphitic Carbons". In: ACS Nano 8.8 (2014), pp. 8447– 8456. DOI: 10.1021/nn5030225.
- [184] Y.-B. Xie and X.-Z. Li. "Degradation of bisphenol A in aqueous solution by H₂O₂-assisted photoelectrocatalytic oxidation". In: *Journal of Hazardous Materials* 138.3 (2006), pp. 526 –533. ISSN: 0304-3894.
- [185] P. Sarala and T.V. Venkatesha. "Effect of Cathode Materials on Electrochemical Degradation of Luganil Blue N and Acid Red I". en. In: *Portugaliae Electrochimica Acta* 31 (2013), pp. 175 –183. ISSN: 0872-1904.
- [186] D.D. Dionysiou et al. "Effect of Oxygen in a Thin-Film Rotating Disk Photocatalytic Reactor". In: *Environmental Science & Technology* 36.17 (2002), pp. 3834–3843. DOI: 10.1021/es0113605.
- [187] V.M. Daskalaki et al. "Solar light-induced photoelectrocatalytic degradation of bisphenol-A on TiO₂/ITO film anode and BDD cathode". In: *Catalysis Today* 209 (2013), pp. 74 –78. ISSN: 0920-5861.
- [188] A. Dixit, A. K. Mungray, and M. Chakraborty. "Photochemical oxidation of phenol and chlorophenol by UV/H₂O₂/TiO₂ process: A kinetic study". In: 2010 2nd International Conference on Chemical, Biological and Environmental Engineering. 2010, pp. 153–157. DOI: 10.1109/ICBEE.2010.5650921.
- [189] IEA. Clean Energy Progress Report. Tech. rep. IEA, 2011.
- [190] H. Qin et al. "Water Quality Changes during Rapid Urbanization in the Shenzhen River Catchment: An Integrated View of Socio-Economic and Infrastructure Development". In: Sustainability 6 (Oct. 2014), pp. 7433-7451.
- [191] R. Andreozzi et al. "Advanced oxidation processes (AOP) for water purification and recovery". In: *Catalysis Today* 53.1 (1999), pp. 51 –59. ISSN: 0920-5861. DOI: 10.1016/S0920-5861(99)00102-9.
- [192] R. Kötz, S. Stucki, and B. Carcer. "Electrochemical waste water treatment using high overvoltage anodes. Part I: Physical and electrochemical properties of SnO₂ anodes". In: *Journal of Applied Electrochemistry* 21.1 (1991), pp. 14–20.

- [193] P. Perez-Rodriguez et al. "Treatment of Organic Pollutants Using a Solar Energy Driven Photo-Oxidation Device". In: *Advanced Sustainable Systems* 1.6 (2017), 1700010–n/a. DOI: 10.1002/adsu.201700010.
- [194] M. Panizza et al. "Electrochemical degradation of methylene blue". In: Separation and Purification Technology 54.3 (2007), pp. 382 –387. ISSN: 1383-5866. DOI: 10.1016/j.seppur.2006.10.010.
- [195] M.H Zareie, B.K. Korbahti, and A. Tanyolac. "Non-passivating polymeric structures in electrochemical conversion of phenol in the presence of NaCl". In: *Journal of Hazardous Materials* 87.1 (2001), pp. 199 –212. ISSN: 0304-3894. DOI: 10.1016/S0304-3894(01) 00278-3.
- [196] L. Wang et al. "The influence of anode materials on the kinetics toward electrochemical oxidation of phenol". In: *Electrochimica Acta* 206 (2016), pp. 270 –277. ISSN: 0013-4686. DOI: 10.1016/j.electacta.2016.04.168.
- [197] G.S. Singhal and E. Rabinowitch. "Changes in the absorption spectrum of methylene blue with pH". In: *The Journal of Physical Chemistry* 71.10 (1967), pp. 3347–3349. DOI: 10.1021/j100869a039.
- [198] T.-C. An, X.-H. Zhu, and Y. Xiong. "Feasibility study of photoelectrochemical degradation of methylene blue with three-dimensional electrode-photocatalytic reactor".
 In: Chemosphere 46.6 (2002), pp. 897 –903. ISSN: 0045-6535. DOI: 10.1016/S0045-6535(01)00157-6.
- [199] T. Umebayashi et al. "Visible-Light-Induced Degradation of Methylene Blue on S-Doped TiO_2 ". In: Chemistry Letters 32 (Apr. 2003), pp. 330–331.
- [200] X. y. Li et al. "Reaction pathways and mechanisms of the electrochemical degradation of phenol on different electrodes". In: Water Research 39.10 (2005), pp. 1972 –1981. ISSN: 0043-1354. DOI: 10.1016/j.watres.2005.02.021.

Summary

The current energy scenario requires not only the conversion of renewable energy sources into electrical energy, but also a way to store it to match the demand and supply. In particular, solar energy can be used to stabilize energy conversion and energy supply by converting the energy in other diverse ways. And important possibility are photoelectrochemical (PEC) reactions for water splitting and water treatment. To be able to directly drive these kind of reactions using solar energy, the interactions between the different elements must be studied in detail. In particular, the semiconductor/electrolyte interface seems to play a very important role in these kinds of devices. Moreover, each of these reactions needs specific conditions in terms of current and voltage, and thus specific semiconductor device architectures would be needed. In these two cases, both a study of the reaction, focusing on the semiconductor/electrolyte interface, and a device optimization was performed.

Regarding the water splitting reactions, first the phenomena happening at the interface between semiconductor and electrolyte were studied in chapter 2, exemplified in an a-SiC:H photocathode due to its availability and stability. The results obtained show that an effective back surface field, together with a good band alignment, is beneficial for the water splitting reaction. In particular, the inclusion of a double n-layer consisting of (n)nc-SiO_x:H and then TiO₂ was applied to reduce the energy barriers in the device and facilitate charge carrier injection into the electrolyte. Since the final p-i-n structure resembled a standard thin-film silicon photovoltaic (PV) structure, further research was dedicated to the design of an adequate PV cell architecture to integrate in a stand-alone water splitting device. Since a high voltage is needed to drive the water splitting reaction, chapter 3 focuses on the development of a new hybrid concept of solar cell, monolithically combining a micromorph thin film silicon solar cell on top of a silicon heterojunction (SHJ) solar cell. This cell architecture is potentially able to generate a high voltage and achieve a good spectral utilization. This chapter aims at showing the suitability of this concept for water splitting by building a working demonstrator. The tunnel recombination junctions (TRJ) were thus the focus of this investigation, in order to improve the voltage and fill factor of this cell, essential for a functional multijunction solar cell. The results showed that it was important to include an n⁺ layer as TRJ between the nc-Si:H and the c-Si subcells to lower the energy barrier at the interface. In addition, hydrogenated indium oxide (IOH) was determined to be the best TCO for this cell, especially after a (p)nc-Si-H/(p)nc-SiO_x:H front bilayer was introduced. The best cell

within this investigation achieved an open-circuit voltage of 2.03 V and a fill factor of 0.64. Once a successful demonstrator was fabricated, **chapter 4** tackles the possible light management strategies of this hybrid triple junction device to increase the current density. The main options explored are substrate texturing and thin film silicon absorber tuning in terms of bandgap and crystallinity. Although texturing increased the current density, the voltage and fill factor were reduced due to cracks in the nc-Si:H layer, causing shunting. Thus, an alternative approach of modifying the a-Si:H absorber to obtain a slightly higher bandgap material was chosen for better spectral utilization. By integrating all the final improvements, this solar cell can achieve a PV efficiency of 10.57 %. The final multijunciton solar cell was connected to an electrolyzer, achieving a STH efficiency of 8.3 %.

The second part of this thesis focuses on the PEC reaction for water treatment of organic pollutants. In this case, the interaction between the solution and the semiconductor was studied in chapter 5 by using the semiconductor BiVO₄ as photoanode. This material was used due to its availability and stability, as well as the higher absorption of the solar spectrum compared to the commonly used TiO₂. This study revealed that the crystallographic properties of the film can determine the performance, suggesting that the limiting factor is the catalytic activity at the surface rather than the charge carrier separation. In addition, this photoanode was combined with a solar cell to demonstrate a stand-alone device to oxidate organic pollutants using solar energy. The highest degradation was obtained with a micromorph solar cell, achieving lower pollutant concentrations than the BiVO₄ with the optimum applied potential. This suggests that the current density applied also plays a role, differentiating it from a voltage source. However, this connection brings its own hurdles, such as the spectrum matching. Thus, another approach for solar water treatment is presented in **chapter 6**. Here, a solar cell is designed to be combined with a graphite/graphite electrolyzer, which is a readily available and efficient material. In this analysis, an interesting relation between power and degradation was found, showing that higher powers tend to degrade the original pollutant slightly more, but the chemical oxygen demand (COD) degradation is reduced. This highlights that the combination of a PV cell and an electrolyzer is not as straight forward as it might seem. These issues were overcome in this thesis by tunning the device architecture. The optimized device in this case would consist on a graphite/graphite electrolyzer combined with an a-Si:H/a-Si:H solar cell. This configuration achieved a 70 % reduction on the phenol concentration and a 90 % reduction on the methylene blue concentration, confirming the suitability of this method for water treatment of organic pollutants.

Finally, **chapter 7** aims at answering the main research questions and give some direction to further research. In particular, water splitting and water treatment are compared among them to identify common points and singularities for each reaction. Furthermore, some context regarding the role that this technologies might play in the future energy scenario is given, stressing the need for more multidisciplinary collaboration between the PV and PEC fields to achieve the most efficient solutions to the energy problem.

Samenvatting

Revised by Johan Blanker

Het huidige energiescenario vereist niet alleen de omzetting van duurzaame energiebronnen in elektrische energie, maar ook een manier om het op te slaan en vraag en aanbod te balanceren. Door zonne-energie op verschillende manieren om te zetten, kan deze energie worden gebruikt om de energieomzetting en energielevering te stabiliseren. Een belangrijke techniek is het gebruik van foto-elektrochemische (PEC) reacties voor watersplitsing en waterbehandeling. Om zonne-energie direct te gebruiken voor de reacties, moeten de interacties tussen de verschillende elementen in detail worden bestudeerd. Met name, de halfgeleider/elektrolyt interface heeft een zeer belangrijke rol in dit soort systemen. Bovendien vereist elk van deze reacties specifieke omstandigheden in termen van stroom en spanning en dus zijn specifieke zonnecelconfiguraties nodig. In de watersplitsing en waterbehandeling reacties werden halfgeleider/elektrolyt interface de een systeemoptimalisatie onderzocht.

In hoofdstuk 2 is eerst het halfgeleider/elektrolyt interface in de watersplitsingreactie bestudeerd. Ze zijn in een a-SiC:H fotokathode gestudeerd, vanwege zijn beschikbaarheid en stabiliteit. De resultaten tonen dat een effectief achterveld, samen met een goede uitlijning van de banden op de interface, gunstig zijn voor de watersplitsingsreactie. De inclusie van een dubbele n-laag bestaande uit (n)nc-Si O_x :H en Ti O_2 was toegepast. Dit vermindert de energiebarrières in het system en vergemakkelijkt de ladingdrager injectie in het elektrolyt. De uiteindelijke p-i-n structuur leek op een standaard dunne-laag silicium fotovoltaïsche (PV) structuur. Dus werd verder onderzoek gedaan om een adequate PV-cel-architectuur te ontwikkelen en dit te integreren in een stand-alone watersplitsingsysteem. Omdat een hoge spanning nodig is om de watersplitsingsreactie te sturen, lag de focus in hoofdstuk 3 op de ontwikkeling van een nieuw hybride zonnecelconcept. In dit concept wordt een micromorfe dunne-laag siliciumzonnecel monolithisch gecombineerd met een silicium heterojunctie Deze cel-architectuur heeft het potentieel om een hoge spanning te (SHJ) zonnecel. genereren en een goed spectraal gebruik te bereiken. Dit hoofdstuk is gericht op het aantonen van de geschiktheid van dit concept voor watersplitsing door een werkende demonstrator te fabriceren. De tunnel-recombinatie-overgangen (TRJ) waren de focus van dit onderzoek om de spanning en fill factor van deze cel te verbeteren. Dit is essentieel voor

een functionele multijunctie zonnecel. De resultaten toonden dat het belangrijk was om de n^+ laag op te nemen als TRJ tussen de nc-Si:H en de c-Si subcellen om de energiebarrière op de interface te verlagen. Bovendien was gehydrogeneerd indiumoxide (IOH) de beste TCO voor deze cel, vooral als een (p)nc-Si:H/(p)nc-SiO $_x$:H-dubbellaag geïntroduceerd is. De beste cel binnen dit onderzoek heeft een openklemspanning van 2,03 V en een fill factor van 0,64. Nadat een succesvolle demonstrator was gefabriceerd, bestudeert hoofdstuk 4 strategieën voor licht-beheer van deze hybride zonnelcel, om zo de stroomdichtheid te verhogen. De veelbelovendste opties zijn substraat-texturing en het aanpassen van de bandgap en kristalliniteit van de absorber. Hoewel texturing de stroomdichtheid verhoogte, vormden er barsten in de nc-Si:H laag, die, als gevolg van shunts, een lagere spanning en fill factor opleverden. Aldus werd een alternatieve benadering voor het modificeren van het a-Si:H gekozen. Een a-Si:H materiaal met een hogere bandgap werd gebruikt voor een betere spectrale benutting. Met alle uiteindelijke verbeteringen heeft de zonnecel een PV-rendement van 10,57 % bereikt. Dit zonnecel was met een electrolyzer verbonden, met een STH-rendement van 8,3 %.

Het tweede deel van dit proefschrift richt zich op de PEC-reactie voor waterbehandeling van organische vervuilers. De interactie tussen de elektrolyt en de halfgeleider is in hoofdstuk 5 bestudeerd. Als fotoanode is de halfgeleider BiVO₄ gebruikt. Dit materiaal werd gebruikt vanwege zijn beschikbaarheid, stabiliteit en de hogere absorptie van het zonnespectrum in vergelijking met de veelgebruikte TiO_2 . Deze studie onthulde dat de prestaties van de film afhankelijk zijn van zijn kristallografische eigenschappen. Dit suggereert dat de katalytische activiteit aan het oppervlak de beperkende factor is, en niet de ladingdrager-scheiding. Deze fotoanode werd met een zonnecel gecombineerd om een stand-alone zonne-systeem te maken die wordt gebruikt voor het oxideren van organische vervuilers. De hoogste afbraak werd verkregen met een micromorfe zonnecel, waarmee lagere vervuilingsconcentraties werden bereikt dan met de BiVO₄ met het optimale toegepaste potentieel. Dit suggereert dat de toegepaste stroomdichtheid ook een rol speelt. Deze conclusie brengt weer veel nieuwe uitdagingen, zoals de spectrumoptimisatie. In hoofdstuk 6 is een andere benadering voor waterbehandeling voorgesteld. Hier is een zonnecel ontwikkeld om te worden gecombineerd met een grafiet/grafiet-electrolyzer, een verkrijgbaar en goed werkend materiaal. In deze analyse werd een interessante relatie tussen vermogen en afbraak gevonden. Hoger vermogen breekt meer vervuiler af, maar vermirdert het chemisch zuurstofverbruik (CZV). Dit benadrukt dat de combinatie van een zonnecel en een electrolyzer niet zo eenvoudig is als het lijkt. Deze problemen werden in dit proefschrift

opgelost door de cel-architectuur te veranderen. De geoptimaliseerde architectuur bestaat in dit geval uit een grafiet/grafiet-electrolyzer gecombineerd met een a-Si:H/a-Si:H zonnecel. Deze configuratie leverde een reductie van 70 % op van de fenol-concentratie en een 90 % verlaging van de methyleenblauw-concentratie. Dit bevestingt de geschiktheid van deze methode voor waterbehandeling van organische vervuilers.

Ten slotte beoogt **hoofdstuk 7** de belangrijkste onderzoeksvragen te beantwoorden en een richting te geven aan vervolgonderzoek. Watersplitsing en waterbehandeling zijn onderling vergeleken om gemeenschappelijke punten en singulariteiten voor elke reactie te identificeren. Bovendien wordt een bepaalde context gegeven over de rol die deze technologieën kunnen spelen in het toekomstige energiescenario, met de nadruk op de noodzaak van meer multidisciplinaire samenwerking tussen de PV- en PEC-velden, om zo tot de meest efficiënte oplossingen voor het energieprobleem te komen.

List of Publications

Peer-reviewed papers

- P. Perez-Rodriguez, Y. Bennani, M.J. Alani, W. Smith, L. Rietveld, M. Zeman, A. Smets. Treating of organic pollutants using a solar energy driven photo-oxidation device. *Advanced Sustainable Systems*, 1(6):1700010, 2017.
- P. Perez-Rodriguez, D. Cardenas-Morcoso, I.A. Digdaya, A. Mangel Raventos, P. Procel, O. Isabella, S. Gimenez, M. Zeman, W.A. Smith, A.H.M. Smets. Improving the back surface field on an amorphous silicon carbide (a-SiC:H) thin film photocathode for solar water splitting. *ChemSusChem* 11(11): 1797 –1804, 2018.
- P. Perez-Rodriguez, W. Vijselaar, J. Huskens, M. Stam, M. Falkenberg, M. Zeman, W. Smith, A.H.M. Smets. Designing a Hybrid Thin-film/Wafer Silicon Triple Photovoltaic Junction for Solar Water Splitting. *Under review*.
- P. Perez-Rodriguez, C. Maqueira Gonzalez, L.C. Rietveld, M. Zeman, A.H.M. Smets. Photo-oxidation of organic pollutants usng a silicon-based photovoltaic device. *Under review*.
- L. Han, F.F. Abdi, <u>P. Perez-Rodriguez</u>, B. Dam, R. van de Krol, M. Zeman, A.H.M. Smets. Optimization of Amorphous Silicon Double Junction Solar Cells for an Efficient Photoelectrochemical Water Splitting Device Based on Bismuth Vanadate. *Physical Chemistry Chemical Physics*, 16:4220-4229, 2014.
- R. Vasudevan, Z. Thanawala, L. Han, T. Buijs, H. Tan, D. Degliannis, <u>P. Perez-Rodriguez</u>, I.A. Digdaya, W.A. Smith, M. Zeman, A.H.M. Smets. A thin-film silicon/silicon heterojunction hybrid solar cell for photoelectrochemical water-reduction applications. *Solar Energy Materials and Solar Cells*, 150: 82-87, 2016.
- I.A.Digdaya, <u>P. Perez-Rodriguez</u>, M. Ma, G.W.P. Adhyaksa, E.C. Garnett, A.H.M. Smets, W.A. Smith. Engineering the kinetic and interfacial energetics of Ni/Ni-Mo catalyzed amorphous silicon carbide photocathodes in alkaline media. *Journal of Material Chemistry A*,

4:6842-6852, 2016.

Y. Bennani, P. Perez-Rodriguez, M.J. Alani, W. Smith, L.C. Rietveld, M. Zeman, A.H.M. Smets. Photoelectrocatalytic Oxidation of Phenol for Water Treatment Using a BiVO₄ Thin-film Photoanode. *Journal of Material Research*, 31:2627-2639, 2017.

W. Vijselaar, <u>P. Perez-Rodriguez</u>, P. Westerik, R. Tiggelaar, A.H.M. Smets, H. Gardeniers, J. Huskens. A Stand-alone Membrane-embedded microporous photoelectrochemical cell. *Under review*.

Proceedings and Oral Presentations at Conferences

P. Perez-Rodriguez, I.A. Digdaya, H. Tan, R. Vasudevan, W.A. Smith, M. Zeman, A.H.M. Smets. *Thin-film silicon based devices for cost-effective solar water splitting*, Spring e-MRS Meeting, Lille, France, May 2015.

P. Perez-Rodriguez, I.A. Digdaya, L. Han, H. Tan, R. Vasudevan, W.A. Smith, M. Zeman, A.H.M. Smets, *Towards 10% Solar-to-hydrogen Efficiencies Using Earth-abundant Materials*, 31st European Photovoltaic Solar Energy Conference and Exhibition, Hamburg, Germany, September 2015.

P. Perez-Rodriguez, Y. Bennani, M.J. Alani, W.A. Smith, L.C. Rietveld, M. Zeman, A.H.M. Smets, *Solar Stand-alone Device for Photocatalytic Water Treatment*, Spring MRS Meeting, Phoenix, USA, April 2016.

P. Perez-Rodriguez, Y. Bennani, M.J. Alani, W.A. Smith, L.C. Rietveld, M. Zeman, A.H.M. Smets, Advances in Potocatalytic Water Treatment Using a BiVO₄ Photoanode Under Solar Illumination, Spring MRS Meeting, Phoenix, USA, April 2016.

P. Perez-Rodriguez, I.A. Digdaya, A. Mangel Raventos, M. Falkenberg, R. Vasudevan, M. Zeman, W.A. Smith, A.H.M. Smets; Solar Fuel Production by Using PV/PEC Junctions Based on Earth-abundant Materials. 2016 IEEE 43rd Photovoltaic Conference (PVSC), Portland,

USA, June 2016, pp. 3620-3624.

- P. Perez-Rodriguez, I.A. Digdaya, A. Mangel Raventos, R. Vasudevan, M. Zeman, W.A. Smith, A.H.M. Smets, *Using photovoltaic concepts to improve the back surface field of an amorphous silicon carbide (a-SiC:H) photocathode*, 34th European Photovoltaic Solar Energy Conference and Exhibition, Amsterdam, The Netherlands, September 2017.
- P. Perez-Rodriguez, M. Stam, M. Falkenberg, R. Vasudevan, M. Zeman, A.H.M. Smets, Looking at the tunnel recombination junctions of an a-Si:H/nc-Si:H/SHJ solar cell for water splitting applications, 27 International Photovoltaic Science and Engineering Conference, Otsu, Japan, November 2017.
- P. Perez-Rodriguez, I.A. Digdaya, A. Mangel Raventos, M. Zeman, W.A. Smith, A.H.M. Smets, Design rules of an amorphous silicon carbide (a-SiC:H) thin film photocathode for solar water splitting, Fall MRS Meeting, Boston, USA, November 2017.
- P. Perez-Rodriguez, C. Maqueira Gonzalez, L.C. Rietveld, M. Zeman, A.H.M. Smets, *Design rules of a silicon-based photovoltaic device for oxidation of organic pollutants*, Fall MRS Meeting, Boston, USA, November 2017.

Acknowledgements

After these four years as a PhD candidate, there are numerous people to thank for the work you see here. I hope I can name them all, but if you have helped me in this huge task and do not see your name here, I am sorry and thank you!

First, I need to thank my promotors Miro Zeman and Arno Smets, who gave me the opportunity to start this journey in the PVMD group already as a MSc student, and let me continue as a PhD student. Miro is a very inspiring leader that gave me the support I needed throughout the six years I spent here. I also have to thank Arno for his knowledge, imagination, good spirit, advice and lack of hierarchy. You always made me feel welcomed in your office for any doubt or question I may have, and your example always made me push myself further and try to make the best of each situation.

I must also thank the members of my doctoral committee, Prof. dr. ir. L.C. Rietveld, Dr. ir. W.A. Smith, Prof. dr. M.A.M.M. van der Meijden, Dr. A. Bieberle and Prof. dr. Rutger Schlatmann, for taking the time to read my thesis and for making the trip, from close or afar, to be in my doctoral thesis defense.

As part of the PVMD group, I was also lucky enough to receive feedback on my progress and collaborate with Professor Arthur Webber, and Associate Professors Rene van Swaaij and Olindo Isabella. Thank you for your critical comments and for all the knowledge I was able to gain from you. In addition, I have to thank my colleagues for all the jokes, the conversations (despite Game of Thrones), the travels, and the insights that you shared with me both inside and outside science. In particular, thank you to Ravi, Martijn, Nasim, Yuan, Fai Tong, Robin, Gianluca and Johan for all those frisbee and spikeball o'clock hours. I also want to thank Fai Tong's toys and the distraction man to make the distraction office what it is today. Thanks to Engin Özkol, Paul Procel, Andres Calcabrini and Ana Rita Montes for the celebratory spirit. I would also like to mention Dr. Lihao Han and Thierry de Vrijer, for being the past and the future of solar water splitting and solar water treatment. In terms of science, I want to thank Dr. Rudi Santbergen for his insight in light management, Dr. Paul Procel for making me really understand how useful band diagrams are, to Dr.Engin Özkol, Dr. Ravi Vasudevan and Dr. Dimitris Deligiannis for their insights and guidance when processing SHJ solar cells. Finally, I want to thank Dr. Klaus Jager, Dr. Do Yun

Kim, Dr. Dong Zhang, Dr. Guangtao Yang, Dr. Pavel Babal, Dr. Jimmy Melskens, Dr. Hairen Tan, Dr. Mirjam Theelen, Dr. Andrea Ingenito, Dr. Andrea Illiberi, Dr. Hesan Ziar, Dr. Luana Mazzarella, Dr. Carlos Tobon, Marinus Fischer, Yilei Tian, Klaas Bakker and Juan Camilo Ortiz for being part of my experience and everyday life in the PVMD group. Last, but not least, I want to give a huge thanks to our technicians Martijn Tijssen, Stefaan Heirman and Remko Koornneef for making sure that everything worked as it should, even in weekends and off-work hours sometimes. Also, thank you for letting me practice my Dutch with you. Bedankt! But this huge group of people would not be able to work as smoothly as it does without our excellent secretaries, Sharmila, Ellen, Ilona, Claudia and Diane.

Moreover, as any PhD candidate knows, MSc students are instrumental to be able to do all the research presented here, and I was lucky enough to work with some great and talented students. Thanks to Mathew Alani, Michael Falkenberg, Aleksandra Gorbatenko, Victor Hamoen, Andrea Mangel, Carlos Maqueira, Sharat Srekantan and Machiel Stam. This thesis is really a combined effort from all of us.

As part of my research, I also had close collaboration with other groups inside and outside TU Delft that were crucial in finishing this thesis. I first want to acknowledge my other home in TU Delft: the MECS group. Thank you Dr. Wilson Smith, Ibadillah Digdaya, Dr. Bartek Trzesniewski, Nienke Firet, Fahimeh Nafezarefi, Dr. Moreno de Respinis, Dr. Marco Valenti, Ma Ming, Joost Middelkoop and Herman Schreuders for your great help, discussions and 11am coffee breaks when I was working in the Chemical Engineering building. I also want to acknowledge the great collaboration and friendship I had with Dr. Yasmina Bennani during our water treatment times, and I want to thank Professor Luuk Rietveld for making this collaboration possible. I was also lucky to have very successful collaborations outside TU Delft, and I must thank Sixto Gimenez, Dryalis Cardenas (Universitat Jaume I) and Wouter Vijselaar (TU Twente) for that.

When doing a PhD, one also needs some people outside research to give some breath of air when things don't go as expected. For that, I want to thank my Beach House house-mates Nish, Danny, Aksh, Chris, Marija, Jo and Sanaa for creating a safe space where I could escape when I was stressed. Also thanks to Nish and Danny for accepting being my paranimphs, despite the tuxedos. In addition, I want to acknowledge Damla, Lucas, Rasmus and Guido for making FOM Veldhoven more fun every year, and for all the shared PhD stresses. I would also like to thank the rest of the people that has supported me from all over the world, and

whom would be too many to mention.

Finally, I want to thank my family for the support they gave me throughout this process. In particular, I want to thank my mum for teaching me to learn, to respect and to be a good human in general. Gracias ama por todo lo que me has enseñado. Last but definitely not least, I want to thank Michael, Mike, Lefty. Asante sana kwa kila kitu. Siwezi kukuambia ni kiasi gani umenifanyia. Nimuvea. Nakupenda kabisa.

Curriculum Vitae

Paula Perez Rodriguez was born on 22nd September 1988 in Madrid, Spain. In 2011 she graduated from Universidad de Cantabria, Santander, Spain with a Bachelor degree in Chemical Engineering. In 2013 she received a Master of Science in Sustainable Energy Technology from Technische Universiteit Delft (TU Delft) with an Honours Track in 'Integration of solar PV in electricity grids'. Simultaneously, she worked as a Teaching assistant in the Photovoltaic Material and Devices (PVMD) group within TU Delft. After that, she spent a total of 8 months working for Solar for Sub-Saharan Schools and Communities (S3C), based in Nairobi, Kenya, as an energy consultant. Since 2014, she has been a PhD student working in PVMD at TU Delft. During this period, she has been working on development of PV-PEC devices based mainly in silicon to enhance the solar driven water splitting and water treatment.